The Dissertation Committee for Miles Dalbom Gray
certifies that this is the approved version of the following dissertation:

The RailPAc Arc

Committee:

Laxminarayan L. Raja, Supervisor

Jayant Sirohi, Supervisor

David Goldstein

Philip Varghese

Ofodike Ezekoye

The RailPAc Arc

by

Miles Dalbom Gray,

DISSERTATION

Presented to the Faculty of the Graduate School of

The University of Texas at Austin

in Partial Fulfillment

of the Requirements

for the Degree of

DOCTOR OF PHILOSOPHY

THE UNIVERSITY OF TEXAS AT AUSTIN

August 2018

Dedicated to my fiancée who edited everything, my family who supported everything, and my big brown dog who barked at everything.

Acknowledgments

I wish to thank my advisors Dr. Raja and Dr. Sirohi, my laboratory teachers Michael Pachuillo and Frances Stefani, and my experimental wingman Young-Joon Choi without whom I certainly would not have gotten so far ...

The RailPAc Arc

Publication No. _____

Miles Dalbom Gray, Ph.D.
The University of Texas at Austin, 2018

Supervisors: Laxminarayan L. Raja
Jayant Sirohi

This dissertation will detail work examining the plasma arc of the RailPAc magnetohydrodynamic flow actuator. Initial studies of the RailPAc arc have shown that the arc formation and propagation processes are highly stochastic and in many cases unpredictable. This insight motivated most of the work in this dissertation to better understand the nature of arc propagation, towards the design of a predictable and well behaved high intensity gliding arc. The work consists of several experiment based studies examining the RailPAc plasma arc, focusing on electrical characterization, spectroscopic temperature analysis, narrow-band-imaging species evolution within the arc, and the effects of electrode surface oxidation states on the propagation of the arc. Additional experimental studies examined the effects of external magnetic fields and rod configurations, the effect of the wall near the electrodes, as well as long term damage on copper and elkonite electrodes. Computational studies examined phenomena which were difficult or not possible to characterize

experimentally. This includes mechanisms of wall stabilization, root mobility over oxidized surfaces, and simulations of the arc column in two and three dimensions to examine coupling of the arc to surrounding gas.

The key contributions of this work can be split into two parts, both of which have experimental and computational components. The first is the characterization of the RailPAc arc dynamics (electrically, chemically, and physically) and its coupling to the surrounding flow. This is examined experimentally with spectroscopy, high-speed narrow-band imaging, and electrical measurements, as well as computationally with commercial arc modeling software solving fluid flow coupled to Maxwell's equations in potential form. The second is the examination of the RailPAc arc root interaction with the electrode surface, particularly the anode root which has seen very little examination compared to the cathode in previous research efforts directed at high intensity gliding arcs. Both of these are combined in a computational effort to model the RailPAc arc column in two and three dimensions.

Table of Contents

List of Tables

List of Figures

Chapter 1

Introduction

1.1 Plasma Flow Actuation

Flow control is a technique to favorably alter the character of a wall bounded or free shear flow field [1]. It has existed in some form since prehistory, however formalized studies of flow control began with Ludwig Prandtl's experiments identifying and manipulating boundary layers with suction in 1904 [1]. Flow control has advanced considerably since this period and is an active field of study today. Broadly, the field can be separated into active and passive methods. Passive methods involve no addition of energy and usually have no moving parts. Representative examples include vortex generators on wings, or dimples on golf balls. Active methods require some addition of energy into the flow to change the characteristics of the flow field. This can be through brute force where the energy input is comparable to the kinetic energy of the flow, or, more ideally, a method taking advantage of the nonlinearity of fluid mechanics to achieve a large change in flow structure from a relatively small addition of energy [2]. Most conventional active flow control methods require the use of moving parts.

The most important aspects of flow actuators are the degree of effect on

the flow-field, called control authority, and the speed at which they act, called bandwidth. Conventional flow control methods taking advantage of nonlinearities in fluid mechanics are difficult due to the relatively low bandwidth relative to control authority [2]. This has lead to interest in plasma flow actuation techniques which offer a variety of advantages over conventional methods.

Plasma flow actuators typically require no moving parts and possess high bandwidth, while maintaining at least modest levels of control authority. Plasma flow actuation techniques rely on a variety of phenomena to achieve their goals allowing them to be categorized by the means of energy delivery to the flow. Plasma actuators use simple thermal heating, electrohydrodynamic forces, magnetohydrodynamic forces, or some combination of the three to augment flow near the device. These are outlined in Figure 1.1.

Electrohydrodynamic (EHD) actuators rely on electrostatic forces to impart momentum to the flow. The most widely studied are dielectric barrier discharge (DBD) actuators [3]. DBDs and similar devices are arguably the most active area of study within plasma flow actuation. While DBD actuators are simple to implement, their control authority is relatively low, with typical induced velocities in quiescent air $\sim$1 m/s [3]. They have shown the ability to reattach flow over stalled airfoils at low velocities $\sim$20 m/s and Re$\sim 10^5$ [4].

Thermal actuators rely on efficient heating of neutral gas by a plasma to actuate the flow either through gas property changes as in [5] or through induction of shocks in the flow [6–8]. While most plasma actuators are at least partly thermal actuators, pure thermal actuators offer more limited use cases

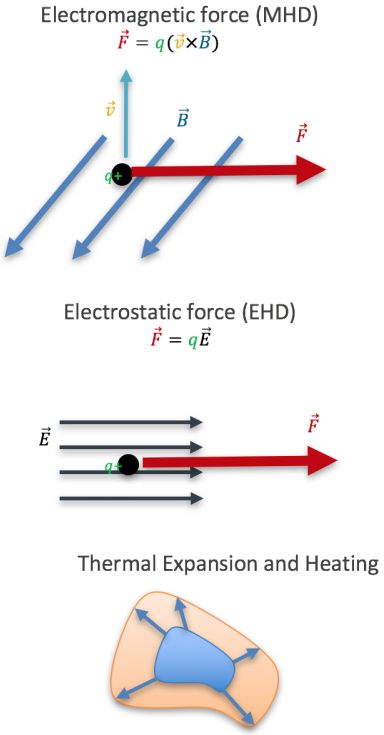

Figure 1.1: Plasma flow actuator varieties.

since they are inherently incapable of adding directed momentum without some kind of nozzle. Still, nanosecond pulsed DBD (NS-DBD) actuators have shown increased flow reattachment at higher Re compared to conventional DBD actuators with Re$\sim 10^5$ and Mach numbers of M~ 0.6 [9, 10].

Magnetohydrodynamic (MHD) actuators rely on $\vec{J}\times\vec{B}$ forces to impart momentum to the flow. They have seen some limited study but are largely a fringe topic in the plasma actuator community likely due to the inherent inefficiency of sustaining long-lived thermal plasmas. However, there are some

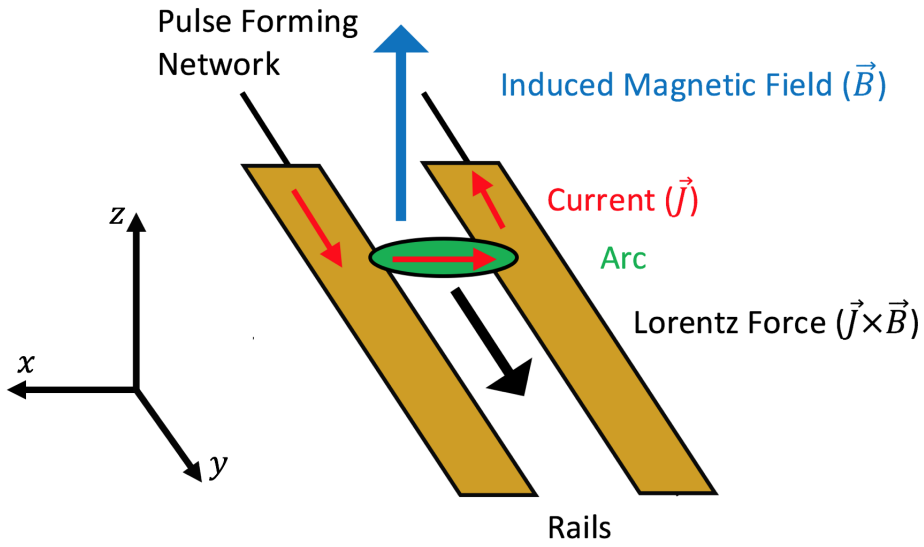

Figure 1.2: Simple RailPAc Schematic.

significant advantages to MHD actuators, namely the lack of inherent phyical limitations on momentum addition as is the case for DBDs [11].

1.2 The RailPAc

The RailPAc (Rail Plasma Actuator) is a magnetohydrodynamic flow actuator [12]. It offers a variety of benefits over both conventional flow actuators and other varieties of plasma flow actuators due to its lack of moving parts, low mass, high control bandwidth, and potential for use in high Reynolds number flows ($Re > 10^6$) [2, 11, 13, 14]. The RailPAc consists of two rectangular rail electrodes, flush mounted parallel to one another on a ceramic surface, and connected to a high current ($\sim$1kA) pulse forming network designed to

operate at ∼100V. An arc is ignited between the electrodes, and the current passing through the arc and the rails induces a magnetic field which interacts with the current in the arc to push the arc along the surface of the electrodes by means of the $\vec{J} \times \vec{B}$ Lorentz force. This is outlined in Figure 1.2.

The motion of the arc has been shown to induce flow in the air above the surface, with measured velocities as high as 16 m/s in a flow with Reynolds number of 4.5×10^5 [12]. Previous studies were largely preliminary in nature, studying a single RailPAc prototype configuration like that shown in Figure 1.3. The arc itself merited only brief examination in the studies, as in [15], with most effort aimed at understanding of the efficacy of the actuator as a whole. However, a deep understanding of the RailPAc plasma arc is integral to optimization of the RailPAc as a flow actuator and provides a unique geometry which helps to elucidate observed phenomena in more conventional arc geometries. A more complete characterization of the RailPAc arc is the primary goal of this dissertation work.

This chapter will provide background information to better understand the dissertation work before moving into more detailed results of experiments and simulations.

1.3 High Intensity Arcs

Broadly speaking, the RailPAc arc falls into the category of high-intensity arcs, or more precisely high intensity gliding arcs. High intensity arcs are quite common. Stadium lighting is perhaps the most familiar exam-

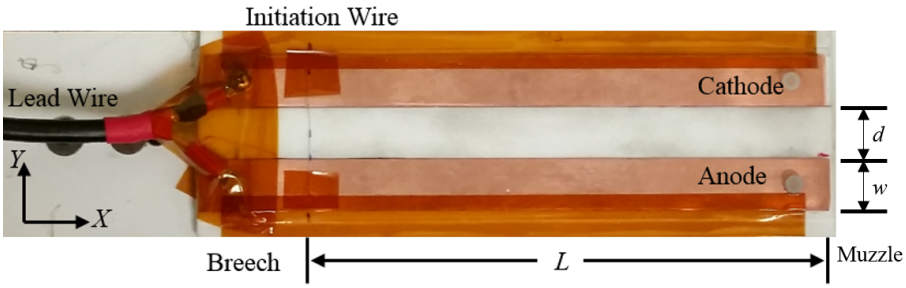

Figure 1.3: A top view of the experimental RailPAc prototype. The arc propagates along the y-direction. The z-axis is oriented out of the page. The rails here are separated by a distance (d) of 13 mm, and are each 13 mm wide (w), and 152 mm long. The distance from initiation point (breech) to muzzle (L) is 127 mm.

ple, however, the arcs found in welding torches, atmospheric lightning, and arc furnaces also qualify. High intensity gliding arcs are less common, with the only real examples in industry being found in high voltage circuit breakers. High intensity arcs may be defined in several ways depending on the author, but most commonly they are required to primarily act under forces which they induce themselves [16]. This means that the dominant flows affecting the arc are also created by the arc.

High intensity arcs typically have currents of several hundred amperes or more and are fully thermalized with temperatures of ∼10,000-30,000K [17–20]. High intensity arcs may be divided into three distinct macroscopic regions: the anode root, the cathode root, and the arc column [21]. Figure 3 outlines these components, and sub-components, for several arc geometries. The arc column usually accounts for the majority of the volume in the arc. It is the

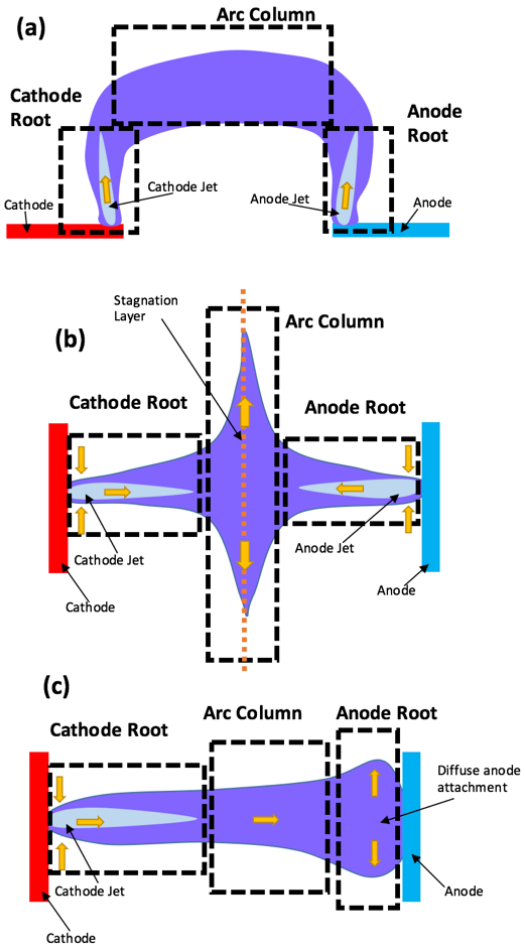

Figure 1.4: Structure of high intensity arcs. The RailPAc arc is shown in (a), while (b) shows an anode dominated arc, and (c) shows a cathode dominated arc.

diffuse plasma which connects the two roots and is located directly between the electrodes, or blown outwards to form an arch shape. The extent of the column is often defined by the location within the arc where axial changes in fluid and electrical properties are negligible [21].

At high currents ($\sim$1000A), the cathode root of the RailPAc arc is usually constricted near the interface of the plasma and electrode surface, a consequence of heat loss to the electrode coupled with the inherent difficulty of generating conditions conducive to eject sufficient electrons from the surface to maintain charge continuity [16]. This constricted area increases the local magnetic field, inducing magnetic pumping, which in turn forms a jet of hot, low-density plasma directed normal to the surface of the electrode as described by Chen [16] and Sanders [22]. An anode jet may also form by a similar process, provided the cathode jet is not able to convect hot plasma to the surface of the anode, negating the constricting effect of heat loss to the electrode surface [22]. If the anode jet is able to form and is directed in opposition to the cathode jet, it pushes on the cathode jet, forming a stagnation layer between the anode and cathode. This is illustrated in Figure 3b.

If only a cathode jet is present, the arc is considered to be a cathode dominated arc, while if the anode jet is able to form and compete with the cathode jet it is considered an anode dominated arc. When the anode jet is not able to form, usually due to high velocity flow coming from the cathode jet, the anode root will be diffusely attached with hot plasma covering a large area of the root. Previous studies have found root jet velocities on the order of

$\sim$10-100 m/s [21], with powerful cathode jets achieving velocities of 600 m/s [23]. Mass continuity requires that fluid be entrained into the jet from around the root, unless enough material can be evaporated into the root to fully supply the jet. Simulations have shown this effect, and predict entrainment velocities of $\sim$1-2 m/s [16]. The directions of these flows are indicated in Figure 3.

The RailPAc arc displays many of the same structures found in other high intensity arcs, however, the unique flush mounted geometry of the electrodes shown in Figure 3a introduces additional effects which change the overall effect of the simple high intensity arc structures. The jets formed may be due to traditional magnetic pumping but can also occur due to direct magnetic pressure caused by the sharp turn the current must make as it exits the electrode. Jets may also point in the same direction in this conformation in contrast to the way they form in traditional electrode geometries where they always point against each other. These factors make the RailPAc a rich test bed for examination of phenomena which would not be visible in traditional arcs.

1.4 Plasma Surface Interactions and Electrode Oxidation States

The deleterious effects on nearby surfaces due to the extreme environment created by thermal plasmas makes electrode erosion a major concern in any case where direct contact between thermal plasmas and electrodes is required. Melting of electrode surfaces is an ubiquitous problem in arc en-

gineering since even highly refractive materials like tungsten melt at $\sim$ 3000 K whereas the coldest thermal plasmas maintain temperatures on the order of $\sim$5000 K and higher [24, 25]. Vaporization of electrode material and re-deposition on the electrode surface is also commonly encountered [26, 27].

Plasma arc surface modifications are almost exclusively dependent on the behavior and characteristics of the arc roots (where the plasma attaches to the electrodes). Arcs may attach either diffusely or at constricted spots on either the cathode or anode [24, 28]. The mode of attachment has been found to be largely a consequence of heat loss to the electrode leading to variable constriction of the current path [16]. Diffusely attached roots cause minimal electrode erosion compared to constricted roots as a consequence of the greater temperatures found at arc spots [21]. Arc root attachment sites are marked by erosion craters and melting sites, the severity of which depends on the mode of attachment and the time of residence. Heating of the electrodes by the presence of the arc and the subsequent cooling may also generate thin metal-oxide layers on the surface of the electrodes [24].

The effect of variation in the electrode oxidation states have been explored by several previous studies. Most have focused on oxidation of the cathode. Cathodic oxide layers can be important in sustaining the arc discharge when thermionic cathode emission is not possible on so called cold cathodes where the thermionic temperature of the electrode material is higher than the melting point [24]. Cold cathode arcs may be sustained by one of two emission processes. The first requires the continuous evaporation of elec-

trode material to work as charge carriers in the arc. These are called metal arcs. The second relies on the presence of an oxide layer which is believed to enhance the local electric field by trapping ions to form temporary electrets [29]. These are called oxide arcs [30].

Considerable work has been done on the effects of oxidized electrode surfaces on gliding arcs similar to the one found in the RailPAc. Several studies corroborate that presence and subsequent erosion of a thin oxide layer on the cathode is necessary in gliding arcs to maintain fast propagation of the cathode root [30–32]. This erosion was found to occur primarily due to vaporization of electroformed channels in the oxide layer [27]. Thin oxide layers were found to promote fast movement of the cathode root, while thick oxide layers inhibited fast movement [33]. The same study found that it was important that the cathode be large enough that multiple possible paths might be traversed by the cathode root. It has been speculated that this movement promotion may be due to the production of electrets in the thin oxide layer created by the arc [34, 35]. Poeffel found that if thick oxide layers were present on both electrodes, higher magnetic fields were required to achieve arc root movement than arc treated surfaces or scraped surfaces but did not distinguish changes if only one of the electrodes was oxidized [36]. Li-Chun found that gliding arc anode roots could easily traverse sections of electrode with a thick oxide layer, however cathode roots could not do the same[33].

With the exception of the work by Poeffel [36] and Li-Chun [33], research into the effect of oxide layers and electrode surface damage has primar-

ily focused on the cathode. For conventional arcs with a direct, linear current path between parallel electrodes this makes sense, because the dynamics of high intensity arcs are primarily driven by the cathode [24]. Even attachment modes at the anode are primarily a function of fluid flow due to magnetically pumped jets formed by the cathode [22, 37]. However, work on the RailPAc, as well as other gliding arcs has found that the anode can play a retarding role on the net motion of the arc due to frequent anchoring [30, 38]. This motivates a desire to better understand the interaction of the anode with the plasma arc.

1.5 Free Burning Arc Aerodynamics

The arc column is the often-diffuse plasma which connects the two roots and is located directly between the electrodes, or blown outwards to form an arch shape. As discussed above, the extent of the column is usually defined by the locations within the arc where axial changes in fluid and electrical properties are negligible[21]. Alternatively it can be viewed as the point where instabilities in the plasma introduced by the electrodes are no longer present [37]. Hence the column may be approximated as only having significant changes in two dimensions while the arc roots have more significant three dimensional structure. For stationary arcs the simplifications of column modeling can be extended to a single dimension, where the entirety of column behavior might be described by a radial coordinate as in [39]. Models for very high current arcs may even go so far as to assume an isothermal arc with a single temperature independent of radius or axial coordinate within the arc

[40]. The approximation that the arc column is only variable in two dimensions motivates the work presented here where coupling of a magnetically blown arc with the surrounding flow is investigated in two and three dimensions.

A great deal of work was done on free burning and wall stabilized arcs with applied transverse magnetic fields in the 1960s and 1970s. Experimental work found linear relationships between applied field strength and the square of the arc transit velocity in several working gases [41]. Early models assumed the arc is impermeable to the surrounding air making the situation identical to a wall stabilized arc with high temperature boundaries [42]. This approximation allows for analytical models of the arc temperature and velocity fields within the arc. Observed trends in the velocity of the whole arc could only be reproduced by assuming a drag coefficient similar to a solid cylinder. Drag coefficient assumptions were born out of experimental work suggesting arc aerodynamic drag coefficients matched well with unheated cylinders [43, 44] though some models suggest arc drag coefficients may be much higher [41]. The same studies found that arc velocity is uncorrelated with arc current and is only dependent on the magnitude of the applied magnetic field. The independence of arc velocity from arc current is not possible to capture using fixed radius arc models. All of these models also rely on steady state assumptions, disallowing analysis of transient phenomena at the start of the arcs movement. A full time dependent solution of the governing equations would allow for natural development of an arc radius and transient development such as interactions of arc forming with the initial shock generated by the genesis of

the arc. This has been done for switchgear applications but the case studied was confined by walls, exacerbating pressure effects, and aerodynamics effects of the moving arc were not discussed in detail [45].

1.6 Dissertation Contributions

Initial studies of the RailPAc found that the arcs formation and propagation are highly stochastic and often unpredictable. This has motivated most of the work in this study to better understand the nature of the arc. This work consists of several major experiment based studies examining the RailPAc plasma arc focusing on electrical characterization, spectroscopic temperature analysis, narrow-band-imaging species evolution within the arc, and the effects of electrode surface oxidation states on the propagation of the arc. Experiments were also performed to examine the effects of external magnetic fields and rod electrode configuration, the effect of the wall near the electrodes, long term damage on copper and Elkonite electrodes, as well as techniques for construction of RailPAc arrays which would be necessary in any large scale implementation of the RailPAc. Additionally, computational studies have been performed to examine phenomena that were difficult or impossible to characterize experimentally. This includes mechanisms of wall stabilization, root mobility over oxidized surfaces, and 3D simulations of the entire RailPAc.

The key contributions of this work can be split into two parts both of which have experimental and computational components. The first is the characterization of the RailPAc arc dynamics (electrically, chemically, and

physically) and its coupling to the surrounding flow. This is examined experimentally with spectroscopy, high-speed narrow-band imaging, and electrical measurements, as well as computationally with the commercial arc modeling software VizSpark. The second is the examination of the interaction of the RailPAc arc roots with the electrode surface, particularly the anode root, which has seen very little examination compared to the cathode in previous research efforts directed at high intensity gliding arcs. Lastly the aerodynamics of the arc column are examined computationally in two and three dimensions.

Chapter 2

Basic Dynamic Characterization

2.1 Introduction

Initial experimental studies of the RailPAc examined global characteristics of the arc, treating the actuator more or less as a black box [12]. Resultant flow modification was analyzed for a given electrical input and electrode configuration with some limited engineering analysis of the arc itself. However, a detailed analysis of the arc of the RailPAc was not made beyond that done by Sitaraman [15]. This chapter will cover the first detailed experimental analysis devoted specifically to the RailPAc arc.

Study of the structure and motion of magnetically driven arcs illustrates a rich variety of features. For example, gliding arcs maintain a single arc mode with a single coherent arc column at low currents, but can transition to a distributed arc mode at high currents, especially if the arc is confined within close gap dielectric walls. In this distributed arc mode, multiple arc columns form simultaneously as a result of restrike phenomena, where hot gas and ablated wall or electrode material in the vicinity of a primary moving arc column alter conditions enough to produce an additional local breakdown [46, 47]. Other arc motion modes may be characterized by whether arc roots

move smoothly over the electrode surface or in distinct jumps with anchored pauses [48].

When driven magnetically, the forward movement of the arc is facilitated by a distortion of the arc column in the direction of the Lorentz forces. As the column is pushed forward by the Lorentz force, the arc roots are either dragged along behind, or the column forms a new root ahead of the old roots [49, 50]. Arc roots tend to propagate by a discontinuous motion on the anode side, switching between moving and anchored modes, but tend to stay in a smooth continuous movement mode on the cathode side [51], [52]. The anchoring of the arc has been shown to be a strong function of electrode material, with more easily vaporized materials producing longer anchoring times [53]. These modes also play a major role in the amount of damage imparted to the electrode surface, with crater/spot damage on the electrode surface at the location where the arc root anchors to the surface [52].

The arc-heating of the gas produces large dilatational (volumetric expansion) effects that can have an impact on the arc structure and its motion [54–56]. For example, natural convection effects can be destabilizing for an arc and cause arc column motion. Hot expanding gases can also push the arc away from the wall surface, distorting the column structure [49].

2.2 Experimental Setup

The experimental setup for the study of driven arc phenomena in an experimental RailPAc device is shown in Figure 1.3. RailPAc operation was

described in detail by Pafford et al. [12]. A summary of the RailPAc operation is presented below.

An arc is initiated at the one end (the breech end shown in Figure 1.3) of a pair of parallel long flat electrodes (rails) that are mounted on a dieletric surface. The arc is powered by a pulse forming network (PFN) connected at the breech end of one of the rails. The other rail is grounded, also at the breech end. A current loop is formed by its path through the lead wire into the powered rail, across the arc to the ground rail, and then out through the other lead wire. This current loop induces a magnetic field in the plane perpendicular to the rail electrodes. The sense of this field is such that the Lorentz (JxB) force acting on the arc column pushes the arc along the length of the rails in the direction opposite to the connection with the PFN. While the principle of Lorentz forcing is common to all magnetically driven arcs, the novelty of the RailPAc device is its use of the arc motion to induce velocity in the surrounding air, resulting in an effective low-speed, high authority, atmospheric pressure aerodynamic flow actuator [12].

In the experiments discussed in this paper, the rails are made of copper and measure 152 mm long, 13 mm wide, and 0.6 mm thick. The thickness of the electrodes has limited effect on the transit of the arc since only the top surface of the electrode is exposed to air. The thickness used here was chosen to minimize the invasion into any structure on which the RailPAc is mounted while also maintaining low electrical resistance and mitigating flexure due to Lorentz forcing. The electrodes are flush mounted on a Macor ceramic plate

and are spaced 13 mm apart. The arc is initiated with an aluminum-copper alloy fuse wire placed 25 mm from the breech end of the rails. The location of the initiation wire and the rail length limits the maximum transit distance (L) to 127 mm. Following railgun convention, this dissertation will refer to the lead wire attachment side of the rails as the breech, and the opposite end of the rails as the muzzle [57]. A fuse wire was used for initiation purposes to maximize reproducibility since high voltage initiation techniques do not always initiate the arc in the same place on the rails.

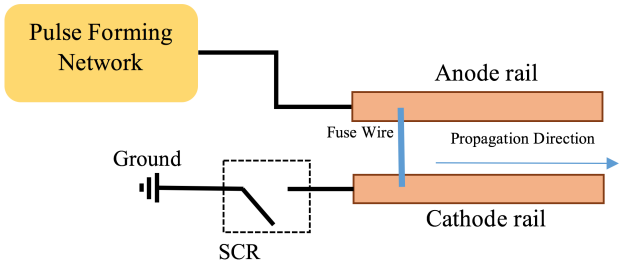

Figure 2.1: A schematic of the RailPAc experimental system. The pulse forming network brings both the anode and cathode rails to positive potential and then the SCR switch drops the cathode rail to ground. This draws current through the fuse wire, which explodes, forming the arc which then propogates down the rails until the pulse forming network ceases current supply.

The RailPAc prototype was powered by the pulse forming network indicated in Figure 2.1. The network consists of a capacitor bank, inductor, and a silicon controlled rectifier (SCR), and provides a ∼5 ms half pulse of current based on the LC time constant of the network. The capacitor bank is comprised of six electrolytic capacitors (Sprague Powerlytic 36DX) set up in parallel with a total capacitance of 21 mF. The bank is charged with a

Xantrex XHR 600 DC power supply and discharged when a trigger voltage is supplied to the SCR. After the trigger voltage is applied, a large current from the capacitor vaporizes the fuse wire and subsequently forms an electrical arc across the rails.

2.2.1 Electrical Measurements

Electrical measurements were conducted to determine the transient arc current I, capacitor bank voltage V_{cap}, and breech voltage V_{breech} during the arc transit. The arc current was measured with a Rogowski coil on the ground side of the SCR by numerically integrating its signal in time. A P5205 differential voltage probe was connected to the lead wire attachment points at the breech end of the rails to measure breech voltage, and another was attached to the capacitor bank terminals to monitor the capacitor bank voltage. The signals from each measurement device were acquired with Tektronix TDS 3014B oscilloscopes at a sampling frequency of 500 kHz.

2.2.2 High-Speed Imaging

Three high-speed cameras were placed along three mutually orthogonal directions to characterize the arc shape in three dimensions. A Phantom V5 camera was mounted above the RailPAc prototype to capture the transit event from above. Two Phantom Miro M-310 cameras were mounted on the anode side and muzzle side to capture the side view and frontal view of the arc, respectively. The Miro M-310 series cameras have higher sensitivity CCD

Table 2.1: High-speed camera specifications and viewing orientations.

Camera	Viewing Direction	Frame Rate (per second)	Resolution (pixels)	Mylar Filter	Exposure Time (s)	Sensitivity (ISO)
Phantom Miro M-310	-x	26000	320x240	Yes	10	3900
Phantom Miro M-310	-y	13000	512x320	Yes	1	3900
Phantom V5	-z	13000	256x256	No	2	600

arrays than the V5, with an ISO of 3900 in the Miro M-310 compared to an ISO of 600 in the V5, so a thin Mylar film (10 mil) was used as a filter for the two Miro cameras. Table 1 lists the frame rates, resolutions, and filters used in the high-speed imaging. All lenses used an F-stop of 22 for all acquisitions. Differences in frame rate between the two M-310 cameras are due to the relative size of each cameras target which called for different resolutions. The phantom V5 has a lower maximum framerate than the M-310.

2.2.3 Spectroscopy

An Ocean Optics HR2000+ spectrometer was used to measure temperature and species composition of the arc. The spectrometer has a resolution of 0.065 nm with responsive range of 200-1100 nm. However, the tungsten calibration source used to calibrate the spectrometer and the fiber optic cable used in the light collection system reduced the reliable spectral response to a range of about 400-900 nm. A collimating tube was used to limit the spectrometer

field of view. This tube has a small viewing port on each end that limits the viewing angle of the spectrometer to 1.1^o. The spectrometer was connected to the collimating tube with a 400 μm fiber-optic cable. Measurements were taken from approximately 15 cm away from the RailPAc surface at a 45^o angle up from the plane of the rails, resulting in an elliptical field of view with a minor axis length $\sim$1.5 mm and a major axis length $\sim$2.0 mm. This is comparable to the diameter fo the arc meaning that the temperature measurements approximate a volume average of the arc temperature. This small field of view provides a simple means of resolving the behavior of the arc in time and space as it transits along the rails. The collimating tube was moved down the rails in increments of 1.3 cm to track changes in the arcs behavior during its transit down the rail. Data was taken at each increment by integrating all incident light on the spectrometer for 10 ms after initiation of the arc. As a result, the absolute intensity of light emitted by the arc cannot be determined.

Several techniques were used to analyze the accumulated spectral data. Analysis of measured data and comparison with values for known strong emission lines from NIST [58] and Camachos analysis of nitrogen plasmas [59] allowed determination of species present in the arc. By integrating the area under emission lines of one species and comparing them with the integrated area under lines of another species, the evolution of species ratios as the arc propagates along the rails can be estimated, provided that temperature does not vary significantly between measurements. Temperature was measured by assuming that the majority of light emitted by the arc comes from the core of

the plasma column, which is assumed to be in local thermodynamic equilibrium (LTE) and that self-absorption by the plasma column is negligible. The condition of LTE implies that

$$n_i = \frac{ng_i}{Z} exp\left(\frac{-E}{k_B T}\right) \tag{2.1}$$

where n_i is the density of a state, n is total density of the species, g_i is the degeneracy of the state, Z is the partition function of the system, T is the temperature, E_i is the energy of the state, and k_B is Boltzmann's constant. The absolute emission intensity per unit solid angle I_{ij} of a spectral line resulting from transition from state i to state j is given by

$$I_{ij} = \frac{V}{4\pi} A_{ij} n_i h\nu_{ij} \tag{2.2}$$

where, V is the volume from which light is emitted, A_{ij} is the Einstein emission coefficient for the spectral line, and h_{ij} is the energy of the photon. Rearranging equations (1) and (2), one can obtain the relation

$$ln\left(\frac{I_{ij}}{g_i A_{ij} h\nu_{ij}}\right) = ln\left(\frac{Vn}{4\pi Z}\right) - \frac{E_i}{k_B T} \tag{2.3}$$

Since all of the quantities in the first term on the right-hand side are constant for a given spectrum, the slope of the line created by the quantity on

the left-hand side plotted versus the energy of the upper state of the emitting species, E_i, gives the temperature. This method is typically referred to as the Boltzmann plot approach to determining temperature [60]. Since Boltzmann plots only allow as many data points for each measurement as there are spectral lines with well-known emission parameters, this technique was further refined by normalizing the left-hand side of equation (3) to zero for one of the spectral lines and only looking at the relative position of the other lines in the Boltzmann plot space to calculate the regression line that yields the temperature. This allowed for the inclusion of data from several runs in the same Boltzmann plot, dramatically increasing the accuracy of the temperature measurements. This method improves on that presented in [61]. The temperature calculated using this technique is a volume average of the arc averaged over several shots at a single location in the arcs transit.

2.3 Results and Discussion

Electrical characteristics of the arc are discussed first. Electrical data was taken for 100 firings and data from each of these was synthesized to find consistent trends in the highly non-repeatable process of the gliding arc. Data from a single representative firing which displays many of the consistently observed characteristics of a RailPAc firing is presented in Figure 2.2. The capacitor bank was charged to an initial voltage of 250 V, which corresponds to a stored energy of 656 J. Figure 2.2(a) shows the transients for the arc current I, capacitor bank voltage V_{cap}, and breech voltage V_{breech}. The capac-

itor voltage discharges from 250 V to approximately 80 V at the end of the transient, corresponding to a total energy of 580 J delivered to combination of the discharge and the resistive load of the circuit. The energy delivered to the discharge alone may be calculated by the relationship,

$$E_{discharge} = \int V_{breech} I^2 dt. \tag{2.4}$$

$E_{discharge}$ was found to be ∼350 J of the 580 J delivered to the whole circuit. The overall discharge time was found to be ∼19 ms, which is significantly longer than the 5 ms half-cycle time of the pulse forming network. The current waveform in Figure 2.2(a) also indicates that the discharge follows the response of a typical RLC circuit until 3 ms, when a discontinuity in the current slope and breech voltage occurs. These discontinuities at t∼3 ms and t∼8.5 ms prolong the discharge time by decreasing the rate of decay of the current draw. Previous studies have shown that such rapid drops in voltage correspond to jumps in the anode arc root location and associated erosion of the anode material [48, 52]. Both claims have been confirmed here by correlating the anode erosion damage locations on the rails with the locations of anode root anchoring in the high-speed images.

The behavior of the transient arc can be observed from the high-speed images in Figure 2.3, which show the motion of the luminous arc along the rails. The intensity of the arc is strongest near the arc roots and less bright

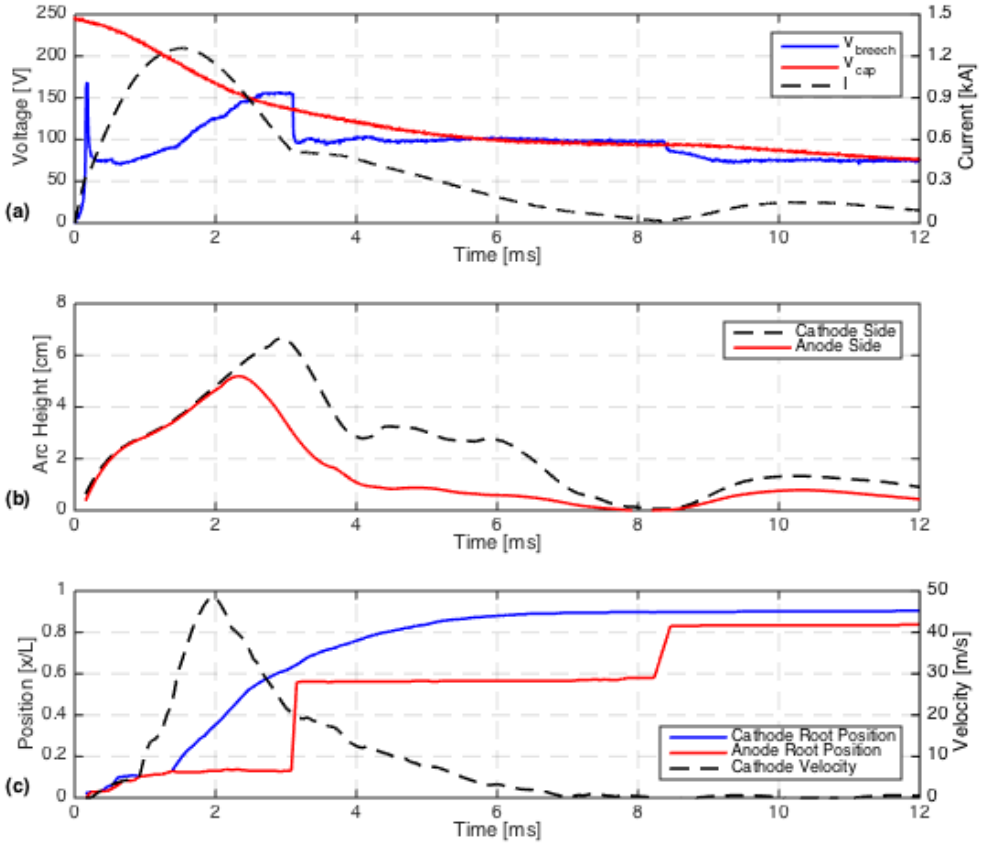

Figure 2.2: (a) Electrical characteristics of the arc, (b) Discharge column height, and (c) Arc root positions and cathode root velocity. Notice that the peak current in (a) occurs during the strong initial acceleration of the arc and precedes the peak velocity in (c). The connections between the anode root jump at 3 ms in (c) and the breech voltage drop in (a) is clearly visible here.

at points in the arc further away from the surface. The arc column appears as a luminescent cloud that diffuses throughout the current-path of the arc. Unfortunately, it is difficult to distinguish the part of this luminous cloud that is current-carrying ionized plasma from the part that is strongly radiating non-ionized gas. Parker [62] has shown that in railgun applications a significant portion of the luminous cloud is non-ionized or weakly-ionized and does not carry significant current across the electrodes. Imaging of the luminous cloud is therefore not a definite measure of the location of the current-carrying arc, so the location of the cloud can only be used as a bound for the outer edge of the arc column.

The arc column height, h, arc root positions, x, and propagation velocity, u, were interpreted from the high-speed images shown in Figure 2.3. These results are shown in Figure 2.2(b) and 2.2(c). Due to the discontinuous jumps in the anode root motion, the cathode root motion was used to approximate the propagation velocity of the arc. Closer analysis reveals that several of the observed arc characteristics are consistent with the measured current, particularly the acceleration of the arc which shares its peak with the maximum current of the discharge. This is an expected result given that the Lorentz force is proportional to the square of the current. The local arc velocity, which depends on the arc acceleration, is also (indirectly) affected by the arcs current.

The arc height and the breech voltage of the arc are also related to one another. The maximum height of the discharge increases as the voltage

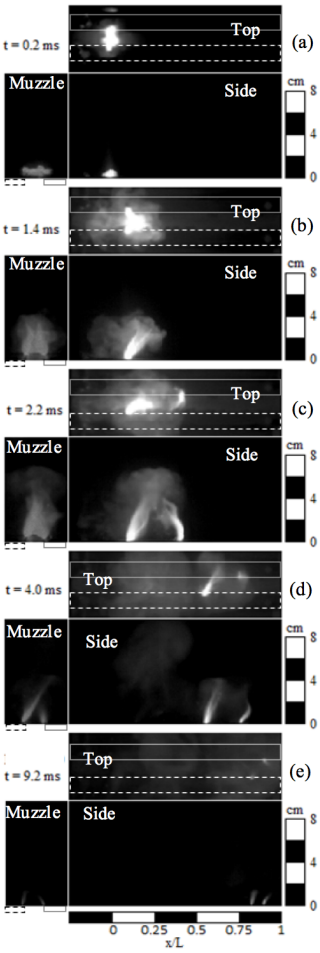

Figure 2.3: High-speed images of the arc transit. Each subfigure shows the top, side, and muzzle view of the propogating arc at a single time. Scales showing the height above the rail surface and the normalized distance traveled are shown at the sides of each image. The dashed lines mark the location of the anode while the solid lines mark the location of the cathode. The initiation stage spans (a) and (b), the main transit stage occurs in (c) and (d), while the quenching stage occurs in (e).

increases and then begins to fall immediately after the first drop in breech voltage shown in Figure 2.2(a) and Figure 2.2(b) at around 3 ms.

The arcs transit may be classified into three stages based on the geometric and electrical properties of the arc. The initiation stage corresponds to the ignition of the arc at the time of the trigger and the transit duration around 1 ms after the trigger. It can be characterized by the acceleration of a coherent arc column. In this stage, the breech voltage initially spikes and then remains relatively steady or increases marginally (by no more than $\sim$20 V), while the current rapidly increases. The main transit stage is marked by a smooth transit of the cathode root and discontinuous jumps of the anode root. The jumps cause fluctuations in the breech voltage and current throughout the main transit stage. The end of the transit shows quenching of the arc, as evidenced by reduction in arc intensity and current.

2.3.1 Initiation Stage

The breech voltage in Figure 2.2(a) contains a large initial peak at t$\sim$0.1 ms corresponding to the vaporization of the initiation wire. After this peak, the breech voltage drops to $\sim$80 V and then gradually increases during the initiation stage. The images in Figure 2.3 show the formation of a single coherent arc column between the electrodes at t$\sim$0.2 ms. This arc column immediately experiences a large acceleration along the rails due to the Lorentz force. During the initial transit, the anode and cathode arc roots propagate as a single column. The initiation stage is specifically defined by the period where

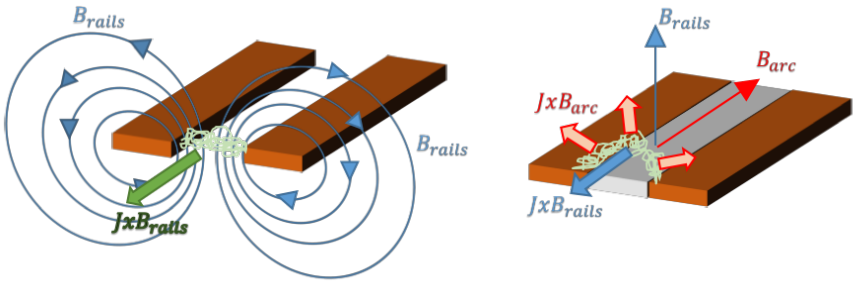

Figure 2.4: The arc on the left is allowed to stay between the electrodes and thus has no force component in the vertical direction. The arc on the right has been forced out of the plane by the surface between the rails. In this case, the arc induces its own magnetic field, B_{arc}, parallel to the rails and orthogonal to the field induced by the current passing through the rails. This causes a Lorentz force on the arc perpendicular to the surface, pushing it upward and outward.

the roots form and then propagate together in this concerted fashion. This concerted propagation can be seen in the image at t∼1.4 ms in Figure 2.3. The arc column grows in height (Figure 2.2(b)) with increasing arc current and forms an arch-like shape above the surface.

The deflection of the arc away from the surface, evident in Figure 2.3, can be explained by geometric factors and the consequent electromagnetic forces. Figure 2.4 presents a schematic of the arc structure and the forces acting on the arc for a symmetric case where there is no insulating surface between the electrodes, as well as for a case like RailPAc with an insulating surface and flush-mounted electrodes. The presence of the insulating surface creates an initial distortion of the arc column into the open air, but this distortion is immediately magnified by the same self-blowing effect that pushes the

arc down the rails. When the arc is in plane with all current localized between the electrodes, the only force on the arc is the forward Lorentz force in the same direction as the electrode length. However, if the arc is displaced such that some current comes out of plane, the magnetic field in the area of the plasma develops a component which points towards the breech. The arc current then interacts with this field, resulting in an expansion of the arc upward and outward. Due to the field enhancement at the edges of the rail electrodes, the arc roots are not always noticeably affected by this force. However, the plasma column always rises upward as the current reaches peak values and enters into the main transit stage. It is likely that this effect is aided by the gas expansion effects described in [49, 54, 56]. The arc heats the gas around it, causing the gas to expand and push the arc away from the surface.

2.3.2 Main Transit Stage

The main transit stage begins after about 2 ms as shown in Figure 2.3. The arc current reaches a peak value of 1.3 kA at around 2 ms and the arc velocity reaches a peak value of $\sim$50 m/s during the later part of the transit at around 5 ms. The single coherent arc observed in the initiation stage is transformed to a diffuse column between the electrodes. This column cannot be observed at all times because of the surrounding luminous cloud, however, the cathode and anode arc roots regions are clearly visible throughout the transit.

The discharge columns extends away from the surface until the first

sharp drop in breech voltage at around 3 ms, after which point the columns begin to decrease in height. As shown in Figure 2.2(b), the cloud extends almost 7 cm away from the surface at its peak height. This suggests that a large region of surrounding quiescent air is affected by the arc transit, i.e. the flow actuation effect can extend several centimeters away from the surface (a desirable feature for surface plasma actuators). The height of the arc above each electrode is independently estimated by finding the cloud height at the respective locations of the arc roots. It can be seen in Figure 2.3(d) that the anode side of the arc column has higher intensity and height than the cathode side of the arc column.

During the main transit stage, the cathode root moves smoothly along the cathode, while the anode root periodically anchors on the anode surface and then jumps forward to catch up to the cathode root. The anode root never leads ahead of the cathode root in this stage. The motion of the anode root is punctuated by the formation of a new anode root directly across from the cathode root whenever the distance between the arc roots is increased. Indeed, the arc column splits to allow the existence of two anode roots to appear simultaneously with the 2 μs exposure time of the camera used. As the new anode root forms, the original anode root is extinguished. The time and location of this process is not consistent from one firing to another. However, the arc current and breech voltage measurements show consistent trends with regards to the formation and destruction of the anode roots.

The anode root jump occurs consistently after the peak arc current dur-

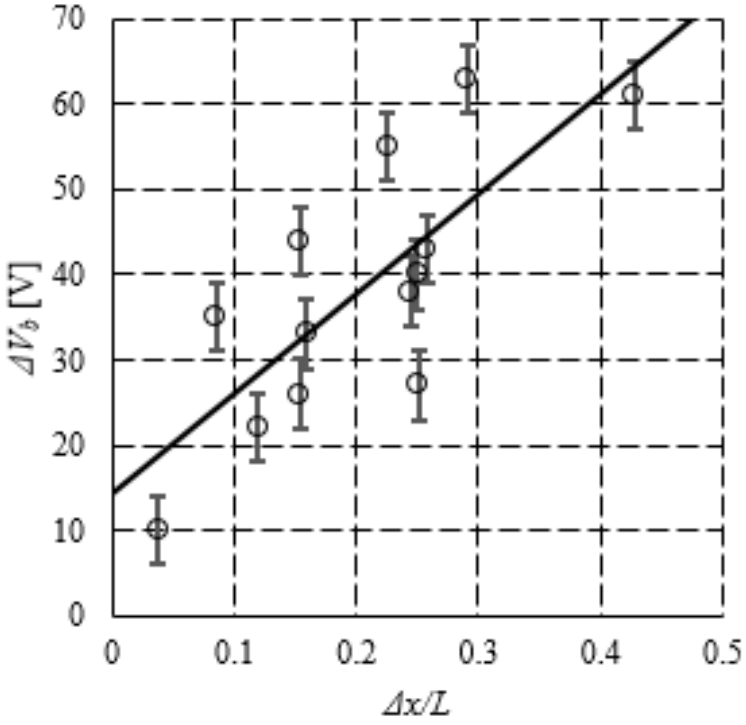

Figure 2.5: Breech voltage drop as a function of arc root jump distance.

ing the decreasing phase of the current. Before the jump, the distance between the anode and cathode roots increases because the anode root is anchored to the electrode while the cathode root continues to move forward smoothly. As the roots move further apart the arc must necessarily lengthen, which increases the electrical resistance of the arc. This increase in the arcs electrical resistance works to decrease the current passing through the circuit, however, the circuits inductance minimizes this change in current by generating an inductive EMF to match the rise in resistance. This electromotive force from the circuit inductance serves to directly maintain the arc current at constant values on

timescales less than the natural frequency of the RLC circuit. As a result, the breech voltage rises proportionally to the arc resistance. As the breech voltage ramps up to its threshold value, which varies from shot to shot, the anode root jumps to a new location closer to the cathode root. Following the jump, the breech voltage drops to a lower value and is nearly steady for the remainder of the discharge.

Figure 2.5 shows the breech voltage drop as a function of the anode arc root jump distance, over a number of firings. A clear correlation is found with the breech voltage drop increasing nearly linearly as the anode root jump distance increases. This drop in voltage is a direct consequence of a decrease in the arc resistance each time the anode root jumps. The scatter in the data is attributed to the fact that the current path distance is not neccesarily a straight line through the arc roots. As a result of the breech voltage drop, the current slope suddenly changes from negative to zero at the jump. The arc column height also drops and then re-expands upward after the jump, as shown in Figure 2.2(b).

Arc anchoring and subsequent movement in the RailPAc seems to be analogous to models for arc movement in low voltage circuit breakers described above [49, 50]. On the cathode, the root moves by a multitude of very small jumps, which are often not discernible by camera but do seem to occur as evidenced by the small closely-spaced spots of arc damage on the cathode rail surface. While the cathode root moves forward smoothly, the anode root anchors for long periods of time as described in [52]. This stretches the arc

column down the surface of the RailPAc and populates the area downstream from the anchored anode root with excited/ionized gas. It is believed that this gas facilitates the new arc root. Meanwhile, the increase in arc resistance due to the increasing arc length makes the current prefer a shorter, less resistive path between the roots.

At some threshold condition, due to a combination of the effects listed above, the anode jump occurs. All of the current immediately begins passing through the new anode root, which is closer to the cathode root and allows a less resistive path. The old anode root ceases to exist as described by Haug [63]. The model described above explains the drop in height seen when the anode root makes its jump, since a lower arc column is a shorter current-path.

Anode jumping behavior does not seem to be a strong function of current in the regimes studies here, as compared to transit velocity which does scale with current as shown in [61]. However, given that the jumping behavior is not observed in the high current regimes used by railguns it may be that it is a weak function of current.

2.3.3 Quenching Stage

The quenching stage begins when the discharge current has dropped to a sufficient small value. For low currents the Lorentz forcing is weak and the arc column ceases motion. This stage begins after 6 ms in Figure 2.2 and in Figure 2.3(e). A continuous reduction in luminosity and column height is seen during this stage. Although the root positions are fixed, the column tilts

towards the muzzle end of the rails as the top of the column continues to be pushed by the weak Lorentz force. However, the roots are sufficiently anchored to resist movement. While the breech voltage is constant, the current decays to zero and the arc resistance increases until the plasma arc is completely extinguished.

In some cases, the anode root jumps once more during the quenching stage. However, the arc formation-destruction process at this stage is different from the one observed in the main transit stage. First, the cathode root does not exhibit motion before the anode jump. Second, the breech voltage does not increase prior to the jump because the arc roots are fixed and the jump occurs at a lower threshold voltage. It is clear from the comparison between the two transit stages that the increase in breech voltage is related to the increase in the relative distance between the arc roots. It appears that the reduction in current in this stage increases the time needed to reach the critical number density of charged species compared to the main transit stage.

2.3.4 Rail Damage

Images of the rail electrodes after a single firing and after five firings are shown in Figure 2.6. The arc causes substantial damage to the surface of the electrodes, concentrated around the edges of the electrodes and most intensely on the anode side. Damage on the electrodes is concentrated around the initiation region for the first few firings, but subsequent firings extend the damage towards the muzzle end. The severity of damage also increases with

Figure 2.6: Comparison of electrode topologies after the first firing (top) and the fifth firing (bottom). Notice the continuous damage on the cathode side and the spot damage on the anode side.

the number of firings.

A closer observation of the rails reveals two types of surface damage. While the cathode side is characterized by a continuous track of dark residue along the transit direction, the anode side is punctuated by anode root anchoring pits of varying shapes and sizes. Surrounding these pits are marks of copper residue left on the ceramic surface, which extend away from the rails towards the opposite electrode. The formation of anode erosion pits correspond to the anchorage of the anode roots at these positions along the rails. Copper residue is also deposited on the ceramic surface of the cathode side, however, the damage is smaller and the residue does not extend as far as the anode side. The difference is a consequence of the dwell time of the respective arc roots at any given location on the electrodes. A longer dwell time (in the

case of the anode root) at a given location results in large energy transfer to the eletrodes an consequently greater erosion damage. Similar observations were made by Teste et al. [52] in their study of arc root motion over anode and cathode surfaces. Interestingly the damage is spread out. One might expect the arc to preferentially attach (and cause damage) to the same location on each passing. The exact opposite is found however. The are attaches a different place on each firing and subsequently damages a different part of the electrode each time. The most likely explanation for this seems to be variable resistivity of the oxidation layer. The attached arc creates a thick oxidation layer making it less attractive as an attachment site for later arc passages. This will be discussed in more detail in Chapter 6.

While some quantities remain the same, there are considerable variations in arc transit characteristics from one RailPAc firing to another, and the exact characteristics of the arc transit are never fully repeatable. The peak current and peak resistance of the arc are nearly constant from one shot to the next, however, most other quantities vary considerably. The maximum velocity as well as the distance traveled by the arc before quenching are variable. The time it takes for the arc to cease discharging is also variable, as is the number of jumps that the anode root makes. Interestingly, despite the expectation that the anode spot damage locations should act as field enhancement points which may make them attractive arc root anchoring points, the number and location of jumps made seems to have no correlation with pre-existing rail damage.

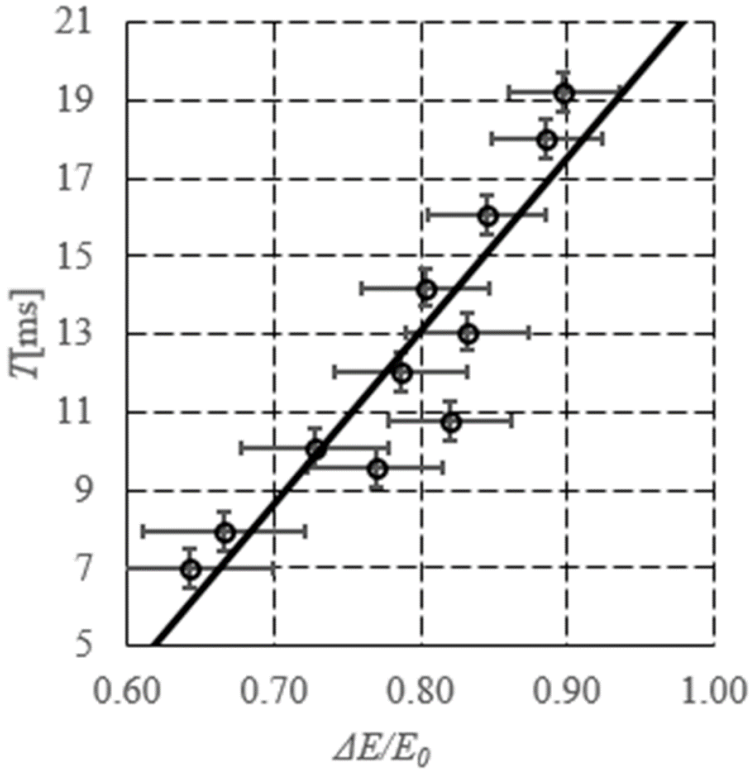

Figure 2.7: Arcing duration as a function of drops in capacitor energy normalized by the initial capacitor energy.

The arc transit duration is found to correlate well with the energy discharged by the capacitor. Figure 2.7 plots the arcing duration as a function of the energy discharged by the capacitor, ΔE, normalized by the initial capacitor energy (E_0). The minimum sustain voltage drop of the arc is relatively constant since it is largely based on the spacing of the rails. The capacitor bank can only continue to drive the arc if the bank is at a higher voltage than the minimum sustain voltage drop, so once the bank voltage drops below the

sustain voltage of the arc, the arc will quench. Observation of the current and capacitor voltage waveform in Figure 2.2(a) and of the pulse generator layout suggests that the circuit behaves like an overdamped RLC circuit. The capacitor bank energy in an ideal RLC circuit should decay exponentially as shown below,

$$ln\left(1+\frac{\Delta E}{E_0}\right) \propto -t. \tag{2.5}$$

The RailPAc experimental data in Figure 2.7 shows that the capacitor bank energy decay follows the above ideal relationship.

2.3.5 Spectroscopy

Spectroscopy measurements allow for the determination of the species present in the arc during its transit. Species detected include atomic oxygen, atomic nitrogen, molecular nitrogen, atomic hydrogen, and atomic copper. Oxygen and nitrogen species are entrained directly from the surrounding air, while the presence of hydrogen is explained by breakdown of atmospheric water. Loss of the signal was not analyzed in a dried environment however, the signal is strengthened in the presence of actively humidified air. Copper appears because it is present in the exploding initiation wire and is eroded from the copper rail electrodes. Oxygen, hydrogen, and copper are all strong emitters but hydrogen has only two strong lines in the region analyzed, making it a poor candidate for spectral analysis. Our spectral analysis thus concentrates

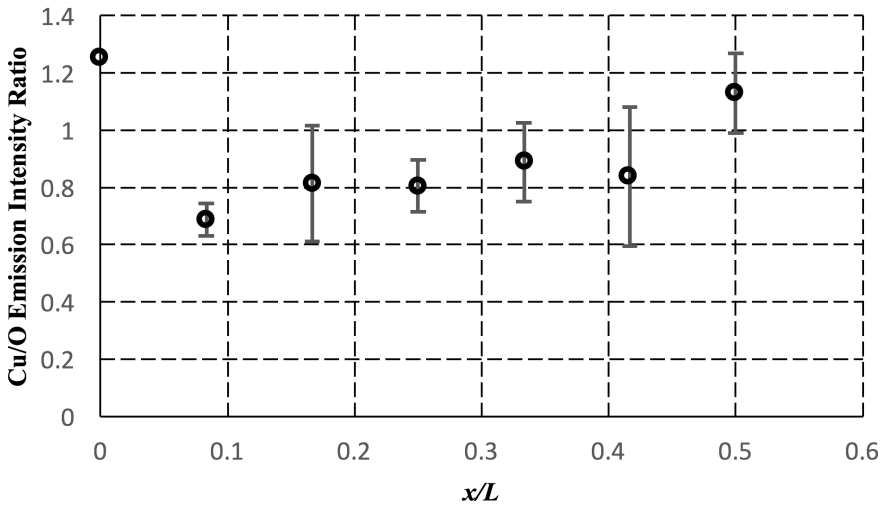

Figure 2.8: Relative ratio of visible copper emission to oxygen emission.

on oxygen and copper species.

While the exact ratio of all of the species could not be determined from simple spectral data, relative increases and decreases in the ratio of species in the arc can be estimated. This is done by comparing the total emission in the region of interest for different species at multiple points in the transit. Values were computed for the strongest emitters, oxygen and copper, and are shown in Figure 2.8. The results suggest that there is a relatively high amount of copper present at the initiation (due to the exploding wire), and then oxygen is entrained into the arc in the first couple of centimeters of transit while copper vapor from the exploding wire condenses on the railpac surface, which corresponds roughly to the initiation phase described previously. This condensed copper is visible on the ceramic surface of the RailPAc after repeated

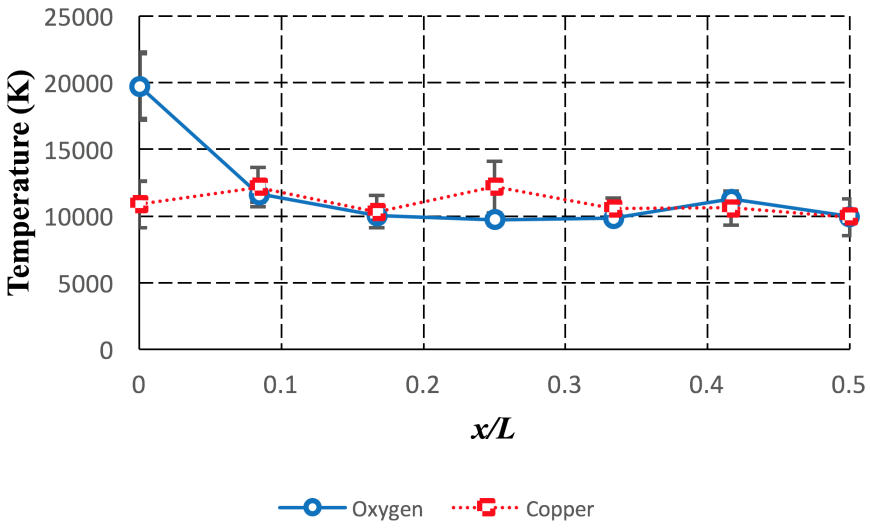

Figure 2.9: Temperature estimates of the arc using copper and oxygen species emission lines. Notice that the temperature is more or less constant after the initiation of the arc

firings. Most of the main transit is captured and shows a steady increase in copper relative to oxygen due to erosion of copper from the electrodes. The quench phase is not bright enough for analysis with the current setup and would require more complex analysis, since the arc is not expected to be at LTE.

Temperature estimates were obtained using the normalized Boltzmann plot method described earlier and are shown graphically in Figure 2.9. Estimates of temperature were made using copper and oxygen. Measurements at the arc initiation (x/L = 0) for oxygen are not reliable because the system is likely not at LTE conditions during this time and the high density of copper

vapor at this stage increases the likelihood of self-absorption of photons by the plasma column. This is also evident in Figure 2.8, which shows that the timescales for entraining oxygen into the arc and removing the initial deposit of copper from the fuse wire are non-negligible compared to the timescales associated with the arc transit. Arc temperature appears nearly constant at about 10,000 K through the first two stages of the transit.

While self-absorption of copper is possible and could lead to incorrect estimates of temperature, self-absorption of oxygen to generate a consistent change in temperature such that both elements create an equal systematic error in the temperature estimate is extremely unlikely. Since both copper and oxygen measurements show approximately the same temperature through the arcs transition the most logical conclusion is that self-absorption is negligible for both species for most points in the main transit of the arc with the exception of the initiation where the calculated temperatures of the two species do not match. The error bars in Figure 2.9 are given by the standard deviation of normalized Boltzmann plotting method used. The small error bars suggest that the RailPAcs temperature is reproducible because the measurements span multiple firings. As with species concentration, no measurements were taken further down the rails because emission of the arc past this point suggests that the arc is not at LTE during the quench phase.

One might expect the variation in concentration of copper in the arc to have an effect on the temperature of the arc as discussed in [64]. However, since the methods used in that work could not resolve temperature changes

through the arc and only captured an average temperature for the whole arc column, a variation in temperature of the level described in [64] would be smaller than the error bounds for the temperature measurements shown in Figure 2.9. Our results show that the arc temperature remains relatively constant throughout the duration of the transient with very little sensitivity to the arc current. Other work in the literature corroborates our observation that for arc currents above ∼200A the arc temperature is only a relatively weak function of current [17–20]. This is because changes in the temperature occur due to either changes in heating, or changes in cooling. Joule heating in the arc is given by $Q = \vec{J} \cdot \vec{E}$. Higher current arcs tend to expand in size to accomodate more current rather than increasing local current density so heating rates are unaffected. At the same time radiative losses are proportional to T^4 so as the temperature increases it becomes significantly more difficult to increase the temperature further. Temperature will thus become more strongly a function of gas composition, which affects radiation characteristics, than electromagnetic parameters.

Chapter 3

Simple Modifications to Baseline RailPAc Geometry

The characterization in the previous chapter covered a single RailPAc configuration with varied electrical inputs. Varying electrical inputs is the simplest means of modification of actuation parameters. However, there are a variety of additional ways in which the actuator can be modified. The electrode material can be changed. The electrode size or spacing can be changed. An external field can be applied, or the induced field may be multiplied. All of these modifications can significantly change the operation of the RailPAc. Analysis of these changes is presented here.

3.1 Electrode Material

Experiments in electrode variation included the use of tungsten, copper, and the Cu-W composite Elkonite. Tungsten is often used for welding electrodes and, in previous experiments, showed minimal damage when employed for gliding arcs using free-floating electrodes (discussed in more detail in Chapter 4)[61]. However, despite tungsten's higher melting point, tungsten plate electrodes for flush mounted RailPAcs were destroyed much faster than

copper electrodes, with extreme melting at the electrode edges. This higher damage level is believed to be due to higher Joule heating in the metal due to tungsten's lower conductivity. Copper anodes showed significant surface damage after repeated firings as well, though not to the same degree as tungsten. Elkonite anodes, meanwhile, showed minimal melting and no topological changes to the electrode surface even after repeated firings. Elkonite cathodes showed similar wear to copper cathodes but did not oxidize as readily as the copper. No noticeable variation in transit speed was noted for any of the materials tested.

In the initiation phase of the arc, there is often a lag between the ignition of the arc and the initial movement of the arc. This is called residence time in the literature. Previous work found that electrode material, and specifically the evaporation rate of the metal, had a strong effect on the residence time of a gliding arc root [53]. With 1 cm wide rails, spaced 13 mm apart, sanded prior to each firing, we observed no variation in residence time between copper, tungsten, and Elkonite.

The study concluded that Elkonite is the superior choice for RailPAc electrodes for durability purposes, however, the difficulty of machining Elkonite prevented significant experimental exploration of Elkonite as an electrode material. Elkonite electrodes also did not display the same oxidation enhancement effects present when using copper anodes, as discussed later in Chapter 5.

Copper electrodes and tungsten electrodes were manufactured by shearing rolled copper and tungsten plates. Elkonite electrodes were cut from re-

purposed Elkonite rail-gun armatures using carbide blades.

3.2 External Fields and Enhanced Fields

Since the current of the arc passes primarily in the dimension normal to the length of the electrodes (we will refer to this as the x-direction as in Figure 1.2), there are two orientations of applied magnetic field which can be used to affect the arc. Magnetic fields applied along the muzzle-breach axis (y-direction) will result in forces which would either expand the arc upward and away from the RailPAc surface, or pull it down to the surface. A wire configuration generating such a field is shown in Figure 3.1a. Magnetic fields applied normal to the surface of the RailPAc will enhance or diminish the primary induced field, speeding up or slowing down the transit of the arc, respectively. A wire configuration generating a normal directed field is shown in Figure 3.1b

Significant manipulation of the axial magnetic field is difficult. To be an effective control method in the practical use of the RailPAc, the field must be generated in the region below the RailPAc. The most effective (reasonable) means of creating an axial external field, without impeding the flow around the RailPAc, is a solenoidal magnet submerged below the surface of the RailPAc. However, solenoidal fields outside of the solenoid go like $B \sim 1/r^3$ moving away from the solenoid along the midline of the solenoid [65]. Pathak gives the explicit expression for the field as,

$$B_{axial} = \frac{nIA\mu_0}{4\pi}\left[\frac{y - L/2}{((y - L/2)^2 + r^2)^{3/2}} - \frac{y + L/2}{((y + L/2)^2 + r^2)^{3/2}}\right], \qquad (3.1)$$

where r is the distance from the centerline of the solenoid in the plane normal to the solenoid's axis, y is the axial coordinate along the solenoid, L is the length of the solenoid, I is the integrated current, A is the solenoid cross sectional area, and n is the number of turns. If the solenoid is run in series with the RailPAc, the magnetic field for a solenoid with 100 turns and a radius of 2 mm will generate a magnetic field between $10^{-5}T$ and $10^{-3}T$ for points 0.5-10 cm away. Compare this to the much larger primary field of the RailPAc which should be $\sim 10^{-1}T$. The existing axial field should be slightly smaller but of the same order. Surprisingly, despite this disparity of field strength, a solenoid of this size and shape does have a significant effect on the RailPAc arc's upward expansion rate.

Experiments were conducted with a solenoid with 100 turns, a length of 10 cm, and a diameter of 7 mm. The solenoid was placed $\sim$ 2 mm below the plane of the RailPAc. Conditions of the RailPAc were otherwise identical to those described in Chapter 2. The average arc height was 2.6 cm for control cases where the solenoid was removed from the vicinity of the RailPAc but was still electrically in series with the RailPAc arc to maintain inductance. The solenoid had no discernible effect on the arc height when the field was oriented to pull the arc towards the RailPAc surface, however, when oriented to increase the height of the arc, an average height of 3.6 cm was found. Maximum

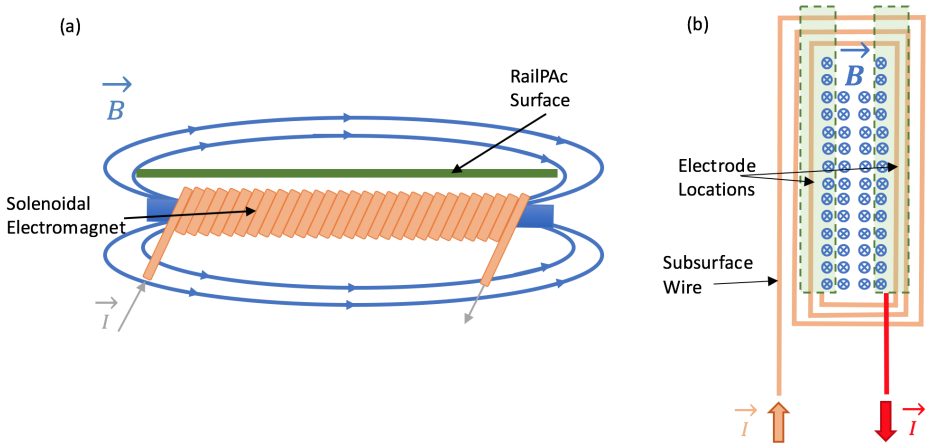

Figure 3.1: RailPAc Wire Configurations for Field Modification with muzzle directed field configuration shown in (a) and a normally directed field configuration shown in (b).

heights were much higher around 7 cm. Interestingly the column being pushed away significantly impaired the arc's ability to restrike with almost no restrike occuring when the arc was pushed away from the surface. The arc was also significantly slower moving when pushed away from the surface, only traversing a few centimeters of the electrodes if it moved at all, compared to the $\sim$ 10 cm transits of the other cases. The ability of the solenoid to force the arc up but not down is likely due to the instability of the arc column. A small additional push upward when the arc is near the surface of the RailPAc makes the secondary induced field grow faster, resulting in the arc quickly expanding upward. However, the solenoid field is not nearly strong enough to overcome the existing secondary induced field, so it cannot pull the arc towards the

surface.

Normal magnetic fields can be much more easily augmented. By running one of the input wires directly under the electrodes to form a simple coil underneath the RailPAc surface, we can multiply the RailPAc's existing primary induced field by the number of additional turns we fit under the surface. Experiments were performed with the same geometric parameters as in Chapter 2 but with a coil submerged below the RailPAc surface. Control cases were run and between 1 and 6 turns in the coil were tested. Results for the effect on velocity are shown in Figure 3.2 where $B/B_0 = 1$ corresponds to the control case while $B/B_0 = 7$ would be the full 6 turns of wire below the surface.

A roughly linear increase in velocity is visible with some diminishing returns for the highest fields. The behavior of the arc also changes significantly. The arc attachment site on the electrodes tends to switch from the inner edge to the outer edge for $B/B_0 > 3$. The anode root also ceases anchoring above this value, moving smoothly along the surface, an ideal characteristic for the actuator arc. Restrike rates are dramatically increased for $B/B_0 > 4$ and the arc takes on a more diffuse appearance. This rapid restriking explains the leveling off of the average velocity for these values of the magnetic field. The arc continues to move faster at any given point for larger magnetic fields, but because the arc frequently restrikes back towards the breech of the RailPAc the arc effectively has to travel a larger distance, which results in a slower average velocity.

The effects of the normal applied magnetic field can be duplicated by

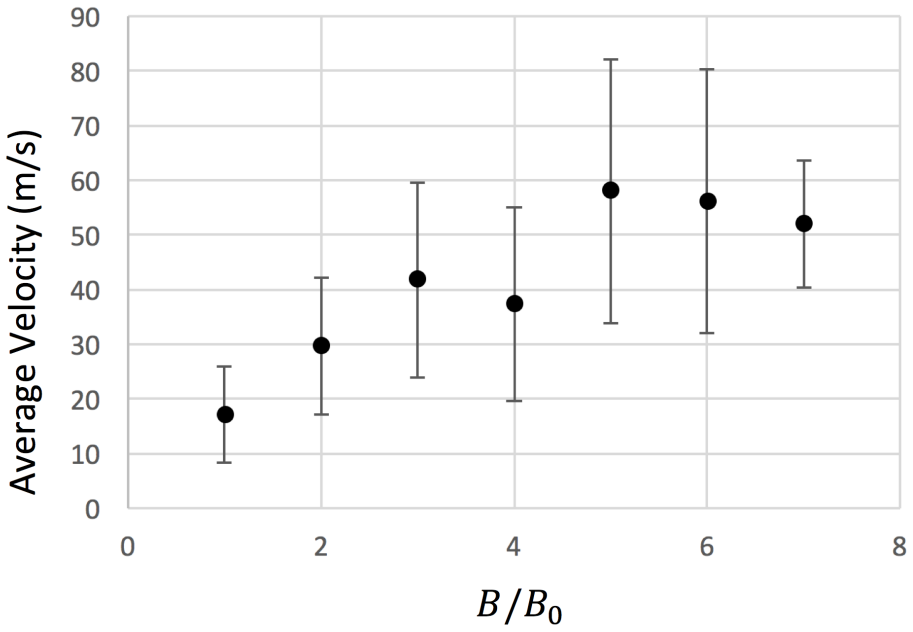

Figure 3.2: Average velocity for enhanced RailPAc for several external magnetic field enhancement ratios.

use of permanent neodymium magnets submerged below the surface of the RailPAc, although using permanent magnets is considerably more bulky than using additional wire turns for a given effect. Using 4 1x1x0.1 in magnets, a similar effect to a single turn of wire below the RailPAc was achieved. The field due to these is oriented such that the north side of the magnets are all pointed up through the surface of the RailPAc. This enhances the field normal to the surface everywhere directly above the magnets. Permanent magnets might be useful for constructing more efficient, low current RailPAcs since the induced fields drop linearly with the current but an applied field from an external magnet can be maintained independently.

3.3 Electrode Spacing

Fundamentally, all of the momentum delivered by the RailPAc to the surrounding flow is initially contained in the electromagnetic fields of the RailPAc circuit. This electromagnetic momentum couples with the flow through the arc and is converted to fluid momentum. The coupling is complicated and difficult to analyze. Momentum contained in electromagnetic fields, however, is quite easy to analyze through use of the Maxwell stress tensor, σ_{ij}, given by,

$$\sigma_{ij} = \epsilon_0 E_i E_j + \frac{1}{\mu_0} B_i B_j - \frac{1}{2}\left(\epsilon_0 E^2 + \frac{1}{\mu_0} B^2\right)\delta_{ij} \tag{3.2}$$

where E is the electric field, B is the magnetic field, ϵ_0 is the electrical permitivity of free space, and μ_0 is the vacuum magnetic permeability. To find

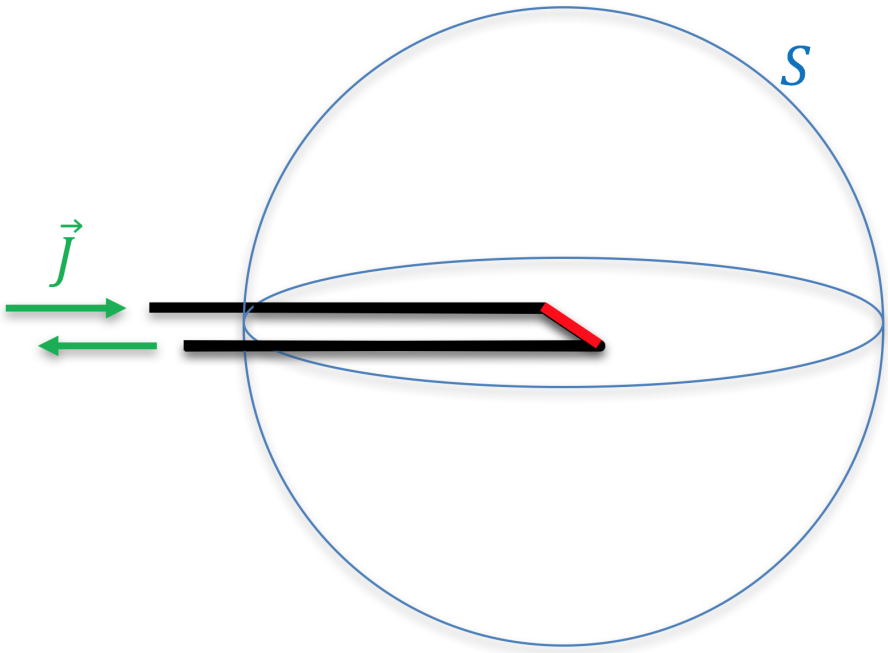

Figure 3.3: Control surface, S, for a current half loop. The long arms of the wire are black and the cross piece analogous to the arc is red.

a body force from the fields we take the divergence of the stress tensor,

$$f = \nabla \cdot \sigma. \tag{3.3}$$

This can be converted to a total force by integrating over the volume and applying Gauss's Theorem over some control surface, S, to arrive at,

$$F = \iint_S \sigma \cdot dS. \tag{3.4}$$

Thus, the net force delivered to a volume can be determined from the fields on the surface of the volume. If we have a situation like the one shown in

Figure 3.3 where we want to know the force delivered by a current configuration with two long electrodes and a cross piece (representing the arc), we must calculate the values of the electromagnetic fields generated by the cross piece and the two electrodes. The electric fields are trivially zero everywhere but the inside of the electrodes since the system has no net charge. It is also clear by symmetry that the net force can only be in the direction along the electrodes. Analysis of the magnetic field is slightly more complicated. Examining the field generated by the cross piece which stands in for the arc first, we can use the exterior solution for the field from a segment of current. The maximum magnetic field for a given distance from the wire will be generated in the plane normal to the segment intersecting the midpoint of the current segment. The value will be given by,

$$B = \frac{\mu_0 I}{2\pi} \frac{L}{R^2 \sqrt{\frac{L^2}{R^2} + 1}} \tag{3.5}$$

where L is the length of the segment and R is the distance from the wire. If we expand the last term for $\frac{L}{R} << 1$ we get

$$B = \frac{\mu_0 I}{2\pi} \frac{L}{R^2} \left(1 - \frac{L^2}{2R^2} + \mathcal{O}(\frac{1}{R^3}) \right) \tag{3.6}$$

So, to first order, the magnetic field goes as $\frac{1}{R^2}$. This field is entirely in the azimuthal direction so $B_i B_j = 0$ if $i \neq j$. If we take the radius of our control volume to be very large, the magnetic fields of the long electrodes will be identical to the field due to an infinite wire. Splitting up the contributions

to the total force from the fields due to the electrodes and the fields due to the arc, we obtain the expression,

$$F_{arc\ fields} = \int \frac{B^2}{2\mu_0} R^2 d\Omega \sim \int \frac{1}{R^2} d\Omega. \tag{3.7}$$

If we draw a sufficiently large control surface, the force will only depend on the magnetic field due to the wires punching through the surface since the arc's magnetic field squared will decay faster (R^{-4}) than the surface area grows (R^2). Thus, the only changes which can be made here to augment force are the rail spacing, the diameter of the rails, and the current input. The actual shape of the arc is clearly immaterial, provided its length is significantly smaller than the length of the electrodes.

An even stronger statement can be made if we require that the arc stays in a plane normal to the electrodes. Such an arc will generate the same force regardless of its shape, and will depend only on the length and spacing of the electrodes. The argument is as follows. We require that $J_z = 0$, where z is the coordinate along the electrodes, since there is no extension of the arc up or downstream. We can also say that $B_z = 0$ since we only care about the field from the electrodes which only generated x and y components of the field. We can ignore fields from the arc itself since by momentum conservation it cannot push itself in the z direction if J has no dependence on z. If the integral,

$$F_z = \int J \times B \ dV \tag{3.8}$$

is path independent for J we must show that $\vec{J} \times \vec{B}$ is a conservative field, or equivalently, that

$$\vec{\nabla} \times (\vec{J} \times \vec{B}) = 0. \tag{3.9}$$

If $\vec{J} \times \vec{B}$ is calculated explicitly with $J_z = 0$ and $B_z = 0$ we find that F_x and F_y are both zero. Thus, $\nabla \times F = 0$ and the curl of the net force on the arc due to the induced field of the rails is naturally zero. So, provided that the arc is either symmetric in the direction of propagation, or the electrodes are very long relative to the interelectrode spacing, the total force imparted by the arc is independent of the specific shape of the arc and depends only on the total spacing of the electrodes and the location of the arc along the electrodes.

To get an idea of when we can start making the assumption that the forcing is entirely dependent on electrode spacing independent of electrode length, we can solve the total force on a short "arc" current segment due to two variable length "electrode" current segments. The force for a 1000 A arc becomes nearly constant after only a few centimeters for electrode spacings between 2 and 20 mm, as shown in Figure 3.4. Note that equation 3.3 is singular at the origin so an electrode radius must be assumed. For this case round electrodes with 1mm radii were assumed. It should be noted that while total force increases with arc length, the force per unit length of arc has the trend

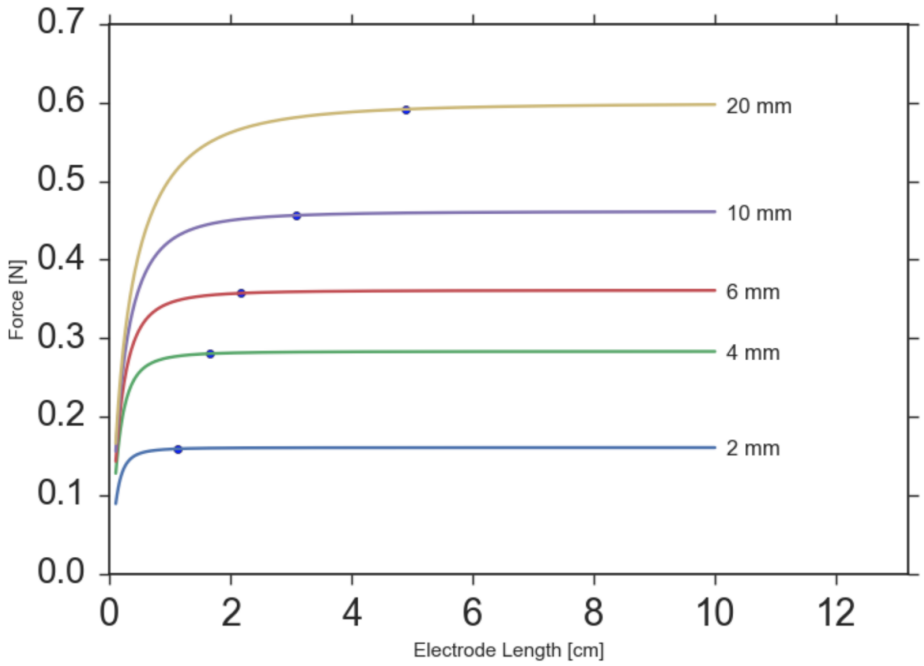

Figure 3.4: Forcing for different electrode spacings with variable electrode length. The point where 99% of max forcing is reached for each case is indicated with a point.

reversed with shorter arcs producing higher average force. This is because the average induced magnetic field between the electrodes falls off like $\sim ln(w)/w$ for a given interelectrode width, w.

The effect of skewing the arc so that one root moves forward while the other stays in place can also be examined by this simple model. We find that after a few centimeters the arc again becomes independent of the electrode length regardless of skew. Initially, total forcing is slightly depleted for skewed arcs compared to unskewed arcs, but eventually reaches the same

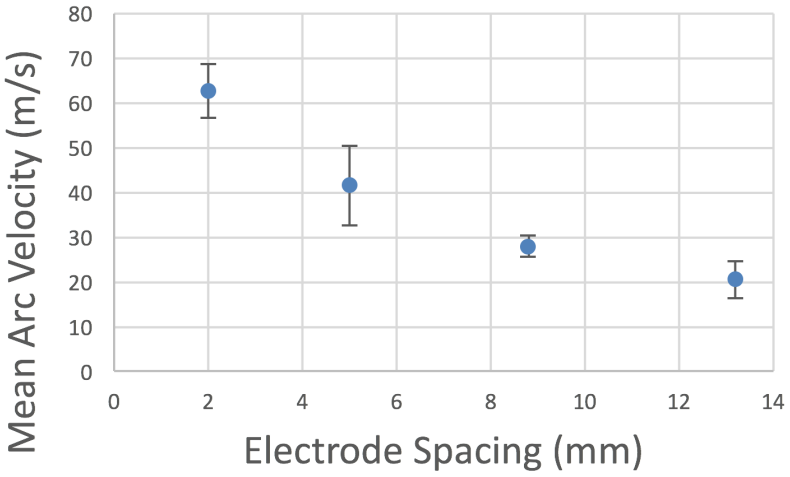

Figure 3.5: Velocity of the arc for 4 different electrode spacings.

value regardless of skew. The results in Figure 3.4 also show the validity of our assumption to take the radius of the sphere in Figure 3.3 to infinity. The electrodes in Figure 3.4 begin to behave as infinite electrodes with an electrode length between 3 and 5 times longer than the arc length.

3.3.1 Spacing Experiments

The effect of the electrode spacing on arc transit velocity was investigated experimentally. An investigation of the effect of electrode spacing on total force delivered by the arc was done by Choi et al. [66]. In the experiment discussed here, electrode spacings of 2, 5, 8.8, and 13.2 mm were tested with peak current kept at a constant value of ~ 850 A by adding resistance to the circuit. Results are presented in Figure 3.5.

Previous results found that the velocity of a gliding arc is primarily dictated by the applied magnetic field independent of the arc current [42]. Since the applied magnetic field for the larger electrode gaps will be smaller for most of the arc, this leads to a lower arc transit velocity despite the increased total force calculated above. The average body force on the arc decreases with gap distance.

While velocity increases for decreasing gap distance there is also a significant change in the character of the dynamic behavior of the arc as it transits. For narrower electrode spacing, the arc moves more smoothly, with fewer anchorings on the anode. This will be discussed in more detail in Chapters 4 and 5.

Chapter 4

Photometry and Muzzle Arc Simulations

4.1 Introduction

This chapter is divided into two parts. The first part discusses experimental characterizations of the internal structure of the RailPAc arc made through high speed video photometry coupled with data on the electrical characteristics of the arc. Dynamics of the arcs internal structure are then correlated with global behavior of the arc, such as transit velocity and repeatability. The second part of the chapter focuses on computational analysis of the RailPAc arc using a thermal (equilibrium) arc plasma simulation tool [67]. The chapter concludes by proposing mechanisms for the observed phenomena discussed in Part 1, based on computational results in Part 2.

4.2 Experiment

Two experimental setups were employed in the studies presented here. The first is a conventional RailPAc shown in Figure 4.2a. Two copper electrodes, each 15.24 cm long, are flush mounted onto a machinable ceramic surface such that two-thirds of their length is embedded in the ceramic, while a third extends beyond the ceramic with only an air gap between them. This

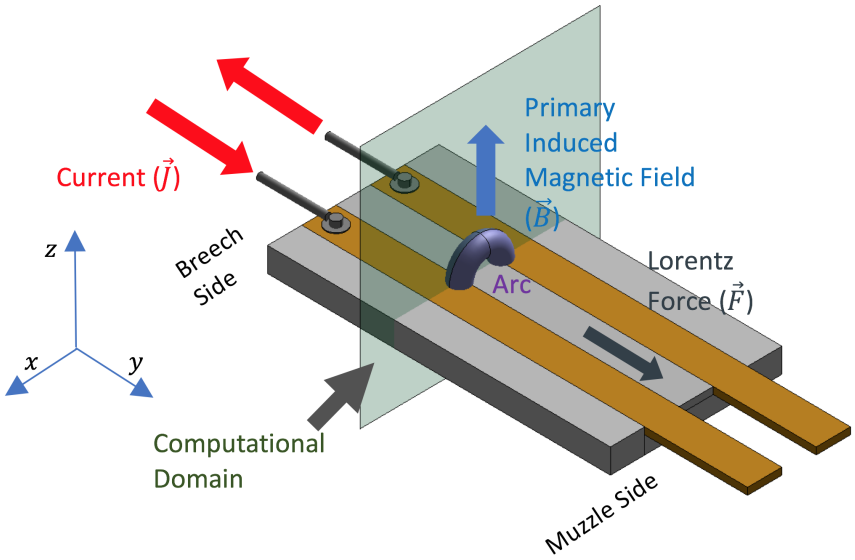

Figure 4.1: Schematic of RailPAc. The computational domain plane used for simulations in this work is indicated in green.

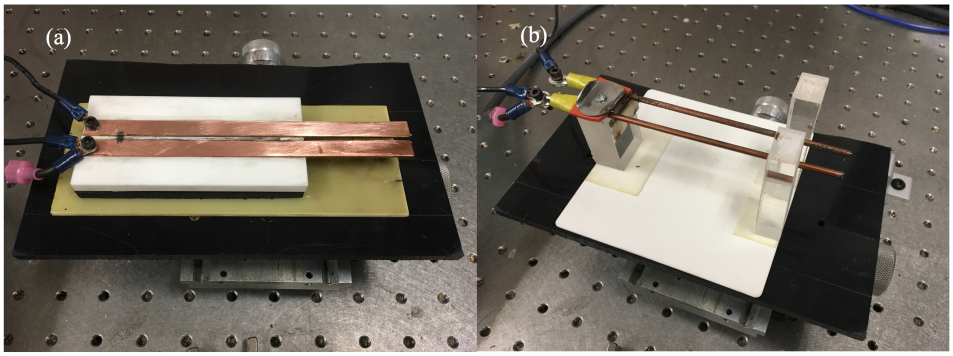

Figure 4.2: The two RailPAc setups. The setup in (a) is the flush mounted variety, while (b) shows the free-floating rod electrode variety.

portion with the air gap allows the arc to come to a stop and quench without damaging the ceramic surface. In a production actuator, the pulse forming network would include components to quickly shut off the current when the arc ceases forward movement. A thin trail of graphite is applied to the surface between the rails as part of the arc ignition mechanism. The anode rail is connected to a pulse forming network as shown in Figure 4.3, while the cathode rail is connected to ground through a diode. The cathode rail is also connected to a high voltage source which can bring the cathode rail to -15 kV for ~ 10 μs. This brief but large voltage change pulls a small surface-tracking arc across the graphite trail, creating a conduction pathway to ground for the larger capacitor bank in the pulse forming network. The connection to the larger capacitor bank rapidly increases the arc current and dimensions.

The second experimental setup follows the same principle as the traditional RailPAc, but uses free-floating copper rods as electrodes. This simplified geometry is free of complicated arc-surface interaction and can be used to determine actuation performance of a simple free burning arc [61]. It is presented here to compare expected behavior differences between the free-floating geometry and the flush mounted geometry. The rods have a length of 11.2 cm and a circular cross section with a diameter of 2 mm. The setup for the free-floating rods case is shown in Figure 4.2b. The pulse forming network which powers both RailPAc setups consists of a 21 mF capacitor bank in series with a 60 μH inductor and a diode with a reverse breakdown voltage greater than the -15 kV initiation pulse delivered to the cathode rail. A schematic for the pulse

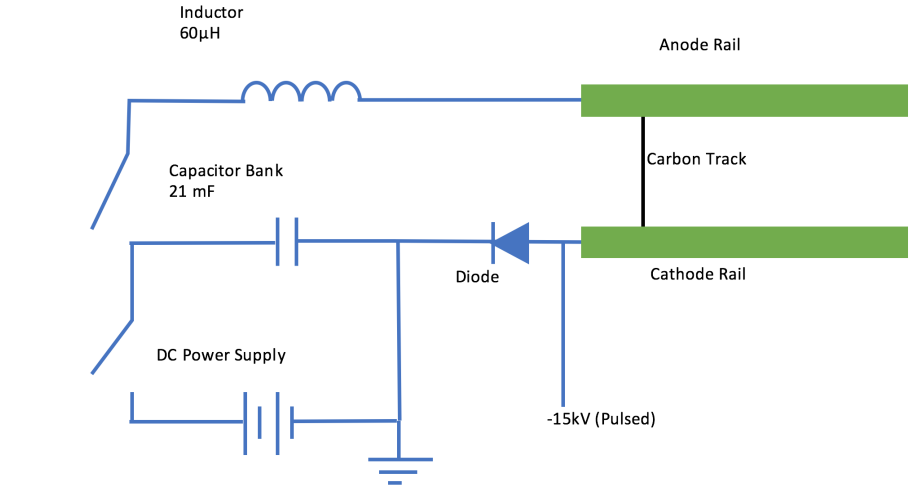

Figure 4.3: Circuit Diagram for the RailPAc with high voltage surface tracking arc trigger system.

forming network is shown in Figure 4.3.

High speed imaging data was collected using a Phantom Miro M-310 camera with a series of first surface optical mirrors which allow for a single camera to look at an event through two independent beam paths, as outlined in Figure 4.4. This allows one or both beam paths to be independently filtered. By using narrow-bandpass filters around specific spectral lines, the spatio-temporal distribution of different species within the arc can be observed. For all imaging in this article, a bandpass filter centered at 520 nm was used to capture copper emission while a bandpass filter centered at 780 nm was used to capture oxygen emission. Both filters are specified by the manufacturer to have a Gaussian transmission profile with a 10 nm bandwidth. Based on the

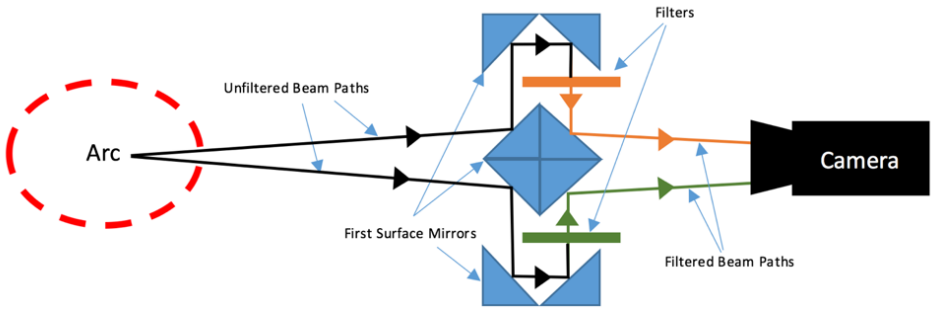

Figure 4.4: Setup for independent filtering.

spectra gathered on the RailPAc arc [38], this should preclude emission from any other species. It is assumed that the presence of oxygen also indicates a proportional level of other air products (nitrogen, argon, etc.). Tests running the arc in an atmospheric pressure tank filled with argon were run and returned little to no signal when run through the 780 nm filter while still returning a strong copper signal in the 520 nm filter. Similarly, tests with tungsten rod electrodes in air give no signal using the 520 nm filter but a strong signal with the 780 nm filter.

4.2.1 Experimental Results

4.2.1.1 Free-Floating Rods

For the free-floating rods, the arc composition appears dominated by air, showing only a low signature of copper eroded from the rods. Previous results suggest that oxygen and copper are thermalized with one another so large variations in copper emission intensity in the absence of a corresponding jump in oxygen intensity should indicate an increase in number density of cop-

per relative to oxygen [38]. At initiation, only the roots are visible as in Figure 4.5a, however the column quickly expands and increases to an approximately constant brightness and size as in Figure 4.5b. As can be seen in Figure 4.5c and Figure 4.5f, the arc transit is occasionally characterized by significant increase in the intensity of copper emission corresponding to a copper erosion at those times. Copper erosion can occur on either the cathode side or the anode side, but appears on the cathode side more frequently. This is in line with previous studies of root movement which suggest that cold electrodes, such as copper (which have melting points lower than the temperature required for significant thermionic emission), must rely on continuous evaporation of the thin oxide layer on their surface to produce charge carriers [24, 30]. Both arc roots move smoothly in the free-floating case. The roots also occasionally develop horn-like structures as in Figure 4.5c where a small amount of plasma protrudes in the direction of motion. It is not clear if these horns constitute anode and cathode jets or something else, since they generate no visible flow. However, it appears likely they are weak jets generated by the expected high Lorentz forcing generated by the high current density attachment site of the arc coupling with the peak magnetic field immediately outside of the electrode surface. Similar horn-like structures are also observed in other studies on gliding arcs [33].

The arc column in the free-floating case is non-diffuse, and moves with a periodic left/right oscillation as it moves down the electrodes. This is visible in Figure 4.5, which shows the bulk of the column moving back and forth

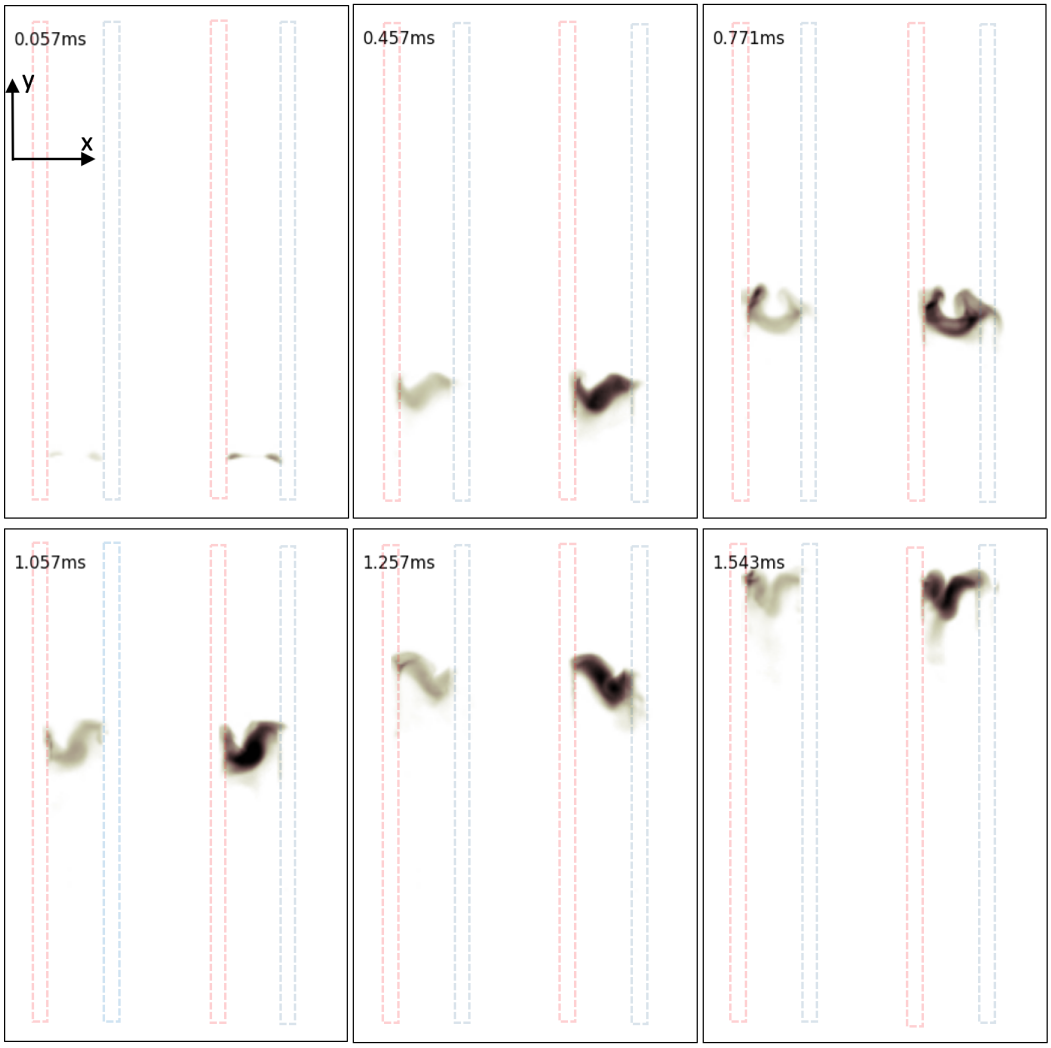

Figure 4.5: Neutral copper and oxygen emission for free-floating rods RailPAc with 12.5 mm rail spacing. The left side shows the copper emission while the right shows the oxygen emission. The cathode is outlined in red while the anode is outlined in blue. The images are in chronological order, and time-stamps in the upper left of each image indicate how long after initiation of the arc the image was taken.

between electrodes. The period for these oscillations is ∼0.25 ms. These oscillations appear to be due to the slight offset of the roots causing the column to run at an angle between them. The offset makes the magnetic field at the downstream root higher due to the tighter curvature of the current path. This higher magnetic field raises the Lorentz force so that the root is pushed further forward enhancing the disparity in field strength while also pushing the column near the downstream root towards the opposite electrode. When the column is pushed all the way across the interelectrode gap, a plasma stagnation layer forms on the opposite electrode pushing the root on that side ahead of the previously downstream root. The process then repeats with the root positions reversed. The jet negating effect of the plasma column on the electrode, as described by Sanders et al., is very noticeable in this process because whenever the column is pushed away from the surface of the electrode, the root constricts and forms a weak jet directed towards the opposite electrode, as shown in Figure 4.5e and Figure 4.5f.

4.2.1.2 12.5 mm Electrode Spacing Flush Mounted RailPAc

The geometry of the arc with 12.5 mm electrode spacing in a flush mounted RailPAc configuration was previously examined [38], however, photometric analysis is repeated here to contrast with the smaller electrode spacing cases. For electrode spacings wider than 5 mm, the arc column begins close to the surface of the RailPAc as in Figure 4.6a and 4.9b. During this time, the arc roots move along with each other. The arc soon rises due to Lorentz

forcing as in Figures 4.6c and 11d. Buoyancy is believed to be a negligible effect in the arc's rise. This can be demonstrated numerically by comparing the relative strength of the buoyant force per unit volume which should be approximately $F_{buoyant} = \rho_{ambient}\ g$ where $\rho_{ambient}$ is the ambient air density and g is the acceleration due to gravity. The strength of the Lorentz force per unit volume is $F_{Lorentz} = |\vec{J} \times \vec{B}|$. For the RailPAc arc, $F_{Lorentz}$ should be nearly 5 orders of magnitude larger than the buoyant force.

At some point, usually after the first restrike, the column becomes far more diffuse than the jets. Copper ceases to permeate the column and the arc roots begin to move independently of one another as in Figure 4.6e and 4.6f. Strong jets are visible at all times, with copper displacing oxygen near the electrode surfaces. The anode jets in the wider electrode spacing cases are often more powerful than the cathode jets and blow the column higher on one side than the other as shown in Figure 4.6e and 4.6f. The jets may also blow the column further out to the sides of the rails if they are directed outward as on the cathode side of Figure 4.6e and 4.6f. Usually one or more of the jets points slightly (or very far) forward in the direction of movement, because the Lorentz force acting on the root is directed this way. The roots also do not always attach on the inner edge of the electrodes as they do in the 2 mm and 5 mm cases. At some point in the transit, the cathode and anode roots both may move across the surface of the electrodes to the outer edges of the electrode. The cathode root does this smoothly, leaving a track across the surface of the electrode, while the anode root may jump to the outer edge.

This movement occurs more frequently for the cathode root than the anode root.

4.2.1.3 5 mm Electrode Spacing Flush Mounted RailPAc

In the 5 mm flush mounted rail case, the arcs anode root can move in one of two ways. The anode root may move in a series of small jumps while the cathode root moves smoothly. This anode root jump behavior was previously analyzed in detail for a rail spacing of 12.5 mm [61], and appears to be the case for any spacing larger than 5 mm. This behavior of anode root jumping is well known and has been observed in gliding arcs across many operating conditions [52, 68]. Unlike the 12.5 mm case, the 5 mm case also has periods where the anode root moves smoothly alongside the cathode root, similarly to the free floating-rod electrode geometry described above. This movement is punctuated by occasional restrikes of the arc, where a new arc forms behind the current arc. The resulting diversion of arc current into the new arc extinguishes or reduces the transit velocity of the original arc until the new arc merges with the original arc. Images from the video of the 5 mm case are shown in Figure 4.7.

The pilot arc for the 5 mm spacing case is shown igniting in Figure 4.7a. Initially only oxygen emission is visible in the arc, however, by 0.1 ms, copper jets at the anode and cathode form and inject copper into the arc structure. Significant copper emission is present at the cathode for the remainder of the arcs lifetime. The anode jet forms and dissipates as the anode root jumps and

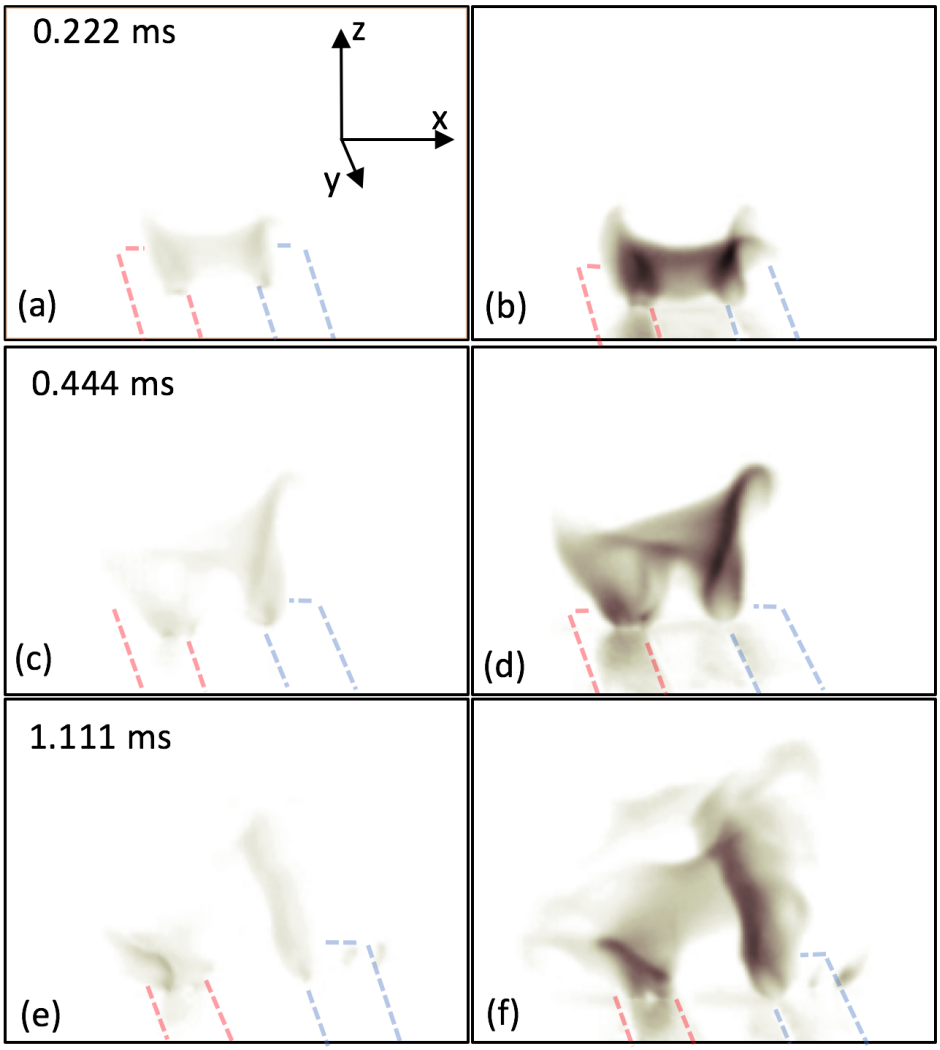

Figure 4.6: Copper and oxygen emission, looking down the muzzle of the RailPAc at a shallow angle for electrode spacing of 12.5 mm. The anode is outlined in blue while the cathode is outlined in red. Note that the copper electrodes are reflective so the electrodes appear bright in (b), (d), and (f). The images are in chronological order from top to bottom, so the evolution of the arc is visible as it expands upwards and develops a diffuse, copper-poor column.

reforms. If the anode moves smoothly, there is minimal copper emission at the cathode as seen in Figure 4.7d. If the anode anchors for a particularly long period of time, as shown in Figure 4.7b, the copper jet on the anode enlarges and displaces oxygen/air from the interior of the arc. A restrike is shown in Figure 4.7d where a second arc temporarily forms behind the original arc before they coalesce and the arc reverts to the smooth, fast moving state it was in before the restrike. Near the end of the transit, around 2 ms, the roots begin to move independently of one another with the anode root slightly leading the cathode root before small restrikes return it to a position immediately adjacent to the cathode root.

Once can determine the shape of the arc in more detail by observing the RailPAc from the muzzle side facing towards the breech so that the arc is propagating directly towards the viewer as it moves down the rails. For the 5 mm electrode spacing case, the arc consistently and repeatably assumes the shape shown in Figure 4.8. An anode and cathode jet extending from the field enhancement spots at the corners of each electrode are both clearly visible. Tracking the movement of small persistent flow features and illuminated particulate through the jets using high speed imaging make it clear that they are generating flow velocities $\sim$100 m/s. The column rests in between the jets and extends from 1-2 mm to 2 cm above the RailPAc surface. There is a noticeable void at the base of both jets in the oxygen emission, which corresponds to a brighter portion in the copper emission. This void implies that the copper evaporating into the arc is displacing the oxygen before mixing at a location in

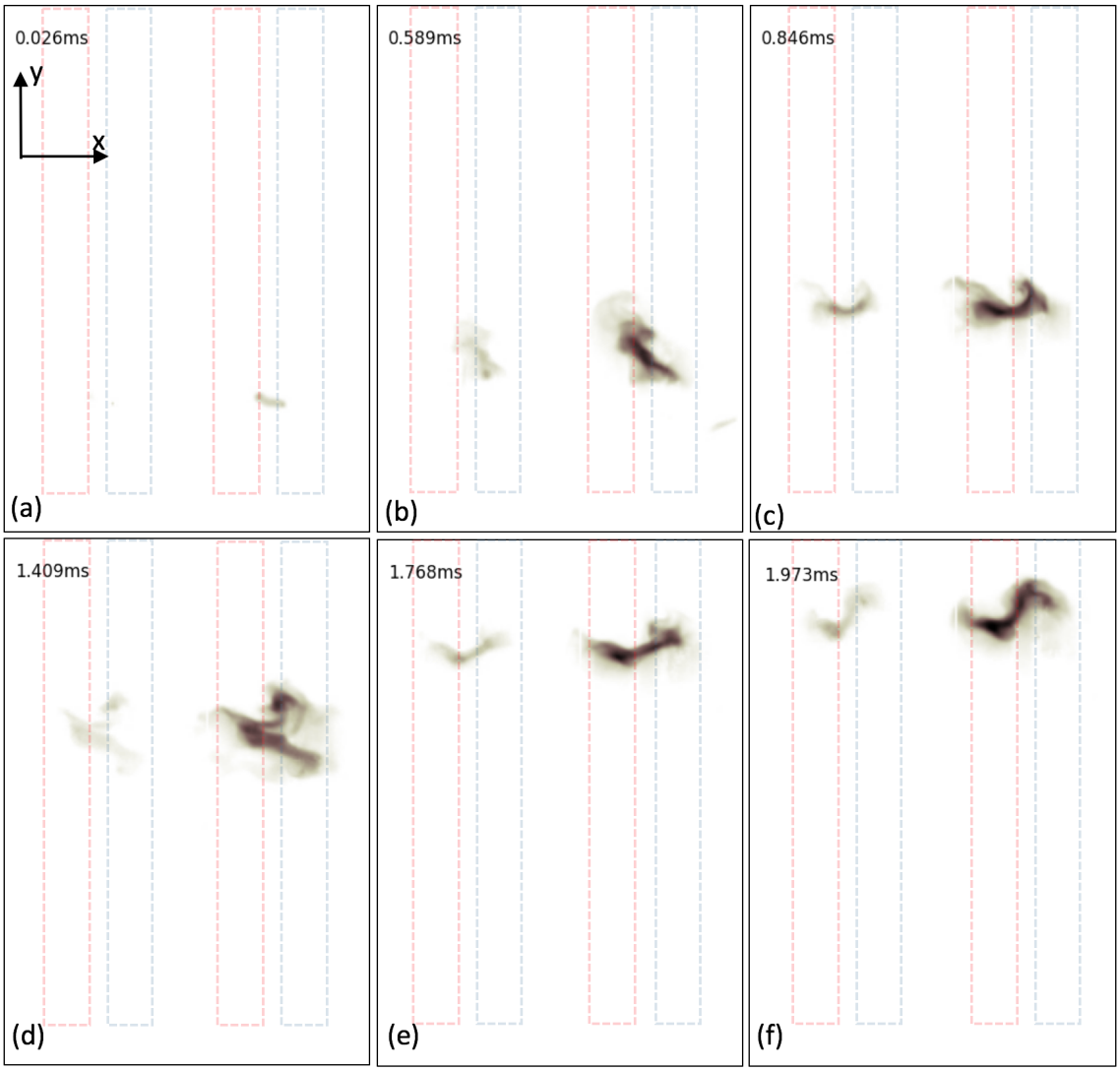

Figure 4.7: Neutral copper and oxygen emission for RailPAc with 5 mm rail spacing. The left side shows the copper emission while the right shows the oxygen emission. The cathode is outlined in red while the anode is outlined in blue. The images are in chronological order and time-stamps in the upper left of each image indicate how long after initiation of the arc the image was taken.

the jet high above the surface. While oxygen emission seems to dominate the column region of the arc, there is also significant copper emission, especially near the axial center of the column.

While the flow of the jets in the 5 mm case shown in Figure 4.8 is mostly laminar in appearance with only occasional turbulence, the flow of the plasma around the root jets in the 2 mm case is often more chaotic but it is unclear how much of this is due to rapid changes in the direction of the jet and how much is due to turbulence. Calculating Reynolds numbers for the jet suggest values of Re$\sim$1000 given ambient viscosity, arc gas density of 1×10^{-2}kg/m^3, length scale of 0.01 m, and a representative velocity of 100 m/s. Literature suggests this turbulence is largely confined to the shear layer on the outside of the jet with the plasma extinguishing at the jet tip due to rapid turbulent mixing of surrounding cold air [69, 70]. This suggests that estimates of the jet velocity by tracking of eddy structures gives a lower bound for the velocity of the laminar core of the jet.

4.2.1.4 2 mm Electrode Spacing Flush Mounted RailPAc

The 2 mm spacing flush mounted case shows considerably different behavior from the 5 mm spacing case. Still images from high-speed video can be seen in Figure 4.7. With 2 mm rail spacing, the arc is more coherent, with both roots moving at the same rate throughout the entire transit. The 2 mm case, like the 5 mm case, forms a pilot arc at initiation which is initially composed solely of air products with no copper emission. At 0.026 ms, the

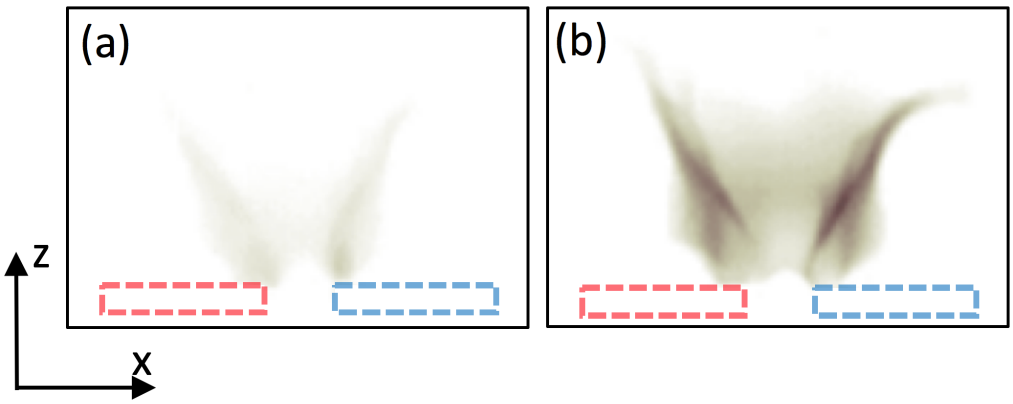

Figure 4.8: Muzzle view of the arc for 5 mm electrode spacing. The oxygen emission is on the right while the copper emission is on the left. The cross section of the anode is outlined in red and the cross section of the cathode is outlined in blue.

copper begins to emit at small spots on the cathode and anode. The arc then moves smoothly along the rail. The copper is always clearly filling out a smaller portion of the arc than the oxygen, which extends out further from the center of the arc than the copper and reaches a height comparable to the 5 mm case.

The one major disruption in the transit of the RailPAc arc for the 2 mm spacing occurs around 0.6 ms into the transit, just after the peak current as measured by a Pearson probe using the same method as in chapter 2. The arc suddenly widens, with both roots taking on a more extended contact with the edge of the rails. A small spike of plasma also appears in the direction of motion which can be clearly seen in Figures 4.10d, 4.10e, and 4.10f. It should be noted that while this spike of plasma appears to be in different

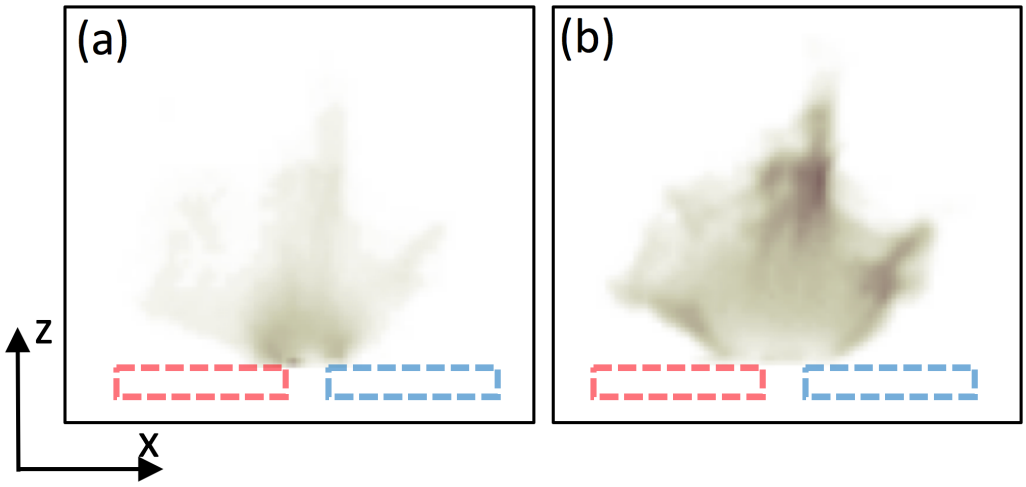

Figure 4.9: Muzzle view of the arc for 2 mm electrode spacing. The oxygen emission is on the right while the copper emission is on the left. The cross section of the anode is outlined in red and the cross section of the cathode is outlined in blue.

places relative to the electrodes in the oxygen and copper emission, this is just an artifact of the data collection system caused by parallax, and the spikes are present at the same physical location in both emissions.

The increased copper density towards the center of the arc for the 2 mm case is particularly obvious when looking down the rails in the y-direction as defined by Figure 4.1. Figure 4.9 shows still images from high speed video looking down the rails for the 2 mm case. Here we see a region of high copper density at the shortest path between the electrodes, where the highest current density is expected. The outer regions of the arc contain a diffuse level of copper but very high oxygen emission. In contrast to the pair of jets seen in the 5 mm spacing case, there is now a bright central spike and two arms extending out to either side which seem to consist of predominantly air products based on the oxygen emission. Occasionally, the region also fills with copper. The central spike has a visible flow pattern in high speed video data with significant upward velocity similar to jets seen in other cases, however, in this case there seems to be a separation of the copper and oxygen, where copper remains at the base of the jet while oxygen dominates the top of the jet. This shape consistently appears at this electrode spacing, though occasionally the tall central spike splits into two slightly smaller spikes.

The small spike of plasma seen after 0.6 ms in Figure 4.10 seems to be the tip of the spike of oxygen-rich plasma shown in Figure 4.9. The velocity of the arc can be determined by tracking the location of peak brightness in the column with respect to time. It appears that after reaching the maximum

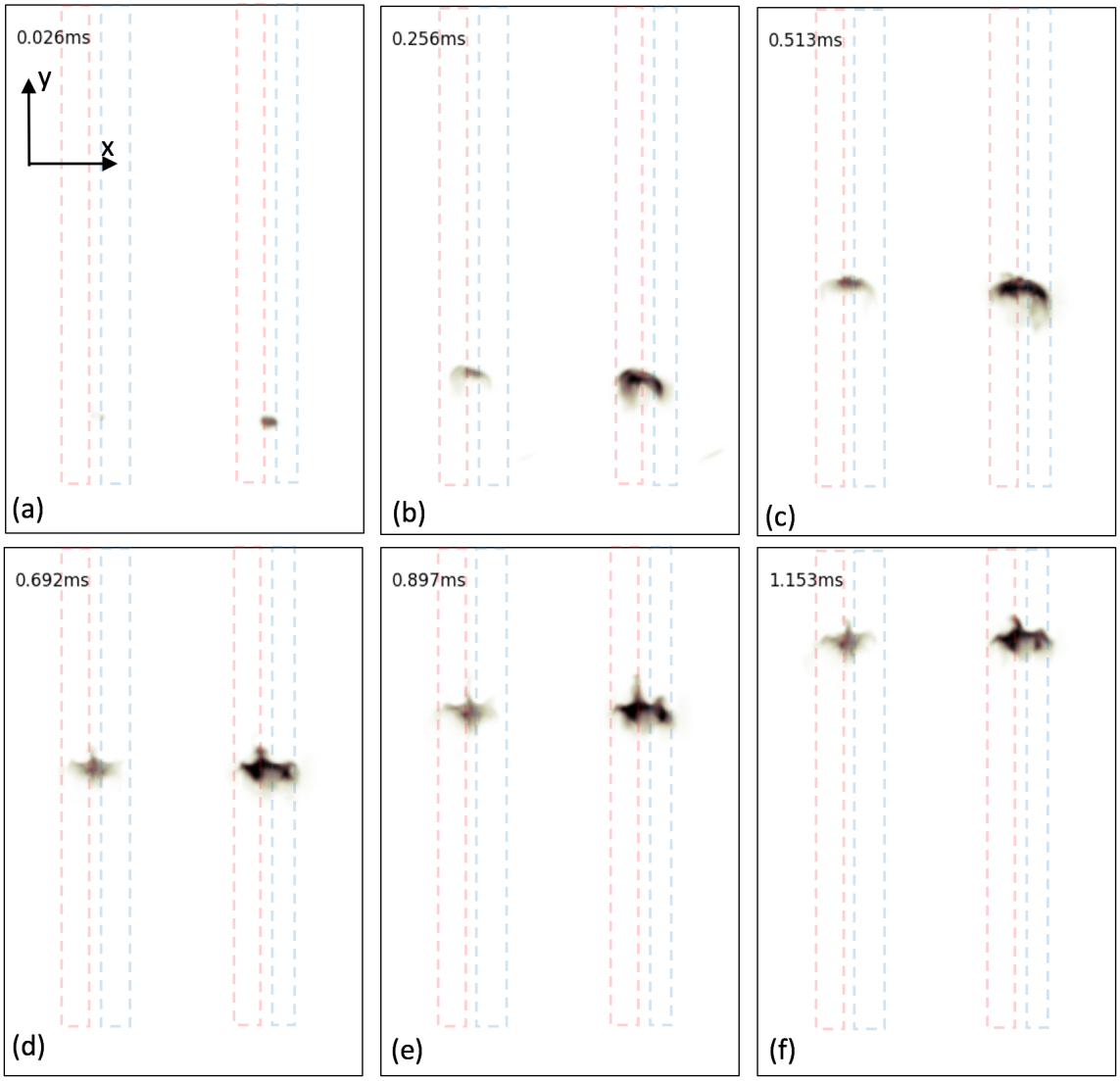

Figure 4.10: Neutral copper and oxygen emission for RailPAc with 2 mm rail spacing. The left side shows the copper emission while the right shows the oxygen emission. The cathode is outlined in red while the anode is outlined in blue. The images are in chronological order and time-stamps in the upper left of each image indicate how long after initiation of the arc the image was taken.

transit velocity just after the peak current, as described in Chapter 2, the induced flow behind the arc begins to push the arc forward with the momentum delivered to it by the now decelerating arc.

Before moving into simulation results, some conclusions can be made based solely on the experimental results above. The arc is clearly anode dominated for the 2 mm spacing. The jet from the anode competes with the cathode jet and prevents a stagnation layer forming at the anode surface. The free-floating rod case is similarly anode dominated with the anode and cathode jets alternately negating one another by forcing the column to the electrode surfaces. The 5 mm and 12.5 mm electrode spacing cases are more difficult to define. Anode jets form in both cases but do not directly compete with one another to form stagnation layers. However, in examining transit characteristics of the arcs, one finds the anode root in all of these cases ultimately dictates the dynamics of the arc, either allowing the arc to move smoothly by traveling continuously along the surface as in the 2 mm and 5 mm cases, or anchoring and jumping as in the 12.5 mm case. This requires a slight expansion of the definition of the term anode dominated to include dynamic behavior of root travel but it would seem appropriate to label these as anode dominated arcs. Copper is eroded from electrode surfaces and enters the arc at the base of the roots where it is injected into the arc by the flow generated in the arc root jet. This copper will remain in the column unless the arc has a restrike, in which case it leaves. Arcs which do not restrike maintain their copper content. Copper is eroded at a high enough rate to visibly displace oxygen at the base

of roots. Examining the dynamics of the arc transit, stable configurations of the arc where the column stays close to the actuator surface are promoted by closer spaced rails with either partially merged or full merged root jets. These stable configurations have fast, smooth moving anode roots which maintain similar velocities to the cathode roots. More closely spaced electrodes result in more stable arcs. Experiments do not reveal the mechanism by which these stable configurations form nor can they confirm the mechanism by which the root jets form. Both of these will be examined computationally in the next section.

4.3 Simulation

Numerous computational studies have been performed on thermal arcs in general and magnetically driven arcs in particular [45, 71, 72]. Here we perform two-dimensional simulations of RailPAc experiments discussed above using the VizSpark thermal/arc plasma simulation tool [67]. The plasma is assumed to be quasineutral and in a state of thermal and chemical equilibrium. While details of the governing equations and the solution approach are available elsewhere, we describe the approach briefly as follows. Governing equations for mass continuity, momentum conservation, and energy conservation (assuming a single temperature plasma) are solved. The momentum equation includes the term for Lorentz forcing of the plasma resulting from magnetic fields and the energy equation includes Joule heating from electrostatic fields. The equations are coupled to a current continuity equation for

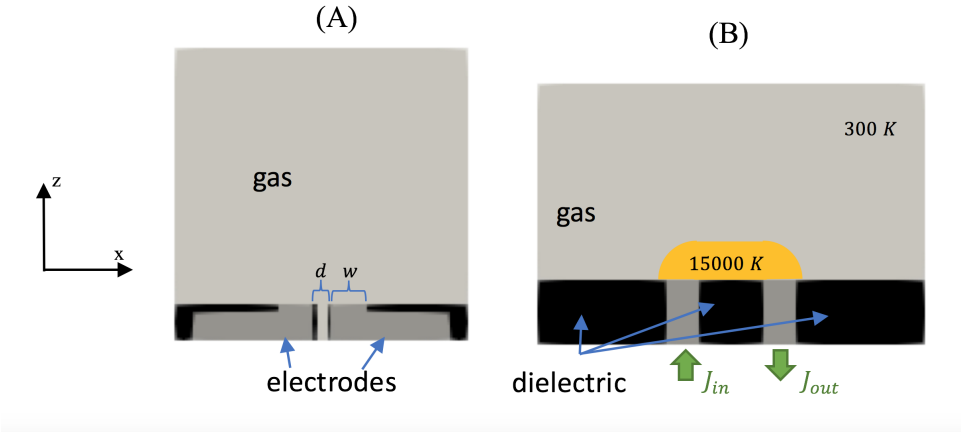

Figure 4.11: Schematic of the computational domain for different representations of the arc. The electrodes are shown in dark gray, the dielectric in black, and the gas in light gray. The shape of the temperature kernel used to initiate the arc is shown in yellow in Geometry (B). The electrode width, w, and rail spacing, d, are indicated in Geometry (A).

description of the electrostatic (ambipolar) electric field and another equation for the self-induced magnetic field resulting from electrical current density in the plasma. Thermodynamic properties of the plasma, such as mass density and enthalpy, are precomputed as a function of the pressure and temperature assuming thermal and chemical equilibrium. The plasma composition is similarly available as a lookup table as a function of temperature and pressure. The transport properties of viscosity, thermal conductivity, and electrical conductivity are also precomputed and tabulated.

While the RailPAc arc is clearly a complex three-dimensional phenomena, we simplify our studies in this chapter to a two-dimensional computational description that resolves arc phenomena in a plane perpendicular to the length

of the rails (see Figure 4.1). This assumption therefore allows for a description of arc structure resulting from forces and transport processes in the solution plane but necessarily ignores the dynamics and structure of the arc along of the length of the rails. Despite this simplification, several experimental observations of the arc structure described earlier can be modeled.

Schematics of the computational domain for different representations of the arc are shown in Figure 4.11. Two electrodes each of width w=2 mm and separated by a distance d (from 1 mm to 10 mm) are embedded in a dielectric material. A uniform input current boundary condition is specified at the base of one of the electrodes while the other is fixed at a ground potential or set to an equal and opposite current boundary condition to maintain symmetry in the arc. This is the simplest two-dimensional model for the current input, which would come in from the front or back of the simulation domain in the actual RailPAc. For domains without the central dielectric like Geometry A, an outflow condition was specified at the boundary to simulate the 3D pressure relief which would be present in the real arc. All other gas boundaries were set as outflow boundaries. The metal electrodes are thermally insulated by setting their conductivity to values $\sim 10^{-8}$ W·m^{-1}·K^{-1}, however heat loss from the gas to the dielectric is allowed to prevent the arc from unrealistically stabilizing at the surface of the dielectric. In the simulations, the arc is initialized between the electrodes using a high temperature kernel of 15,000 K as shown in Figure 4.11(b). This kernel creates a conductive path which current can pass through when the simulation begins. Subsequently, the arc evolution is modeled in a

time-accurate fashion.

4.3.1 Computational Results

4.3.1.1 Arc Root Jets

The most prominent features observed in the RailPAc arc are the anode and cathode jets formed at the attachment site of the arc roots on each electrode. As mentioned earlier the presence of one or more of these jets is a common feature of high intensity arcs and has been observed to play a large role in the dynamics of the RailPAc arc [24, 38]. As discussed above the arc root jets exist as either independent jets, partially merged jets, or fully merged jets, and the state of the jets is strongly dependent on the spacing of the electrodes. Wider electrodes favor independent jets and closer spaced electrodes favor partially or fully merged jets. Two dimensional simulations using geometry B from Figure 4.11 show minimal dependence of jet formation on electrode spacing, however structures similar to the independent, partially merged, and fully merged jets shown respectively in Figure 4.6a, 4.8b, and 4.9b are observable at different points in the evolution of the arc. Figure 4.12 shows simulation results for electrode spacing of 4mm at three different time-shots with Geometry B.

Computational results presented in Figure 4.12 suggest that the primary mechanism for jet formation is direct Lorentz forcing at the base of the roots (indicated in Figure 4.12d) as opposed to magnetically pumped jets found in other high intensity arcs [23, 24]. While this has only been shown

to be true in two dimensions with the simulations presented here, it may be inferred to also be true in three dimensions since the strength of magnetic pumping for a given average current density is expected to be more dramatic in two dimensions than three dimensions. The strength of magnetic pumping is dictated by the rise of pressure at the center of the arc due to magnetic pinching. This pressure can be estimated by assuming a steady state so that,

$$\vec{\nabla} P = \vec{J} \times \vec{B}. \tag{4.1}$$

If equation 4.3.1.1 is integrated for the same current density and arc radius in two and three dimensions it can be shown that the central pressure for the two dimensional case is a factor of $\pi^2/2$ larger than the three dimensional case.

The localization of the Lorentz forcing which leads to jet formation is caused by the strong field enhancement and corresponding high current densities at the arc root attachment sites at the corners of the electrodes. Since the magnetic field is strongest near sharp turns in the current path, the $\vec{J} \times \vec{B}$ forces near the electrode corner is extremely high. This localized increase in forcing causes the appearance of jets.

As the arc forces itself away from the surface of the RailPAc, the jets production sites move from the electrode corners into the column, and eventually merge into a single jet as in Figure 4.12k. The simulation results indicate

that this may in fact be due to the change in the location of peak forcing from the corners of the electrodes to the high curvature region of the column as it lifts up from the surface, shown in Figure 4.12h. This high curvature in the arc induces a strong magnetic field that accentuates the vertical motion of the arc and, if the curvature is sharp, a high current density region similar to the one near the electrodes is formed. This process is analogous to kink instability formation in tokamak plasmas [73]. Jet velocities were found to reach as high as 500 m/s for the non-pressure relieved geometry with higher velocities for merged jets than independent jets. This compares well with observed velocities in magnetically pumped root jets despite the apparent difference in formation mechanism [21, 23].

Velocity predictions in these simulations may over-predict actual velocities. Smaller grid sizes can make velocity predictions as much as 20% lower. This variation is due to the confinement of the majority of field enhancement to the grid cells immediately outside the electrodes. For smaller grid sizes, the physics of this enhancement are less smeared out and result in slightly higher heating but lower momentum addition. Ideally, this smaller grid size would be used to obtain more accurate quantitative information, however, the computational cost of using such a smaller grid makes running these simulations untenable with available equipment. Simulations of 1 ms physical time took up to 5400 hours for finer grids on 4 cores. With additional time and a more capable machine it would be possible to make more accurate simulations and is a target for future work. We feel that while the velocity predictions of these

models are only quantitatively accurate with an error of ∼20% at the field enhancement sites, the predictions still serve as an excellent analysis tool to identify the mechanisms by which experimentally observed phenomena occur. A mesh convergence study was performed to evaluate the degree of inaccuracy. The results are shown in the Appendix.

As discussed previously, the arc plasma jets are expected to consist of a laminar core with a turbulent outer region. This presents a problem for modeling with VizSpark which doesn't include a turbulence model in its calculations. Since jet height is dictated by turbulent mixing rates [69], the solutions presented here likely overestimate both jet height and jet velocity since cooling of the jet would be increased by the presence of turbulence. This matches what we see in simulations where the jet height is only limited by diffusive cooling and run time.

4.3.1.2 Wall-Stabilization of the Arc

The arc column is expected to move as a single fluid packet in a so-called snow-plow mode [42]. In two dimensions, this means that the arc acts as a piston so that as it is forced upwards, away from the surface of the RailPAc, a low-pressure region is formed below the arc and a high-pressure region is formed above as in Figure 4.13. The low-pressure results in an inward motion of the left and right parts of the arc column, forming a sharp kink at the top of the column. The kink is characterized by high current density that leads to a high Joule heating region at the tip, and a high temperature of ∼25000

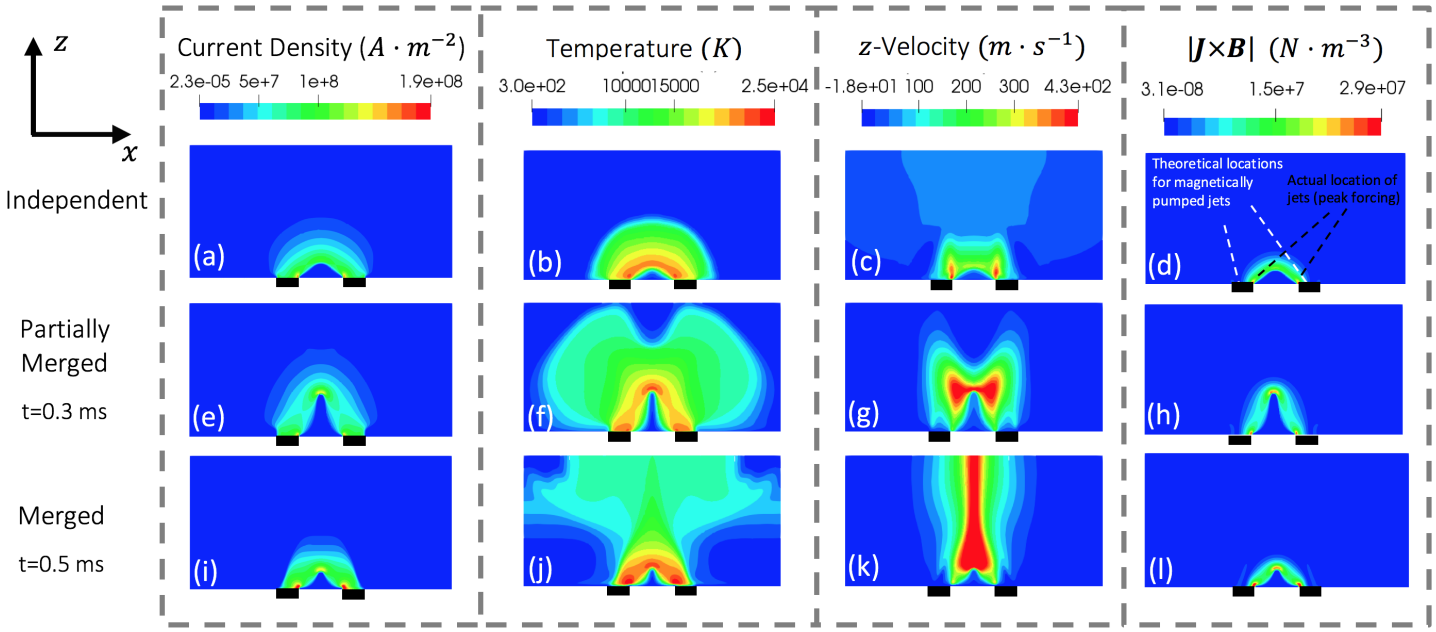

Figure 4.12: Evolution of current density, temperature, vertical (y) velocity, and in plane Lorentz forcing for interelectrode spacing of 4 mm with Geometry B. Electrode locations are indicated by black bars. Temperature distributions are expected to correlate roughly with observed light intensity in experiments. Larger versions of this figure are available in the Appendix.

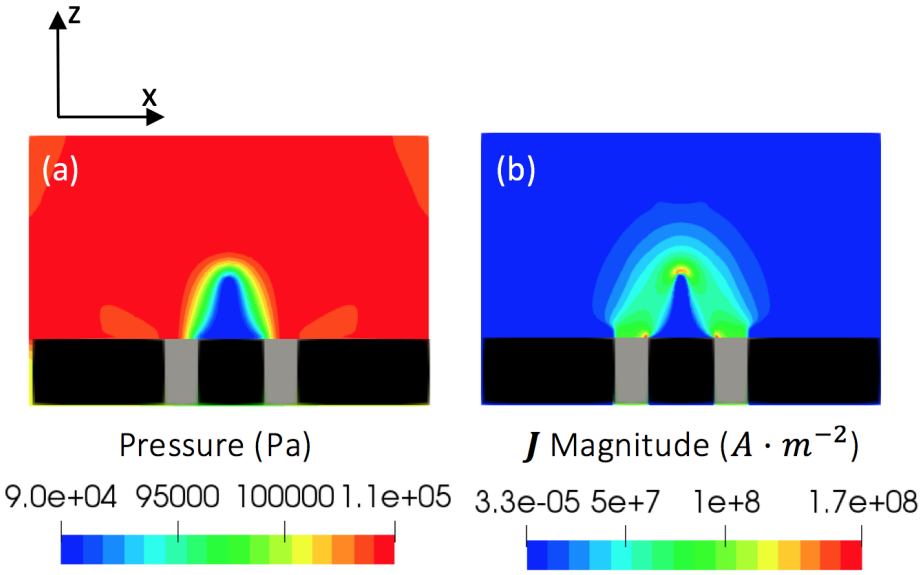

Figure 4.13: Low pressure region created below the arc column. Pressure distributions are shown in (a) while current density magnitude is shown in (b).

K compared to average temperature of around ∼13000 K in the rest of the column. This heats the air below the arc, causing the arc to move diffusively as a deflagration back towards the surface where it eventually stabilizes as in Figure 4.12i.

Two possible wall-stabilizing mechanisms are thus identified. The low-pressure region pulls the column downwards, and strong curvature in the arc column leads to the arc moving diffusively towards the wall. The pressure effect is expected to be considerably weaker in three dimensions due to the pressure relief in the direction along the length of the rails. However, when the diameter of the arc begins to approach the length of the arc, such as the more narrowly spaced electrodes in Figure 4.10, pressure effects are expected to dominate, strongly stabilizing the arc at the RailPAc surface, as observed in experiments with closer electrodes. Similarly, close electrode spacing should cause the curvature of the arc to increase more rapidly with column height above the surface increasing the arcs ability to move diffusively towards the RailPAc surface.

If pressure relief is allowed by setting the boundary between the electrodes to a constant pressure outflow using Geometry A, the Joule heating effects discussed above can be seen in more detail, as in Figure 4.14. When the electrodes are closely spaced, as they are in Geometry A, a high electric field is generated in the x-direction between the two arc roots. Since this region is also hot enough to be conductive due to diffuse heating, there is a small current density in the same region. This causes high Joule heating

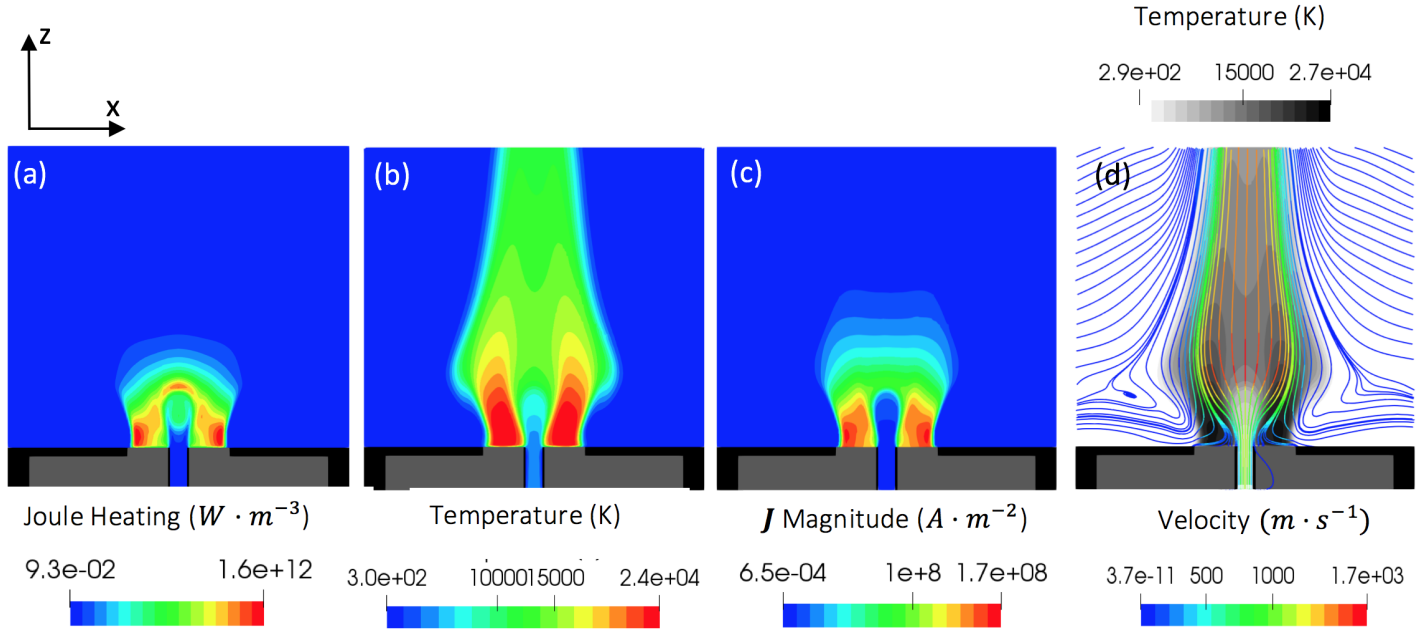

Figure 4.14: Wall-stabilization by high Joule heating for 1 mm spaced electrodes using Geometry A from Figure 4.11. Joule heating is shown in (a), temperature distribution is shown in (b), and the magnitude of the current density is shown in (c). Streamlines are imposed on the temperature distribution in (d). Dielectric is indicated in black while electrodes are dark gray.

$(J \cdot E)$ which rapidly raises the temperature of the incoming gas, allowing it to flow directly through the current carrying portion of the arc and enter the merged arc root jet. If the magnitude of the Joule heating is right, and the gas entering through the pressure relief boundary is significantly heated ($\sim$4000 K), the arc will stabilize at some point above the wall as seen in the computational results in Figure 4.14 and experimental data shown in Figure 4.8b. Notably, in the geometry shown in Figure 4.14, the jet is also able to reach much higher velocities ($\sim$1600 m/s) than the non-pressure-relieved case. This is large compared to other estimates of arc jet velocities but still of the same order of magnitude. This stabilization above the wall with minimal pressure effects is believed to be the mechanism by which the arc stabilizes in the 5 mm cases shown in Figure 4.8.

The streamlines in Figure 4.14d show that the arc is not perfectly impermeable. Streamlines enter into the arc from the outside into the base of the electrodes and from the pressure relief boundary up and into the arc. Both entry locations correspond to high Joule heating regions. For cold gas to enter the temperature gradient also must be very steep to diffusively heat the cold gas to a point of significant conductivity so that Joule heating can bring the gas up to arc temperature. This is an extremely important insight into the physics of arc permeability. As discussed in more detail in Chapter 7, high intensity arcs are largely impermeable but not perfectly so. High heating sites near the edges of the arc allow for cool gas outside of the arc to enter into the arc. Note also that while gas has trouble entering the arc, exiting the

arc is simpler. If we define the arc by the current carrying region in Figure 4.14c we see that while the streamlines enter only in certain places, there is no identifiable requirements for the exit of those streamlines from the current carrying portion of the arc.

The final wall-stabilization mechanism identified is related to the dependence of the magnetic field on the electrode geometry. If the electrodes are constructed such that a larger portion of integrated current, I, is forced to travel in the x-direction through the electrodes, the magnetic field induced near the surface of the RailPAc between the electrodes, tends to push the arc downward towards the surface. This effect is shown in Figure 4.15 where the magnitude of the $\vec{J} \times \vec{B}$ force is plotted for simulations using variants of Geometry A. The stable case on the left side of Figure 4.15 has a portion of dielectric along the bottom of each electrode so that current only enters and exits from the outer regions of the electrodes forcing a different current path through the electrode from the unstable case on the right.

A line of zero net force traverses the length of the current path, with current-carrying portions of the domain on either side of this line being pinched inwards toward the line. In the stable case, the portion of the arc being forced downward is greater than the portion being forced upwards. This results in an arc with a net force directed downwards, which stabilizes the arc at the wall. In the unstable situation on the right side of Figure 4.15, the opposite is true, resulting in an arc which has a net force upward thereby preventing stabilization at the wall. In the real world, this effect is expected to scale

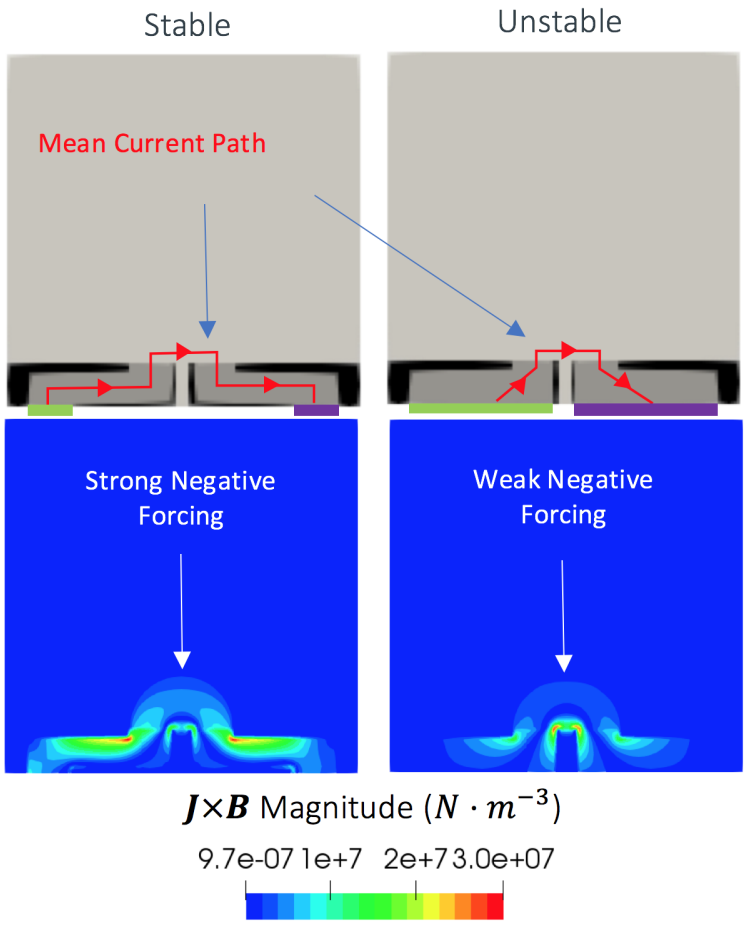

Figure 4.15: Electromagnetic stabilization of the arc due to electrode geometry. Electrode spacing is 1 mm. The images on the left correspond to a stabilizing electrode geometry and the images on the right to an unstable electrode geometry. Current input is indicated in green, while output is indicated in purple. The line of zero force through the arc is indicated by a dashed orange line in both cases. All forcing will be directed towards this line, so current carrying portions of the arc above the line will push downwards while portions below the line will push upwards.

with the width of electrodes since the current density in the electrodes will be largely constant until very near the attachment site of the arc. The existence of this effect implies that thin electrodes with a width comparable to the diameter of the arc root will likely impair actuator performance by preventing wall stabilization, however this has yet to be confirmed experimentally.

4.3.2 Restrike

Restrike is the phenomena where an additional arc is formed electrically parallel to the primary arc. This phenomenon is well-characterized in the RailPAc arc and is a common feature for all gliding arcs [30, 48]. For the RailPAc, the second arcs formation is almost always associated with the immediate quenching of the original arc. This results in the arc appearing to jump from place to place rather than moving smoothly over the surface of the electrodes. Restrike usually appears to occur in a stepwise process. First, a small restrike filament is formed at a new attachment site on one or both electrodes. This restrike filament then increases in brightness and forms a new arc while the old arc quenches. Experimental observations limit the timescale over which this occurs to $\sim$50 μs. Experimental observations of the transition from restrike filament to fully formed arc column are shown in Figure 4.16.

Restrike processes similar to those seen in experiments are also observed in simulations. Computational results are shown in Figure 4.17. The process occurs over timescale of a few microseconds and is primarily driven by Joule heating of the gas between the arc roots. As the arc rises, the constant

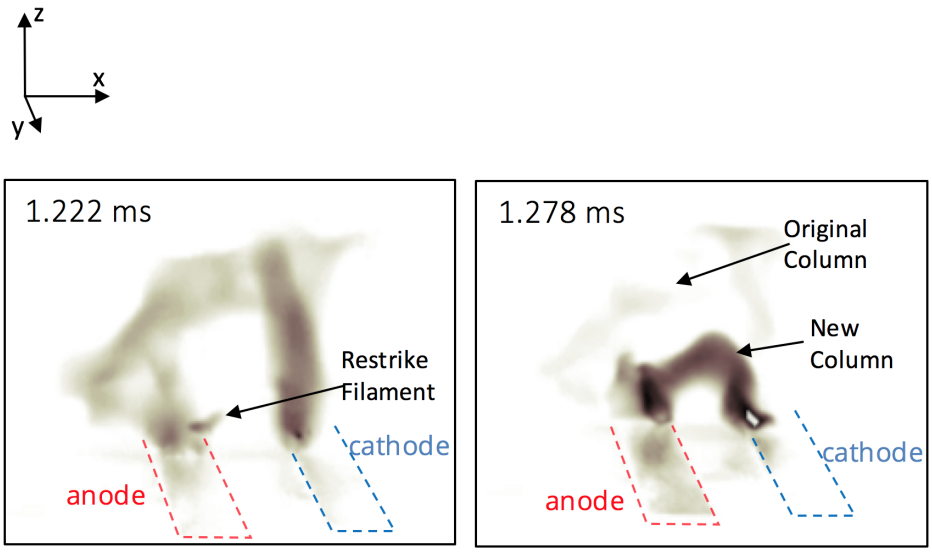

Figure 4.16: Experimental observation of the restrike process. Electrode spacing is 12 mm.

current requirement at the boundary forces the potential drop across the arc to increase. The electric field in the x-direction between the roots increases as the arc rises away from the surface, which means that Joule heating also rises anywhere that the gas is conductive enough to pass current. This results in localized regions well below the main column which are heated to a point where the conductivity is of the same order as the main column forming a restrike filament as in Figure 4.17 at t=602 μs. Eventually, the current path through the restrike filament is preferable to the main column and the restrike filament rapidly increases in conductivity, becoming the new main column while the old column quenches as shown in Figure 4.17 as t=603 μs.

Notably, the restrike filament rises significantly faster than the loan

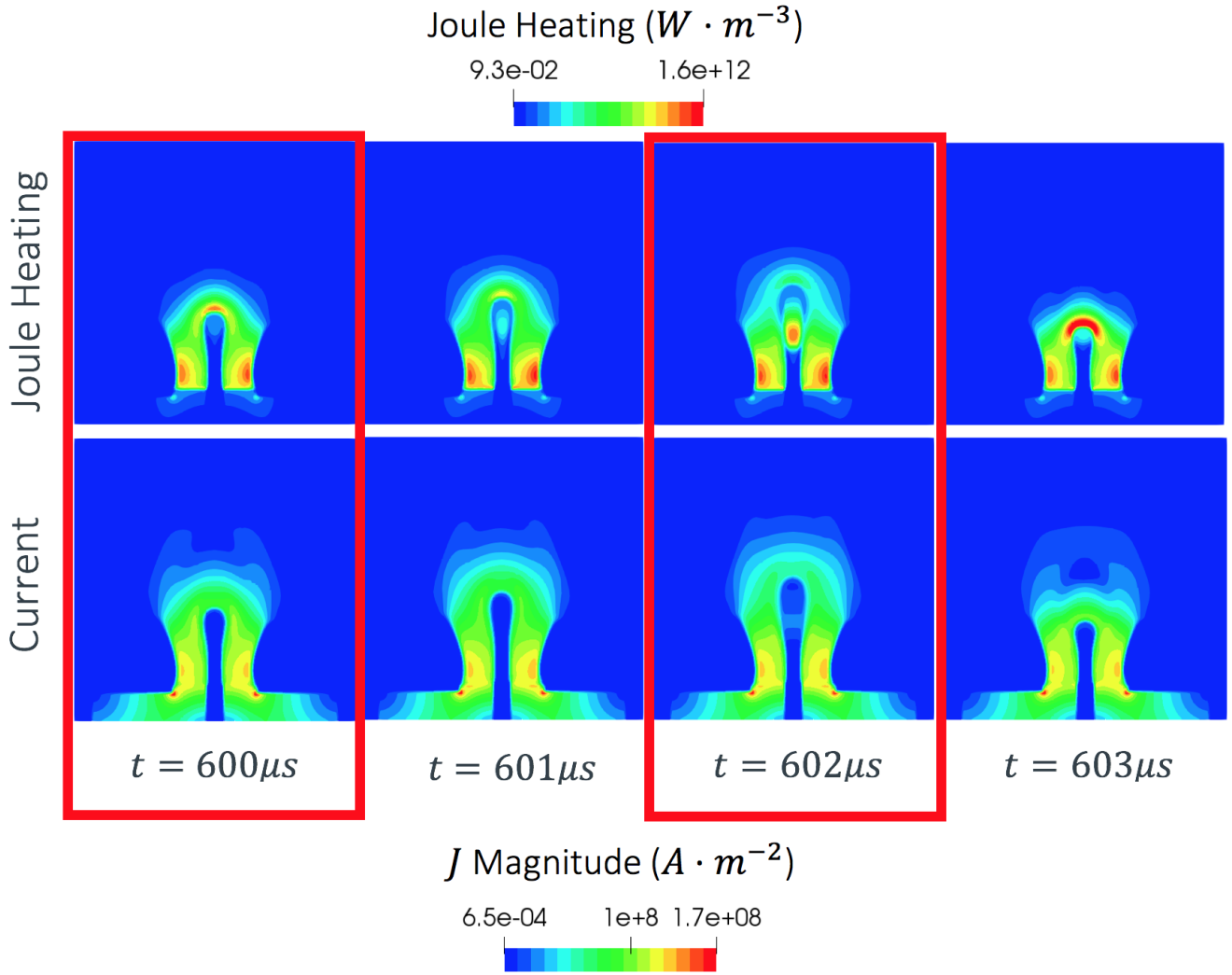

Figure 4.17: Computational observation of the restrike process in arc simulation using domain with Geometry A.

column because the filament and column are attracted to one another just as current-carrying wires would be. This attraction results in a rapid rise in the restrike filament as it becomes the main column and sends a transient impulse of momentum upwards on each restrike. These transient momentum additions may significantly affect the actuators efficacy when it operates in the restrike mode.

4.4 Reynold Number Analysis

VisSpark does not include a turbulence model. Literature suggests that turbulence is important in root jets only at the tip of the jet where cold air is brought in from the outside of the jet through turbulent mixing, quenching the plasma and shortening the length of the jet [69, 70]. Turbulence is generated in the shearing layer starting at the base of the jet and grows with distance away from the jet base. The center of the jet maintains a laminar core until the strongly mixed jet tip. Reynolds numbers are expected to vary from around 10 at the laminar base of the jet to 10000 at the turbulent tip of the jet [69]. This is very close to what we find for our simulations. Figure 4.18 shows the local Reynolds number for the pressure relieved case where velocities (and thus Reynolds numbers) are highest. Reynolds numbers noticeably increase further up the jet. Reynolds numbers in simulations never reach above $\sim$1000. This is encouraging for the viability of VizSpark for reaching physical solutions to the muzzle arc problem.

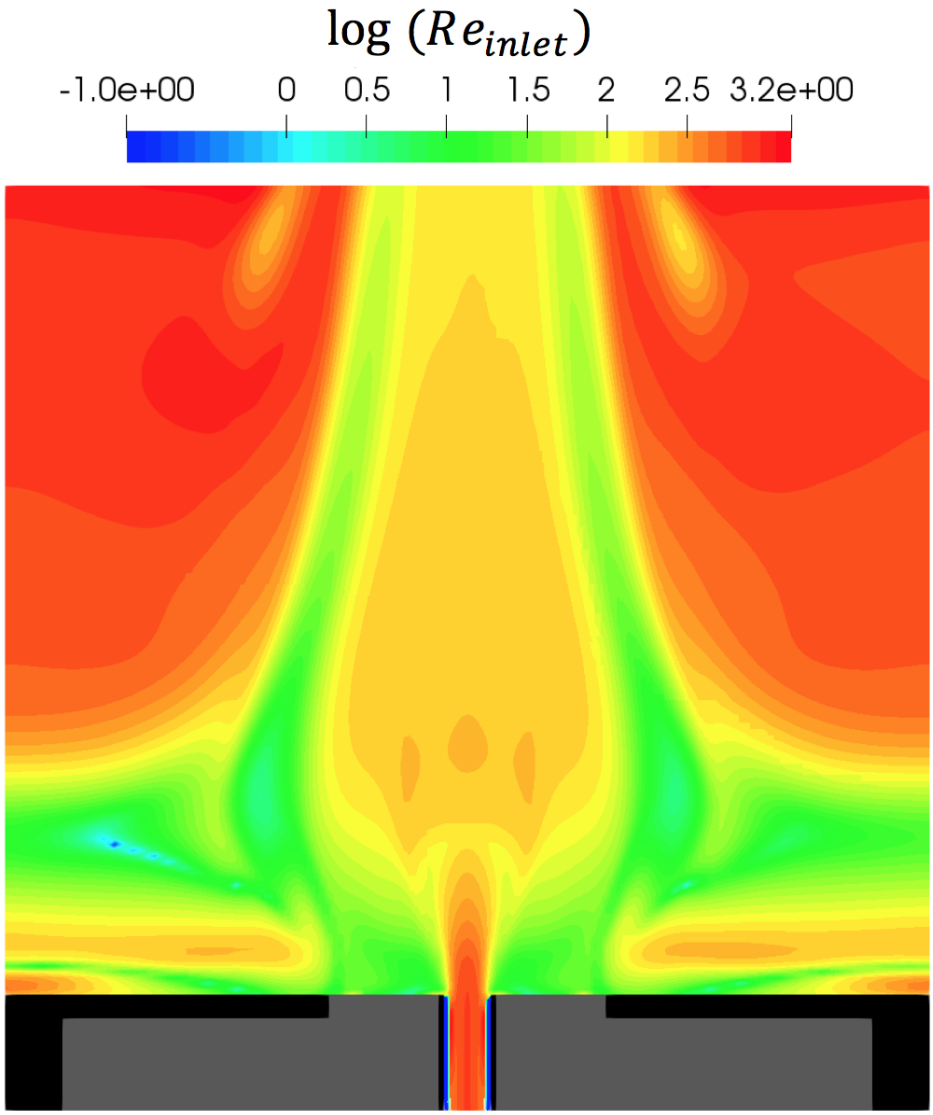

Figure 4.18: Local Reynolds number using a length-scale dictated by the inlet width.

4.5 Discussions

In aerodynamic analysis of high current gliding arcs, it is common to assume that the arc moves as a solid body with no convective transport in or out of the arc [42]. However, it is possible that fluid could flow through the arc by ionizing at the leading edge of the arc and then neutralizing at the trailing edge. This behavior is called a plasma deflagration mode, in contrast to a snowplow mode where the arc moves as a single fluid packet pushing the surrounding fluid out of the way. Arc motion in the deflagration mode significantly lowers the ability of the arc to transfer momentum to the surrounding air. The ability for current to pass through a fluid volume is dictated by the local conductivity σ of that fluid. The electrical conductivity is predominantly a function of temperature ($\sigma = \sigma(T)$) so the variation of σ in the flow will be dictated by the transport of temperature within the flow. The relationship,

$$\frac{DT}{dt} = \alpha \frac{\partial^2 T}{\partial x^2} \tag{4.2}$$

describes the behavior along a streamline running through the center of the arc along its direction of motion, allowing us to quantify how much of the apparent arc velocity is due to diffusion. The equation is solved in one dimension for several initial temperature distributions. Values for the thermal diffusivity of the gas as a function of temperature and pressure are obtained

from VizSpark [67].

Thermal diffusivity is a weak function of pressure, however, to simplify results, the one dimensional domain is assumed to remain at a constant pressure of 100 kPa. Simulation results shown above suggest this is a reasonable assumption since pressure rarely changes by more than 10% in the two-dimensional simulations. Air begins to be significantly electrically conductive between 3000 K and 6000 K. It is thus assumed that any gas reaching 4000 K will begin to carry current. If the point in the solution where T=4000 K is tracked across several timesteps, a diffusion velocity can be estimated. This velocity should correspond to the maximum rate at which fluid can pass through a steady state arc in a fully developed flow. Several initial sinusoidal temperature profiles are shown in Figure 4.19a with temperature distributions given by,

$$T = \begin{cases} T_{ambient} & for\ r > R \\ T_{ambient} + \frac{T_{max} - T_{ambient}}{2} \left(1 + cos\left(\frac{\pi r}{R}\right)\right) & for\ r < R \end{cases} \tag{4.3}$$

where T_{max} is the peak temperature, $T_{ambient}$ is the ambient gas temperature, and R is the width of the temperature kernel assumed to roughly correlate with arc radius. Ambient gas with a starting temperature of 300 K is compared to preheated ambient gas starting at 3000 K with peak temperatures of 10000, 15000, and 20000 K.

For non-preheated gas at 300 K, the peak velocities of the moving temperature front are ∼5 m/s with most velocities < 1 m/s. Even with very steep temperature gradients and gas preheated to 3000 K, the velocity of cold gas entering into the arc will be of order ∼10 m/s. Both of these numbers are obtained with spacing between the peak temperature value and the ambient gas of less than 1 mm. Observed velocities of the arc in experiments are ∼50 m/s, which suggests that the only time 10% or more of the arcs motion can be ascribed to deflagration movement is when the ambient gas is significantly preheated due to radiative or Joule heating and when the arc has a temperature distribution which produces steep temperature gradients near the outside of the arc.

This suggests that the degree to which the arc moves in a snowplow mode or in a deflagration mode can be estimated by looking at the temperature profile at the edge of the arc. The arc will move diffusively in the steep temperature profiles near kinks in the plasma column. In contrast, the areas in the main column of the arc away from sharp turns in the current where the temperature gradient is shallower would be expected to move in a snowplow mode. This explains why the outer portion of the arc in the simulations shown in Figure 4.12, which had relatively low temperature and current density, moved in a snowplow mode, while the wall side parts of the arc, where the current density and temperature gradients were high, moved diffusively. This has significant implications for actuation purposes and suggests that the most efficient means of actuation is to somehow limit the ability of the arc

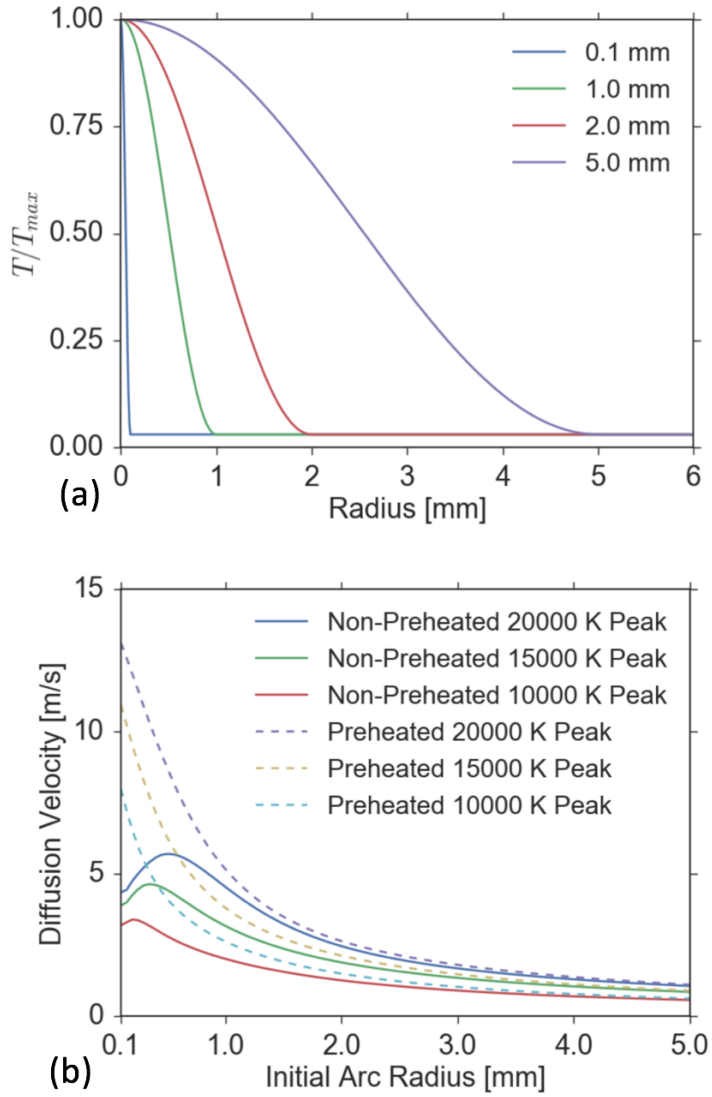

Figure 4.19: Initial sinusoidal temperature distribution for one dimensional simulations are shown in (a) while results for the diffusion velocity of the temperature wave front for each distribution are shown in (b).

to produce regions of high Joule heating while maintaining high Lorentz forcing. This could be achieved by lowering the integrated current into the device while commensurately increasing magnetic field, either by looping the input wires below the RailPAc to form a solenoidal field or by applying some other external field.

Chapter 5

Effect of Electrode Oxidation States

5.1 Introduction

With the exception of the work by Poeffel and Li-Chun [33, 36], research into the effect of oxide layers and electrode surface damage has primarily focused on the cathode. For conventional arcs with a direct, linear current path between parallel electrodes this makes sense, because the dynamics of high intensity arcs are primarily driven by the cathode [24]. Even attachment modes at the anode are primarily a function of fluid flow due to magnetically pumped jets formed by the cathode [22, 37]. However, previous work on the RailPAc and other gliding arcs has found that the anode can retard the net motion of the arc due to frequent anchoring [30, 38]. This chapter explores the effect of oxide layers on the anode and implications for the global dynamics of the RailPAc arc.

5.2 Experimental Methods

The experiments described here employ the same flush mounted setup used as in Chapter 4. Two copper electrodes, each 15.24 cm long, are flush mounted onto a machinable ceramic surface, such that two-thirds of their

length is embedded in the ceramic while a third extends beyond the ceramic with only an air gap between them as in Figure 4.2a. As in Chapter 4, the behavior of the arc is only examined in the section where the electrodes are flush mounted.

The pulse forming network which powers both RailPAc setups consists of a 21 mF capacitor bank in series with a 60 μH inductor and a diode capable of holding off the -15 kV pulse delivered to the cathode rail. In all cases, the capacitor banks were charged to $\sim$250 V before firing the 2 mm rails and $\sim$275 V for the 5 mm rails to maintain more consistent current levels between the two cases. A schematic for the pulse forming network is shown in Figure 4.3.

As in Chapter 4, Phantom Miro M-310 cameras were used to capture high-speed video with frame rates in the range of $\sim$18-100 kHz. Anode, cathode, and column position were tracked digitally using the OpenCV machine vision package. The tracking results were smoothed with a Savitzky-Gavol filter to highlight largescale trends in the otherwise noisy data. Electrical data was collected using Tektronix 3014B oscilloscopes with Tektronix high voltage probes to measure the voltage drop across the arc and Pearson current monitors to measure the total current of the circuit which should correspond to the arc current.

Uniform oxide layers can be created on copper surfaces by heating the copper surface in the presence of oxygen at atmospheric pressure. Layer depth is a function of time, temperature, and pressure. In this experiment, copper anodes were prepared by mechanically removing their outer surfaces with 120

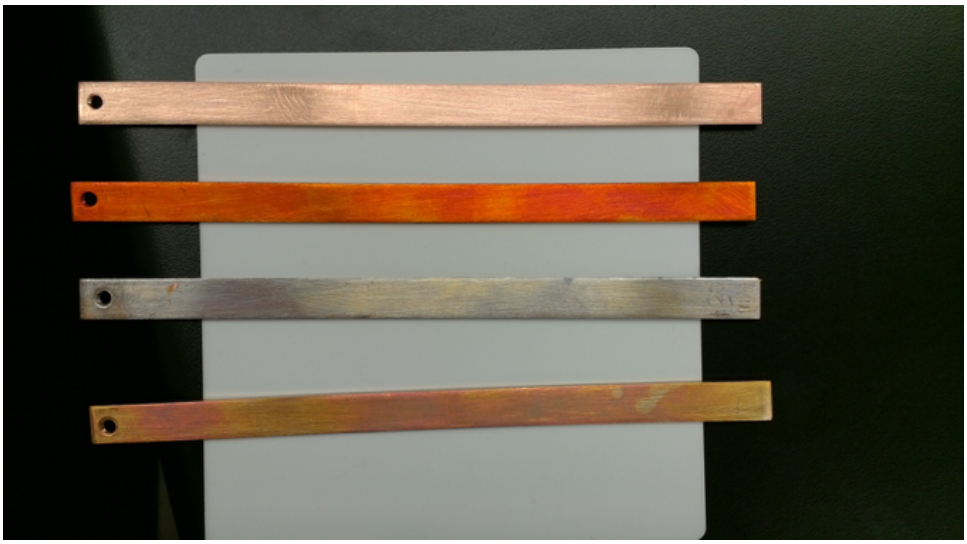

Figure 5.1: Oxidized rail electrodes

grit sandpaper. The anodes were then heated in open air ovens at 200°C for 1, 10, 30, and 120 minutes. Based on the results from Lee et al. [74], oxide layer depths of approximately 150, 200, 300, and 600 nm respectively are expected. Oxidized electrodes are shown in Figure 5.1. One study found that gliding arc cathode root velocity was increased by small abrasions on the electrode surface in the direction of travel, so sanding was done with an orbital pattern to eliminate any preferential direction of sanding abrasion on the surface [75]. Observation of arc behavior was conducted with rail spacings of 2 mm and 5 mm with fully reduced rails, as well the four oxidation levels described above and shown in Figure 5.1.

The oxide layer which naturally forms on copper in air can be removed either by chemically reducing the copper in an acid bath or by mechanically

removing the outer surface through sanding. Experiments were conducted to determine if either method results in a significant change in the arc behavior. No significant change in arc behavior was noted. Similarly, no noticeable effects could be related to mechanical deformation due to arc melting of the surface. Pairs of electrodes were repeatedly fired to damage their surfaces and then reduced in hydrochloric acid solutions. Upon firing the RailPAc with the reduced rails, arc behavior was identical to behavior with freshly sanded rails despite macroscopic topological differences still present on the surface of the rails due to melting. These two points allow for considerable leeway in experimental design with regard to control studies since the initial state of the rails only depends on the chemical state, and not the mechanical state as claimed by Cheng and Zhao [75]. Control studies using electrodes with freshly sanded electrodes were performed on both the 5 mm and 2 mm rail spacings.

5.3 Results 5 mm Rail Spacing

For the 5 mm control case, the arc was found to travel significantly more smoothly than with the 12.7 mm spacing described by Gray et al. [38]. The cathode root moves smoothly, as in wider spacings, and the anode root was observed occasionally anchoring before jumping forward to attach at a site directly across from the cathode root. This is most common on the first shot independent of electrode oxidation level. Unlike the previous observations using wider electrode spacings, the anode root often simply slowed down instead of fully anchoring. Anode jumps with a slow-moving anode instead of

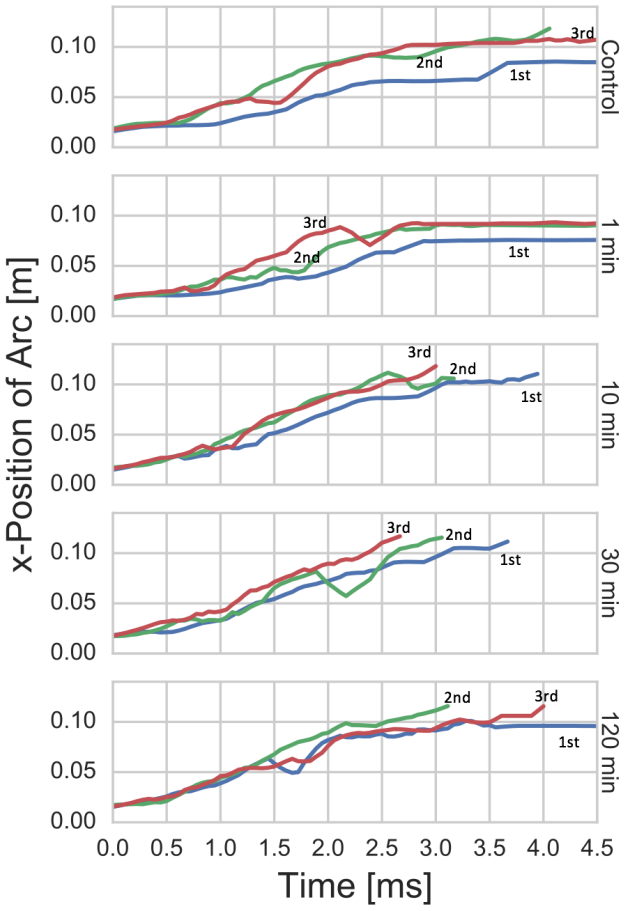

Figure 5.2: Anode position with respect to time for 5 mm rail spacing with variable oxidation.

an anchored anode tended to be smaller around the width of the rail spacing, while jumps with fully anchored anodes often reached 10 mm or more from the anchoring site to the new root site. A brief anchoring on the anode was often observed upon ignition of the arc even in arc-treated rails. There was also significant variation in the arc behavior as the control rails were repeatedly fired. In all cases for fully reduced rails, the first shot has multiple anchorings and restrikes and then, as the rails are repeatedly fired, the passage of the arc becomes smoother. This is similar to behavior described by Poeffel [36] where it was noted that arc-treated rails behaved differently than reduced rails for simple gliding arcs. Oxidizing only the anode and using a fully reduced cathode produced similar results to arc treatment. This is shown in Figure 5.2 where anode location is plotted as a function of time.

Note that as the oxide depth increases, the first shot becomes more like later shots. For the control and 1-minute oxidation case, the first shot on the rails results in an arc with a slower maximum speed, slower average speed ($\sim$20 m/s compared to $\sim$40 m/s for the higher oxidation levels), and higher propensity to restrike. The second shot may then have some of these characteristics, though to a lesser degree, while the arc reaches a steady state by the third shot where the arc moves smoothly and consistently. For higher oxidation depths, this state is reached on the first shot. The origin of this smoother arc motion is the nature of attachment of the anode root. For fully reduced anodes, the root does not move at all, and the arc moves by periodically forming new anode roots in the direction of movement. For deeper

oxide layers, the anode root moves freely over the surface of the anode in a similar fashion to the cathode root. The anode root also occasionally anchors with the 1, 10, and 30-minute oxidation levels, however, it never anchors in the 120-minute oxidation case.

Electrical data showed small but significant changes across oxidation levels. More strongly oxidized anodes resulted in lower resistance arcs and lower arc power on average than the more reduced anodes. Both effects are shown in Figure 5.4. On average, the control has a 16% higher resistance and a 24% higher arc power compared to the 120-minute oxidation. This causes a slight decrease in the current level for the reduced anode arc, which should also result in a quadratic decrease in the force on the arc since $F_{Lorentz} \sim I^2$ when the magnetic field doing the forcing is self-induced. Metal vapor has been found to increase conductivity in gliding arcs, so the more likely source of any changes in arc resistance is physical deformation of the arc either through constriction/expansion of the arc roots or lengthening of the arc column [71].

Damage to the rails is radically different across anode oxidation depths. In the control and 1-minute oxidation cases, the anode root often moves from the inner edge of the anode to outer edge, leaving a dark trail of eroded attachment sites. Anchoring sites are identifiable by significant physical damage due to melting and small black oxidation spots between 0.1 mm and 1.0 mm in diameter. As the oxidation depth increases, the attachment on the anode tends to remain confined to the inner edge of the anode with smaller (and fewer) attachment site damage spots. A similar number of melting sites are found re-

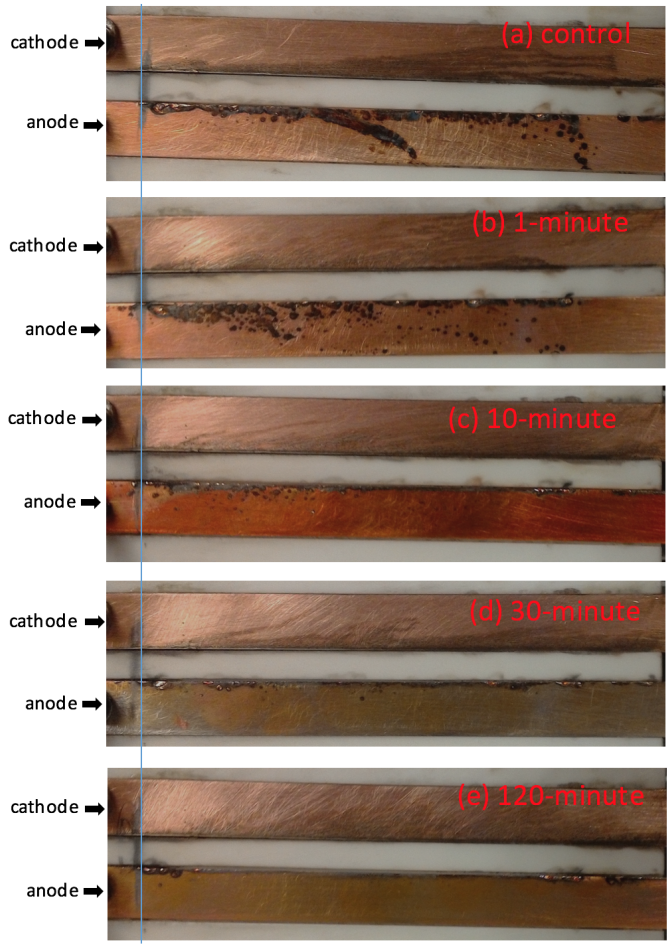

Figure 5.3: Electrode damage for 5 mm rail spacing with variable oxidation. The ignition site is indicated by the blue line on the left.

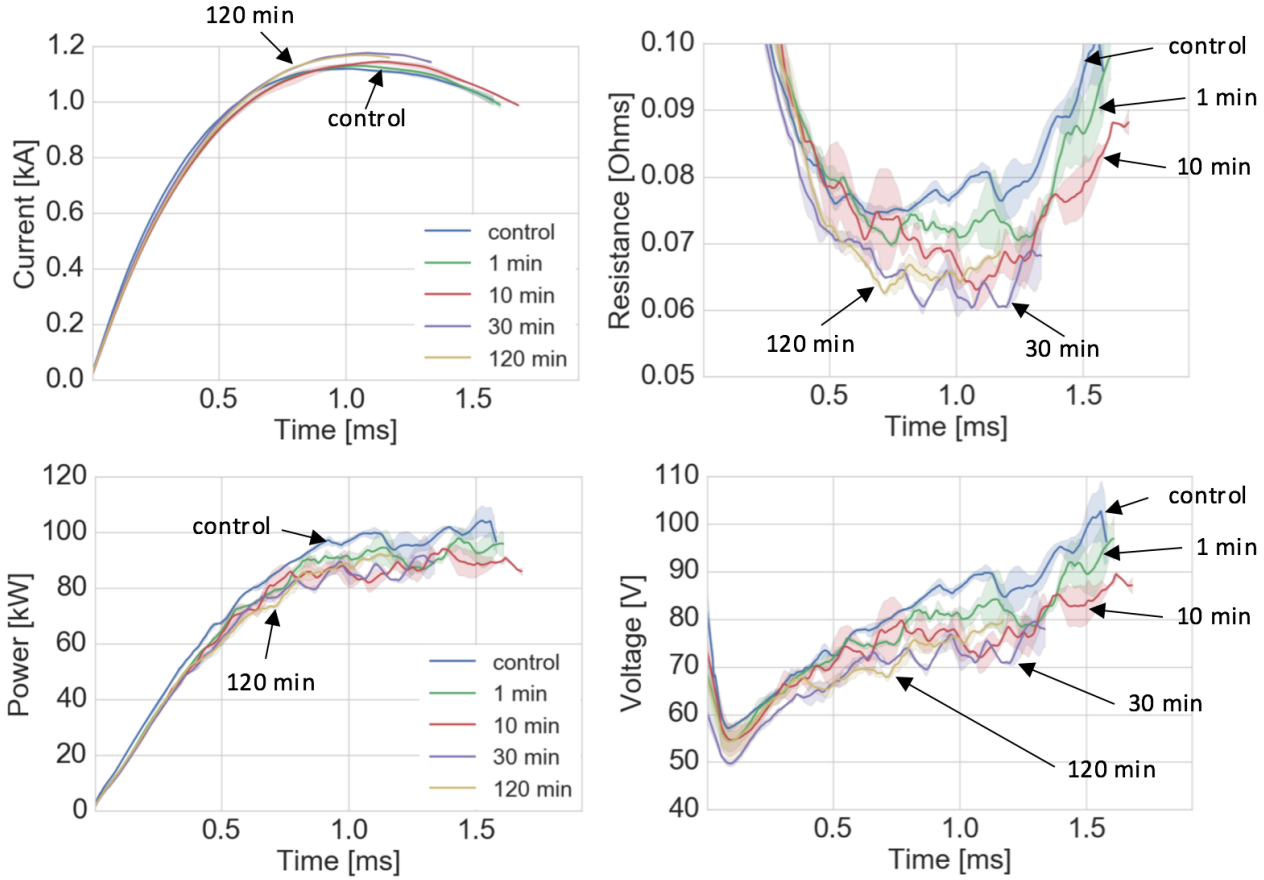

Figure 5.4: Electrical characteristics for oxidized rails with 5 mm rail spacing.

gardless of oxidation depth, however, the severity of melting is decreased with greater oxidation layer depth. Melt sites are noticeably iridescent in color, suggesting thin film optical interference from the presence of a thin oxide layer of variable depth. This iridescence also suggests that the arc is generating its own oxidation layer on the surface of the anode. McBride believed that the arc partially eliminates the oxide layer by electrode heating and then a new layer is formed as the electrode cools [30]. Differences in the behavior of the cathode erosion seem to be insignificant, with faint arc tracks extending from the inner edge to between a third and half of the width of the cathode. The increase in resistance can come from only two sources: deformation of the arc or compositional changes in the arc. The localization of damage to the interior of the electrode suggests that this is the primary point of attachment for the arc roots. This should result in a shorter, and thus less resistive arc.

5.4 Results - 2 mm rail spacing

The narrower 2 mm rail spacing largely follows the same trends found in the 5 mm case. As the rails are fired repeatedly, the arc treatment causes subsequent firings to increase in velocity and smoothness. The arc treatment effects are noticeable at all levels of oxidation in the 2 mm case, with a noticeable change between the first and second firing even at 120 minutes of oxidation. The 2 mm spacing seems to largely prevent anode anchoring noticeable in larger spacings, with the exception of an initial lull in the movement of the arc at ignition. For un-oxidized control rails, the 2 mm rail spacing arc

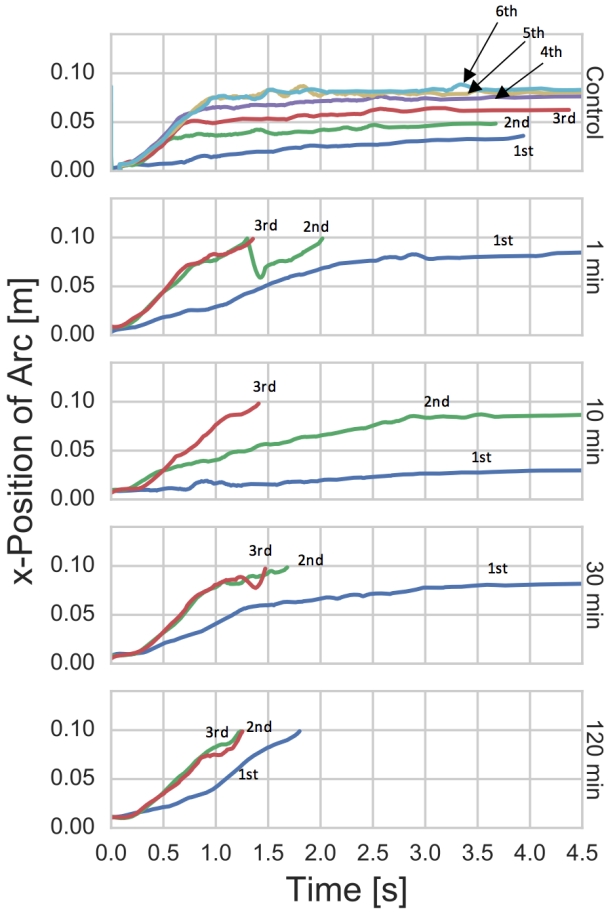

Figure 5.5: Anode position with respect to time for 2 mm rail spacing with variable oxidation. Note that six shots are shown for the control case but only four for each of the oxidized cases because there ceased to be significant shot to shot variability after the first three shots for all but the control case.

demonstrates a burn in effect wherein the arc moves very slowly over any unoxidized surface but quickly over areas the arc has already passed. This results in the unique anode tracks shown in the control case of Figure 5.5. The first shot moves slowly at ∼1-10 m/s for the lifetime of the arc as it traverses the first 5 cm of the rails. The second shot moves quickly at ∼70 m/s for the 5 cm that the first shot covered and then at the slower speed for the latter 2 cm. The third shot moves quickly for 7 cm then slowly over the rest of the rails and all subsequent shots move quickly over the entire length of the rails. This stepwise increase in the length of electrode that the arc traverses is also noticeable in the damage pattern on the control rails, shown in Figure 5.6a.

The different movement modes have significant effects on the physical structure of the arc. When in creeping mode or during the post-ignition anchoring, the arc sweeps forward as in Figure 5.7b,d,c, and e. This is because the arc roots are not moving as fast as the gas in and around the column of the arc. The forward movement of the column is being impeded by the arc root. In the fast mode, the arc is swept backward in the direction opposite of travel, indicating that the aerodynamic forces on the arc column are limiting the transit speed of the arc. The vertical flow velocity induced by the arc is comparable to forward velocity in the creeping mode but negligible in the fast mode. This disparity of vertical flow velocity and the arc transit velocity is indicated by the hot semi-luminous gas present above the arc when it is in creeping mode but which is swept into the low-pressure region behind the arc when it is in fast mode.

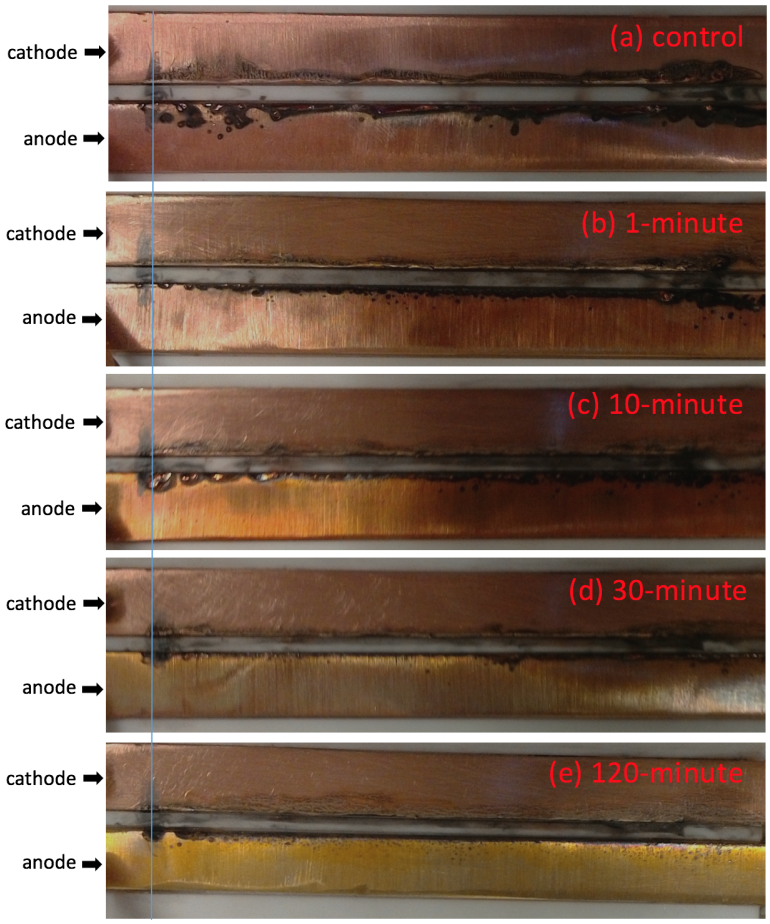

Figure 5.6: Electrode damage for 2 mm rail spacing with variable oxidation. The ignition site is indicated by the blue line on the left.

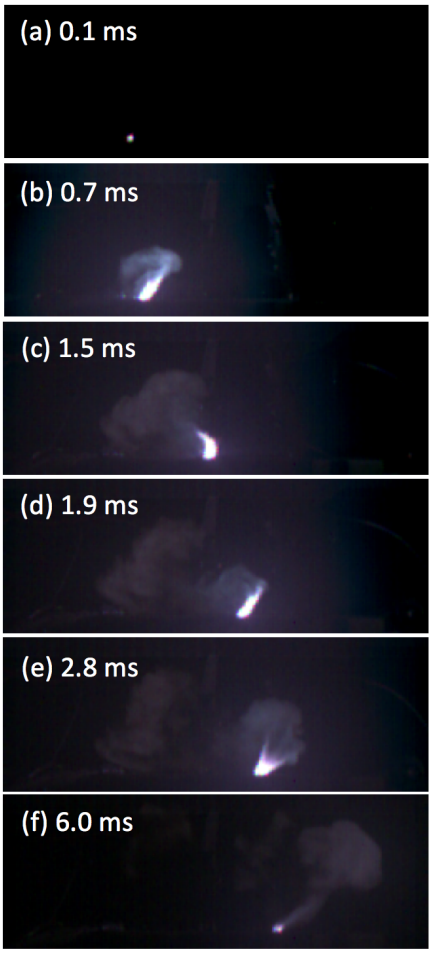

Figure 5.7: Side view of arc movement transitioning from post-ignition anchoring (0.1 - 0.7ms) to fast mode (1.5 ms) and then to creeping mode (1.9 -6.0 ms).

In more oxidized rails, this creeping mode is either not present at all or significantly reduced. The 1-minute oxidation starts out similarly to the control rails and then transitions into a faster mode around 1 ms, which corresponds to the peak current of the shot. The later shots are much faster after their post-ignition anchoring and then begin to slow down as the current nears its peak. Initially, the 10-minute oxidation case shows a similar burn-in effect to the fully reduced control, however, after 2 shots it reaches a steady state fast mode with a comparable velocity to the previously observed fast modes. For 30-minute oxidation levels and greater, the first shot is slower than the subsequent shots but still moves at $\sim$40 m/s. This is much faster than the creeping mode observed in the control case. Notably, the arc never fully anchors regardless of oxidation depth. This is presumably due to the stronger magnetic field experienced by the roots for the 2 mm electrode spacing which in turn produces a larger force on the roots, as discussed by Choi et al. [66].

Electrical data shows similar trends to the 5 mm rail spacing cases, but variation is most dramatic if shots with creeping mode and shots without are compared instead of oxidation levels. Plots of comparative data are shown in Figure 5.8. As before, arc resistance and arc power are higher for less oxidized cases with strong creeping mode arcs. This implies that it takes less energy for the arc to move quickly than to move slowly. Presumably this is due to thermal losses to melting and vaporization of rail material which is considerably higher as evidenced by the greater damage to rails by the creeping mode arc shown in Figure 5.8. The rise in resistance may be due

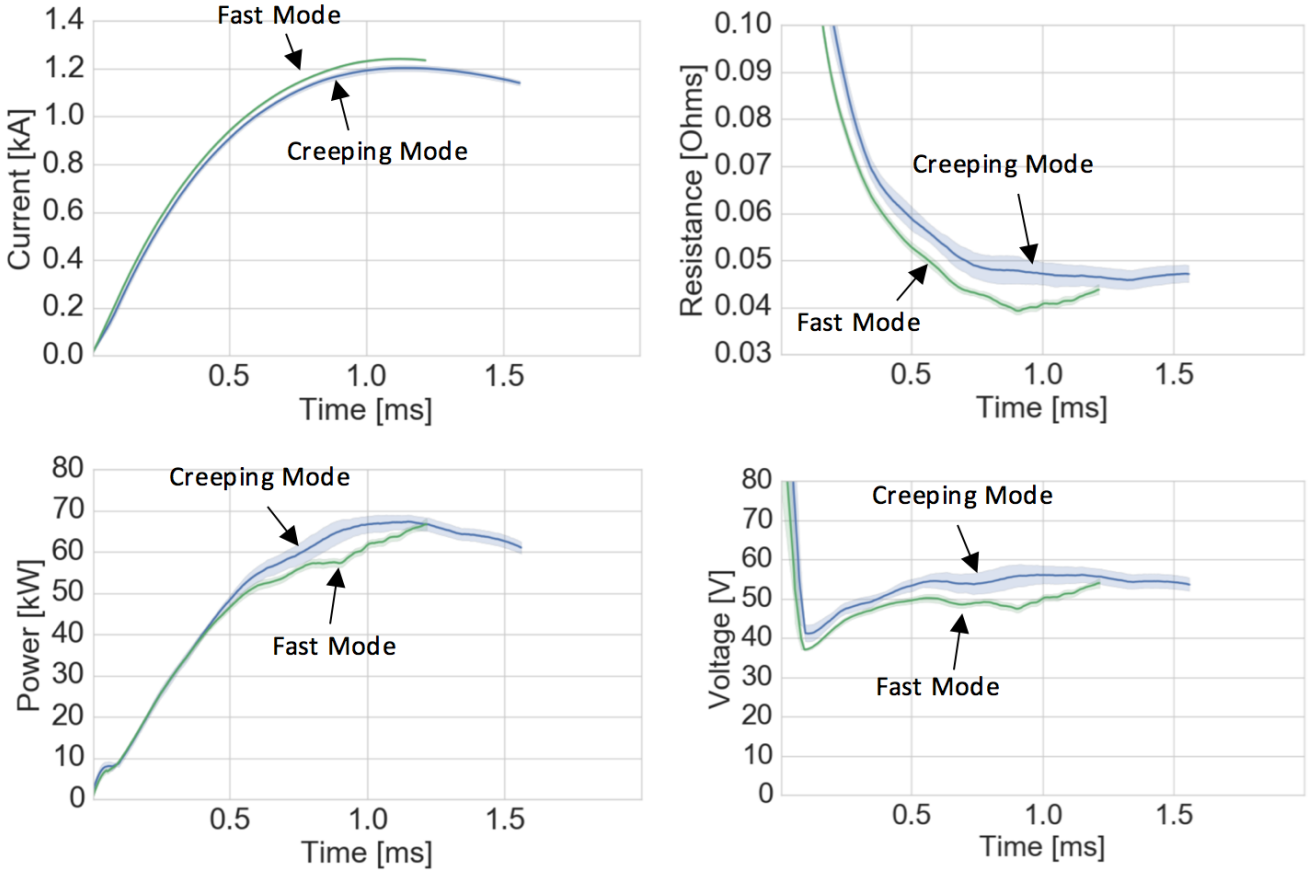

Figure 5.8: Electrical characteristics for oxidized rails with 2 mm rail spacing.

either to an increase in the length of the current path of the arc, or because of a drop in arc conductivity due to a higher percentage of metallic vapor in the arc. Metallic vapor can dramatically change the current and temperature distribution in the arc, and has been shown to increase gliding arc velocity in numerical simulations [71, 76].

Damage in the 2 mm rail spacing case follows the same trends as the 5 mm rail spacing cases but the trends are considerably more dramatic. The control rails, shown in Figure 5.6a, are severely damaged by the creeping mode arc with damage extending several millimeters out onto the surface of both the cathode and the anode. There is severe melting and surface damage for the control case with localized vertical deformation of the electrode on the order of $\sim$0.1-1.0 mm. Damage is significantly less severe in the more oxidized cases and is virtually absent from the 30-minute and 120-minute oxidation cases. The 10-minute oxidation case has similar damage to the control case near the ignition site due to the creeping mode on its first shot, but damage is much less severe away from the ignition site.

5.5 Discussion

There is a clear change in the behavior of the arc for arc-treated rails, and that effect is strongly correlated with the introduction of a thin oxide layer on the surface of the anode, indicating that the cause of the change for the arc treated behavior may be the presence of the oxide layer on the anode. This also suggests that the fast and creeping modes of the arc are determined by the

anode arc root, however, the mechanism by which the oxide layer affects the anode root is not clear. There are two primary observable differences between oxidized and un-oxidized anode roots. Oxidized anode roots preferentially attach to the inner edge of the anode, and oxidized anode roots do not anchor as easily (if at all) to the surface of the anode.

Given that the arc treated behavior is not fully recovered for the heat oxidized anodes and often requires at least one shot before the peak velocity is achieved, there is also something being altered specifically by the arc. There are several way the arc may be altering the oxidized surface.

The arc could be forming electrets in the oxide layer as discussed by Guile and Rageh [29, 34, 35]. Electrical fields from these electrets could then affect the arc. The quasineutral region of the arc would be slightly polarized by such a field but the anode sheath which maintains a positive space charge could be strongly affected. However, the sheath on an arc at this pressure should be $\sim$ 30 nm [77, 78]. The relative size of the sheath compared to the rest of the arc makes the validity of this explanation questionable.

Electrode material transfer in high intensity arcs is a well known phenomenon dictated by current levels and electrode spacing [25, 26, 79]. The arc is likely selectively removing oxidized copper from some parts of the electrode and increasing oxidation in other locations. Arcs with large gap distances and high currents as in our experiments promote oxidation of the anode and sputtering of the cathode [79]. This could lead to preferential attachment through local increases or decreases in electrode conductivity by variable increases in

the anode oxide layer depth.

Variable oxidation becomes particularly attractive as a possible mechanism when the properties of different oxides are examined. Copper forms two types of oxides. CuO is formed primarily at temperatures of 300-1000°C while Cu_2O is formed primarily for temperatures below 200°C [80]. Valladeres found that oxidation layers which annealed at 1000°C have resistivity a factor of 10^7 higher than oxide layers annealed at 200°C which are themselves another factor of 10^7 more resistive than pure copper.

The experiments discussed in this chapter showed that rails oxidized at 200°C promote smooth anode root movement, though they do not promote it as well as arc-treated rails. We believe this is because the arc-treated rails form an oxide layer primarily composed of the more resitive CuO while the oven treatment at 200°C generates an oxide layer primarily composed of the less resistive Cu_2O. So, if arc attachment or root formation behavior at the anode can somehow be tied to resistivity of a thin layer on the electrode surface, this is a good explanation for the varying behavior of the arc transit behavior on oxidized rails. This hypothesis motivates the computational work presented in the next part of this chapter.

5.5.1 Computational Results

Simulations were run using the VizSpark thermal plasma computational tool with a domain like the one shown in Figure 5.9 [67]. The domain consists of a gas subdomain on top which is 0.8 mm thick and a metal subdomain

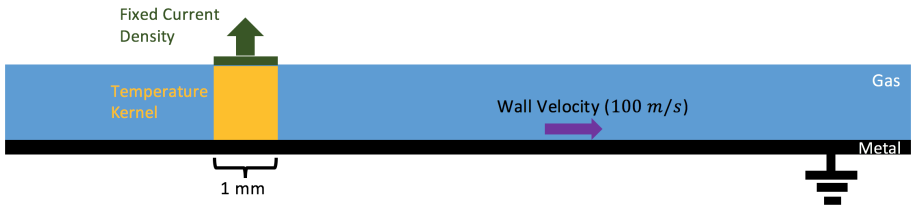

Figure 5.9: Computational domain. The fixed current density boundary condition is indicated in dark green and the initial temperature kernel used to initiate the arc is shown in gold.

below which is 40 μm thick, approximating an oxide layer. An arc is initiated by a 15000 K temperature kernel and sustained by a fixed current boundary condition at the top of the gas subdomain. The bottom of the metal subdomain is grounded to simulate a highly conductive metallic electrode below the simulated metal subdomain. The metal is thermally insulated and the interface is set to move at 100 m/s to the right starting impulsively at time, t=0. The gas is initially at rest. The metal subdomain is set to mimic copper for a control case and the electrical conductivity is reduced by a factor of 10^6 or 10^7 in the test cases to simulate thin resistive oxide layers $\sim$0.1-1 μm thick. Results for all three are shown in Figure 5.10. No external magnetic fields are applied, so any movement of the arc root is due to the moving wall.

Typical oxide layers on copper are between $\sim$10 nm and $\sim$1 μm so a 40 μm simulated oxide layer is quite thick compared to real oxide layers. While it is computationally infeasible to simulate thinner oxide layers, the only physical change from a thick oxide to a thin oxide should be the increased potential drop across the oxide layer. This will result in greater field enhancement

at the surface of the oxide layer far away from the attachment site of the arc. However, simulation variations show that the electric field enhancement at the leading and trailing edges of the arc root are linearly dependent on both conductivity and oxide depth, allowing simulations to achieve similar conditions to a thinner oxide layer by maintaining the same oxide thickness but increasing the oxide conductivity.

Clear differences are apparent in the attachment mode of the arc. The test cases in Figure 5.10b and 10c with resistive oxide layers force the arc to attach diffusely to the electrode. The attachment site location of the arc is unaffected by the moving wall of the electrode on the upstream side of the arc for the lowest conductivity in Figure 5.10c. The downstream side of the arc is swept away, making the arc attachment site highly diffuse. The spreading rate of the attachment site is increased by decreasing conductivity. The control case in Figure 5.10a mimics pure high conductivity copper and has a constricted attachment site which is swept downstream slightly by the moving wall. This supports the hypothesis that a resistive layer on the surface of the anode increases the mobility of the anode root, allowing it to move smoothly over the surface of the electrode. In contrast, a highly conductive surface layer discourages movement of the root as in Figure 5.10c which shows almost no movement of the leading edge of the arc root.

The constricted attachment site present for the pure copper surface is considerably hotter than the diffuse attachments in the simulated oxide layer cases. The increased temperature would be expected to lead to spot formation

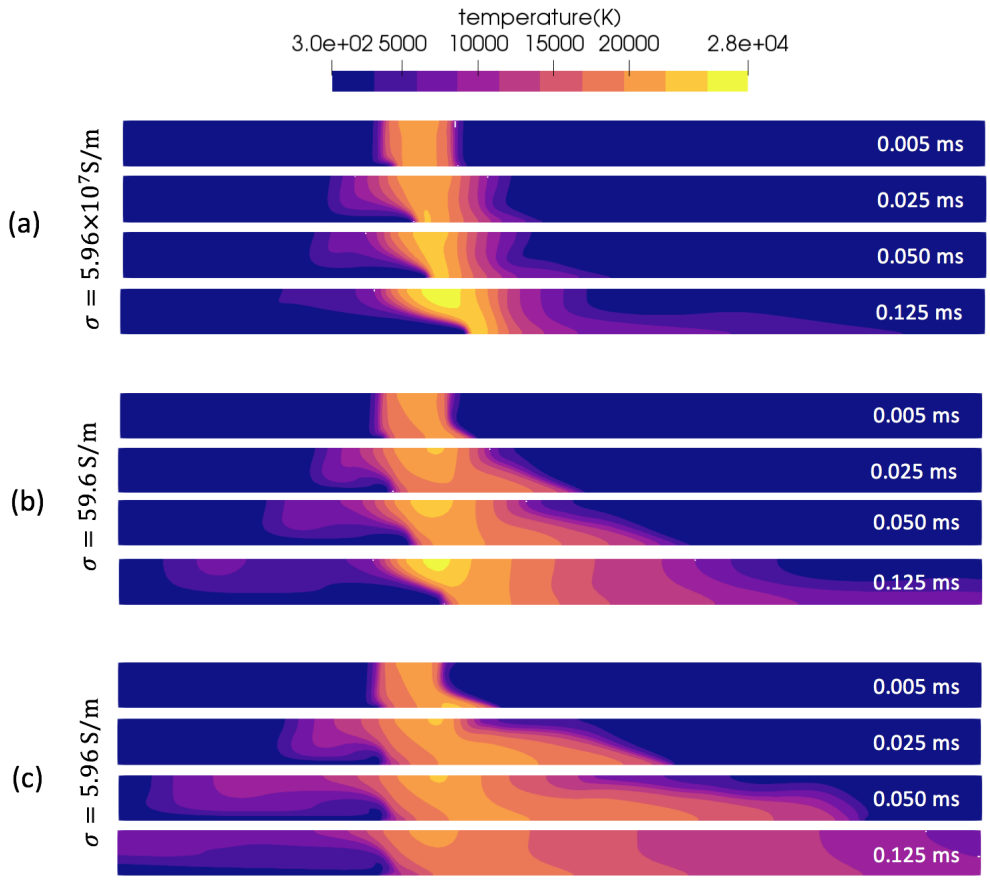

Figure 5.10: Computational results of arc root temperature with varied conductivity 40 μm electrode.

and eventual anchoring on the electrode surface in a physical situation. This constriction also increases the voltage drop across the arc compared to the diffusely attached cases with the simulated oxide layer. This may partially explain experimental results showing that the RailPAc circuit is less resistive with oxidized electrodes.

The edge of the attachment site of the arc experiences a field enhancement inversely proportional to the conductivity of the electrode surface. Electric field magnitudes at the leading and trailing edges are low for a conductive copper electrode surface, but can be extremely high for a resistive electrode surface. This increased electric field causes local Joule heating to increase as shown in Figure 5.11. This Joule heating causes the attachment site to diffuse outward at a rate comparable to the wall movement velocity for the test cases shown.

The last effect of the change in surface conductivity is the formation of a jet directed in the opposite direction to the movement of the wall, corresponding to a jet moving in the direction of the arc roots motion for a physical case. This is particularly obvious when looking at Figure 5.12 where the streamlines bend further towards the horizontal in simulatons with lower conductivity electrodes. The jet forms due to current traveling sideways through the trailing edge foot of the arc root. Current traveling this direction is pinched by self-induced fields, creating a magnetically pumped jet. The larger the trailing edge foot, the stronger the jet. This jet blows hot gas ahead of the root, which would be expected to aid forward movement of the root by generating

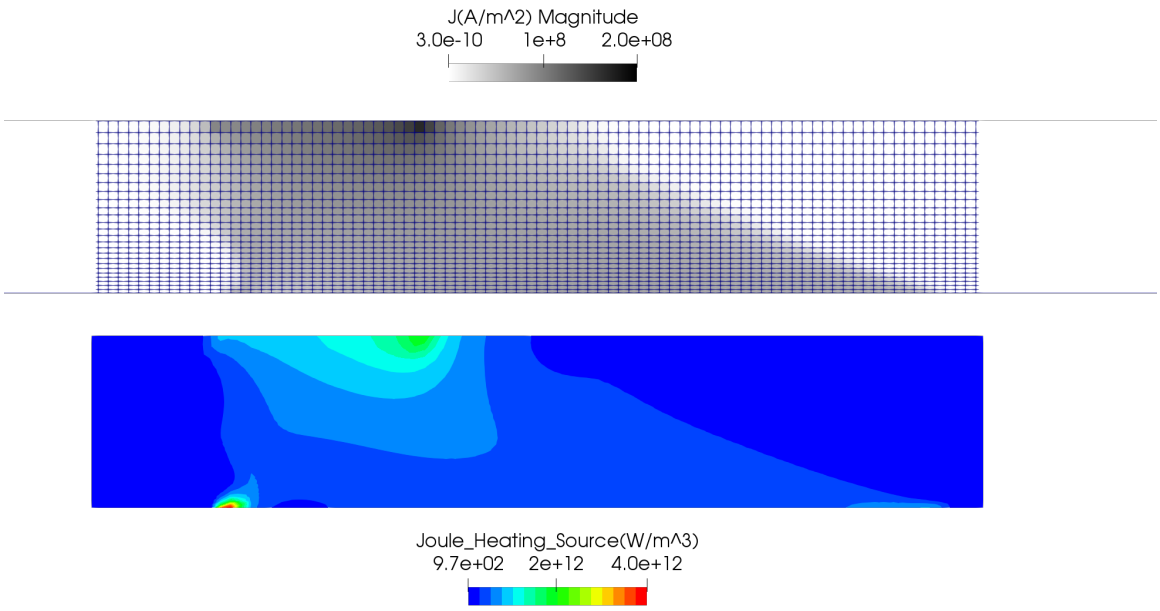

Figure 5.11: Local Joule heating enhancement and simulation grid size for $sigma = 59.6 S/m$ at t=$50 \mu s$.

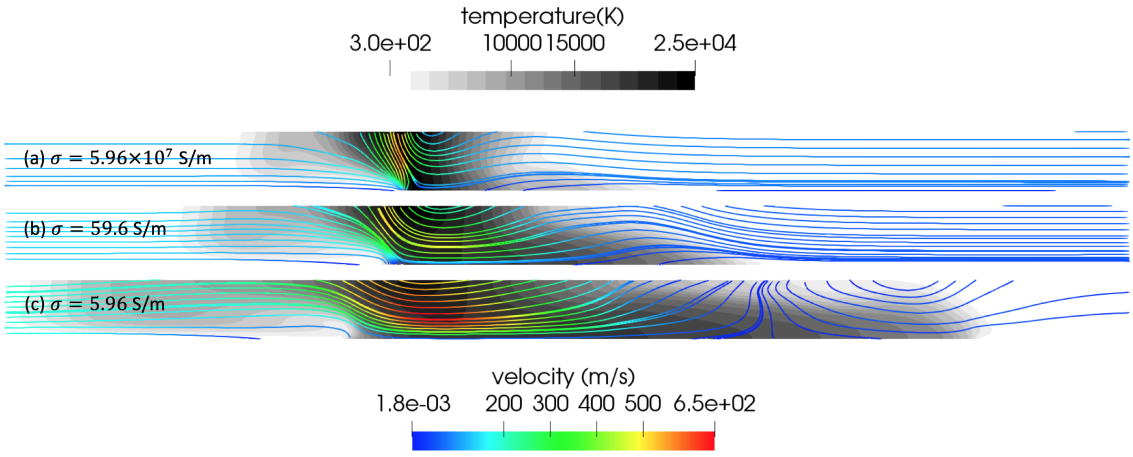

Figure 5.12: Computational results of arc root streamlines for different conductivities at t=50 μs.

conduction pathways from the main column to points on the electrode surface downstream of the root. Note that the streamlines here are calculated in the lab frame (Galilean transform 100 m/s to the right) rather than the arc frame which the simulation was run in, so most of the fluid appears to be moving from right to left with the wall stationary.

These simulations strongly support the hypothesis that the change in arc behavior is due to the increased resitivity of the electrode oxidation layer. We beleve the anode root is creating a thick predominantly CuO oxide layer on the anode surface. On subsequent firings the arc root is forced to attach diffusely to the now oxidized surface. This diffusive attachement promotes fast movement by directly moving the edge of the attachment site by strong Joule heating and indirectly by convecting conductive gas ahead of the attachemnt

site promoting restrikes downstream of the arc root.

Chapter 6

Arc Aerodynamics

6.1 Introduction

This chapter seeks to further explore aerodynamic drag on the arc column computationally. Unsteady two-dimensional simulations with naturally evolving arc radii and full three-dimensional simulations of simple RailPAc geometries will be presented. Drag and qualitative flow characteristics will be examined, and the mechanism by which momentum is transferred to the surrounding gas from the arc will be discussed [42].

6.2 Two-Dimensional Simulations

While two-dimensional simulations are computationally less expensive than similar three-dimensional simulations, they also present a unique challenge; electromagnetically, gliding arcs are inherently three dimensional due to the importance of $\vec{J} \times \vec{B}$ forces, where the primary component of $\vec{J}$ is axial along the centerline of the arc but $\vec{B}$ is primarily orthogonal to $\vec{J}$. This cross product leads to a force vector in the remaining third dimension orthogonal to both $\vec{J}$ and $\vec{B}$. For fluid models, the Lorentz force manifests as a simple body force contained entirely in two dimensions (provided the arc has no axial

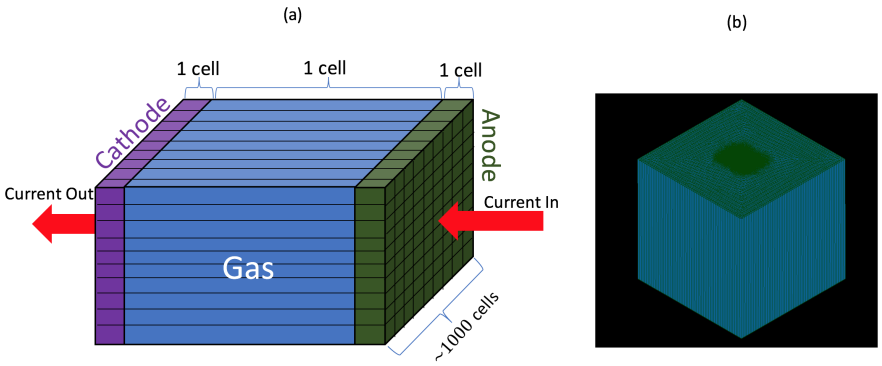

Figure 6.1: Pseudo 2D simulation domain. A schematic of the domain is shown in (a) to show the electrode and gas layers which are not visible in the full domain shown in (b) because they are only as thick as the smallest cell size.

variation), but this force can only exist if current is traveling in the third dimension. To get around this problem, a pseudo third dimension is simulated by solving the equations for arc behavior in a three-dimensional domain which has $\sim 1000 \times 1000$ cells in two dimensions but is only three cells thick in the third dimension. A schematic of this mesh is shown in Figure 6.1a while the actual mesh is shown in Figure 6.1b. Two outer layers of cells act as electrodes while the inner layer of cells is solved as a gas. The interface of the gas cells and electrodes are insulated and inviscid so that the fluid equations are two dimensional. The gas cell is 40 cm long compared to the arc radius of $\sim$1 cm, so that the arc induced magnetic fields approach the same values as an arc of infinite length. Constant current boundary conditions are applied on one electrode to prevent uncontrolled growth of the arc while the other is set at ground voltage. Simulations are run at several current levels and applied

magnetic fields. This allows for calculation of drag coefficient and analysis of transient phenomena in the development of the arc column in the early stages of its transit. Quantities like actuation efficiency and slip velocity can also be calculated.

All results from the two-dimensional simulations share certain features. The arc is initiated by a temperature kernel with parabolic temperature distribution. The peak temperature of the kernel is 24000 K and the radius is 5 mm. The ambient gas temperature is set to 300 K. The temperature distribution for a representative case is shown in Figure 6.3. The arc immediately grows after initiation. While an equilibrium size is expected to be reached, the arcs in these simulations never reach a constant area. Growth slows down with time as can be seen in Figure 6.2, but it is difficult to say if it will ever fully stop. This may be due to the weak electromagnetic coupling between the electrode and gas layers of the simulation or overestimates of Joule heating, as a physical free-burning arc would be expected to reach some constant cross-sectional area [40].

Given that these simulations demonstrate non-physical arc growth, they should not be expected to make one-to-one predictions regarding propagation velocities as a function of electrical inputs, however, they do offer insight into the coupling of the arc movement with the surrounding flow. The mechanism by which momentum is transferred is of particular interest.

As can be seen in Figure 6.3, the momentum magnitude is largest immediately behind the shock produced by the initiation of the arc (visible at t=0.1

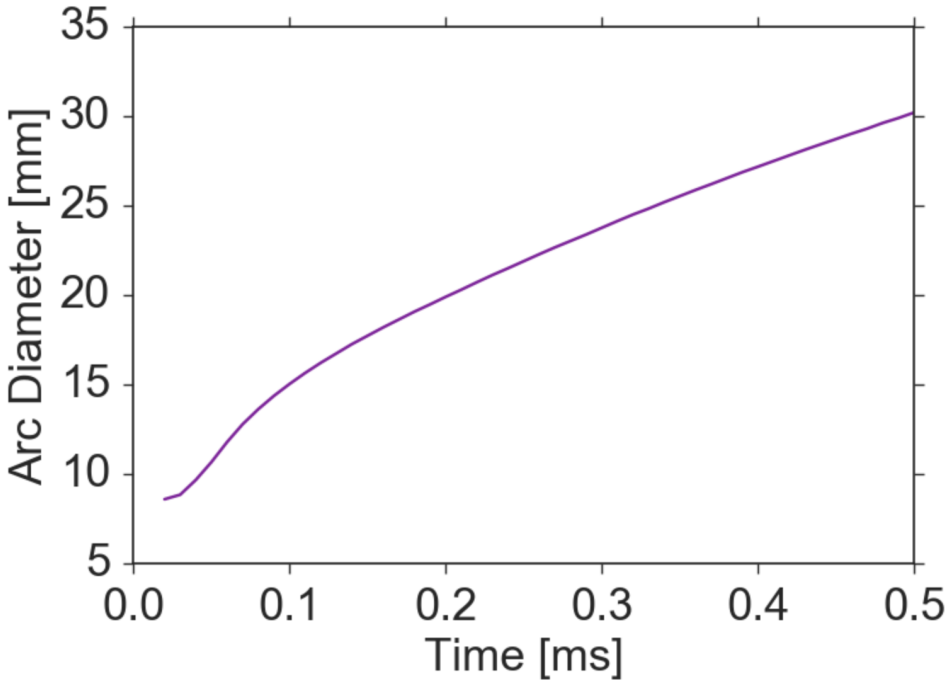

Figure 6.2: Arc diameter growth with time.

ms), and in the areas immediately in front and behind the arc where fluid is being respectively compressed and entrained. These regions all represent areas with large pressure gradients, as can be observed in the pressure distributions of the same arc shown in Figure 6.4. The fluid inside of the arc actually carries very little fluid momentum due to its low density, despite moving at nearly twice the velocity of the arc. Forcing inside of the arc is communicated outside through pressure gradients across the arc so that a low-pressure region is formed behind the arc and a high-pressure region is formed in front of the arc. The largest area of momentum is generated in the region immediately behind the arc. This high momentum region is visible in Figure 6.3 at t=0.5 ms. Fluid in this area actually achieves velocities 40-60% higher than the velocity of the arc. This high momentum fluid eventually forms a jet which bisects the arc remnant as shown at t=1.0 ms in Figure 6.3. It may cause some confusion that the fluid inside of the arc moves so much faster than the arc itself however this apparent inconsistency is rectified by two points. Firstly the density of the fluid is very low compared to the outside of the arc, and secondly the flow inside of the arc consists of two counter-rotating vortexes. The peak centerline velocity of a vortex ring is faster than the forward propagation velocity of the ring. The same is true for the arc vortexes which allow for a much higher centerline velocity than the velocity of the arc as a whole.

The shock shown in Figure 6.4 rapidly deteriorates from a shock wave to an acoustic compression. Compression waves are continually generated from the front of the arc while it is being forced so that more fluid is con-

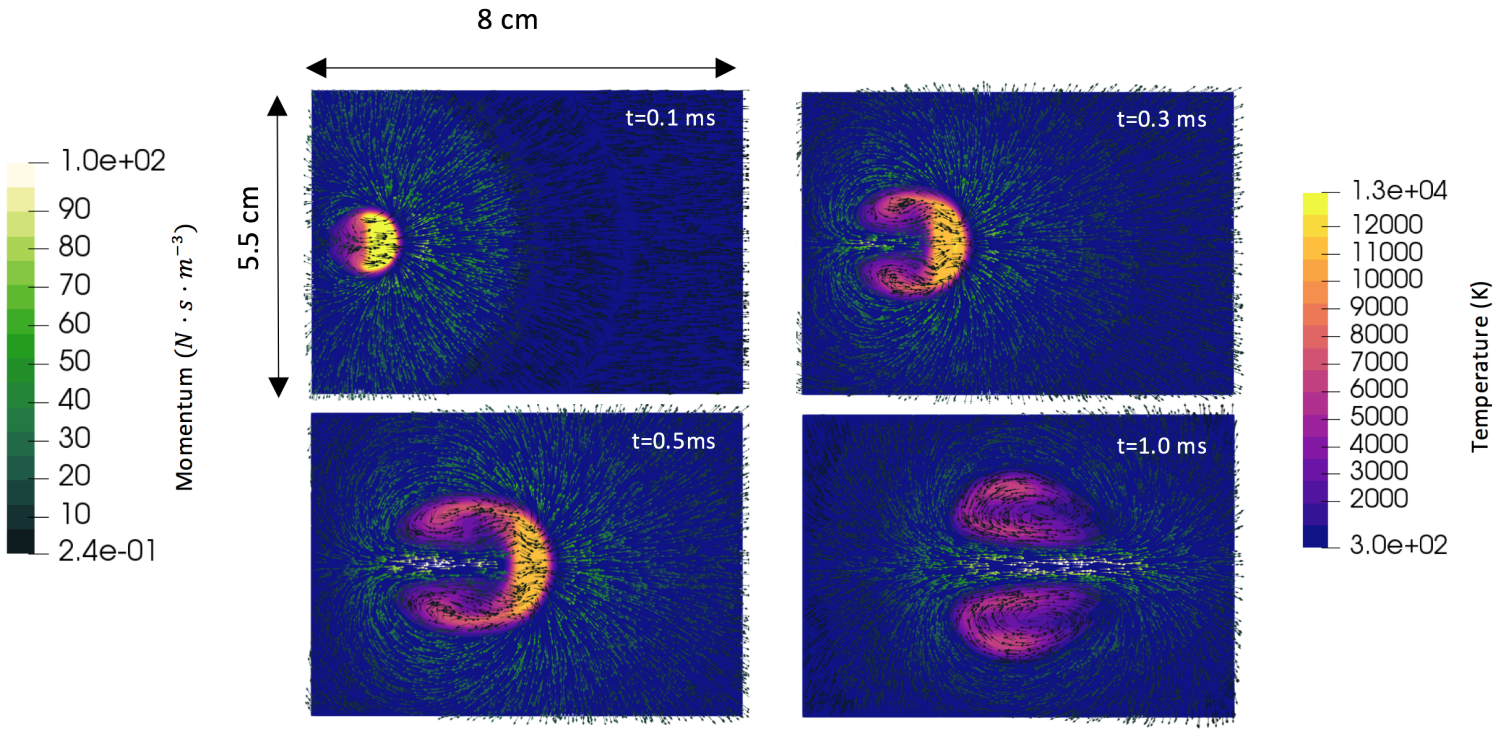

Figure 6.3: Temperature distributions for arc with ∼1000 A integrated current and 0.1 T applied field. The arc current is dropped to zero at t = 0.5 ms and the flow field is allowed to evolve. Fluid momentum vectors are also shown.

tinually processed. The flow in the area immediately around the arc, behind the compression waves, reaches a quasi-steady state in only a few tenths of milliseconds. The arc continues to change shape and grow; however the local pressure distribution around the arc remains approximately the same, and the total momentum in the flow, ρu, near the arc (in the region marked by the green box in Figure 6.4) remains constant after the compression wave passes out of the region. This is illustrated by Figure 6.7 which shows the integrated momentum and pressure terms for the inner computational domain but not the outer buffer region. The speed with which the arc reaches this steady state implies that more efficient jet creation can be achieved by shortening the arc lifetime and maximizing arc forcing.

For a given arc current and applied field, the arc moves at a nearly constant velocity. This is illustrated in Figure 6.7. Momentum addition from the electromagnetic fields does not continually accelerate the surrounding fluid to greater velocities, but instead entrains more fluid into the jet created by the arc passage. This has significant implications for the arc as a flow actuator, since local jet velocities may be more important than global flow properties. Additionally, the arc velocity as measured by change in position of the rapid temperature rise in the gas at the front of the arc is very nearly identical to the local fluid velocity at the temperature front. This is illustrated in Figure 6.7, and implies that there is little to no through-flow from inside of the arc to the outside or vice versa. Arguments that the arc may be approximated as an impermeable body are thus partially validated by our model. These

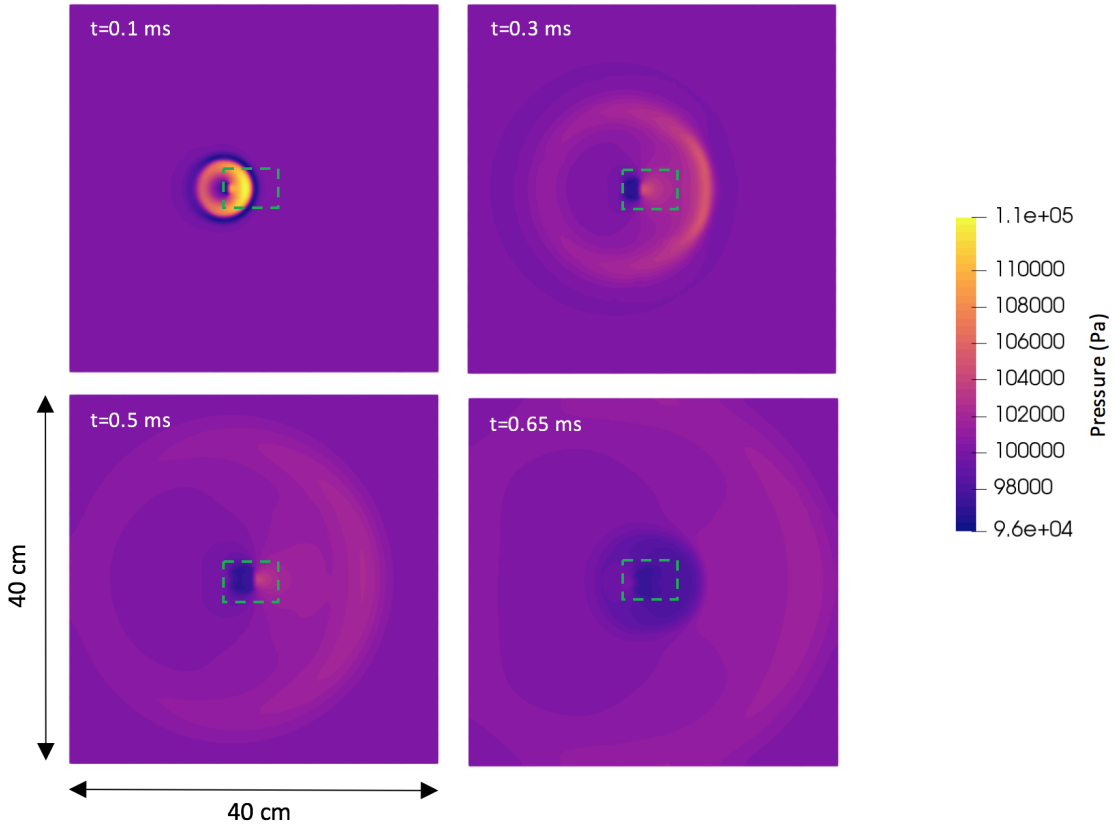

Figure 6.4: Pressure distributions for moving arc with integrated current ∼1 kA and applied field of 0.1 T. The current is turned off at t=0.5 ms causing the change in orientation of pressure gradients in the horizontal direction at t=0.65 ms. The full simulation domain is shown here. The green dashed box in each sub-figure represent the portion of the simulation viewed in Figure 6.3.

arguments are further supported by looking at the streamlines in Figure 6.5. Note that there is a region where the streamlines are closed within the arc in the streamlines calculated in the arc frame in Figure 6.5b. There are also streamlines which begin at the edges of the arc and exit off the left side of the figure. This is due to volumetric expansion of the arc due to heating of fluid as it sweeps past the arc. Since the thermodynamic variable of presure, temperature, and density within the arc are not significantly changing the only way for this to occur is for the arc to be processing new fluid. This seems to occur by fluid passing from the small mixing layer at the top and bottom edge of the arc into the space behind the arc where it is heated and then allowed to move into the arc. So if any fluid is added to the column it must enter through the back of the arc.

Arc Vorticity is shown in Figure 6.6a. While the shear term matches almost perfectly with the vorticity distribution, this is because it represents a sink of vorticity. The magnitude is largest of the three terms but it is very localized so it doesn't dominate the other two terms and only serves to prevent vorticity from convecting away from the arc as it passes. The baroclinic and body force terms are of similar magnitude to one another but peak at different locations. The baroclinic term is only present at the front of the arc while the body force term is present everywhere there is vorticity.

Examining several variations of applied fields and integrated currents, it becomes clear that the arc velocity is much more strongly dependent on the applied field than it is on the integrated current for currents above $\sim$1 kA.

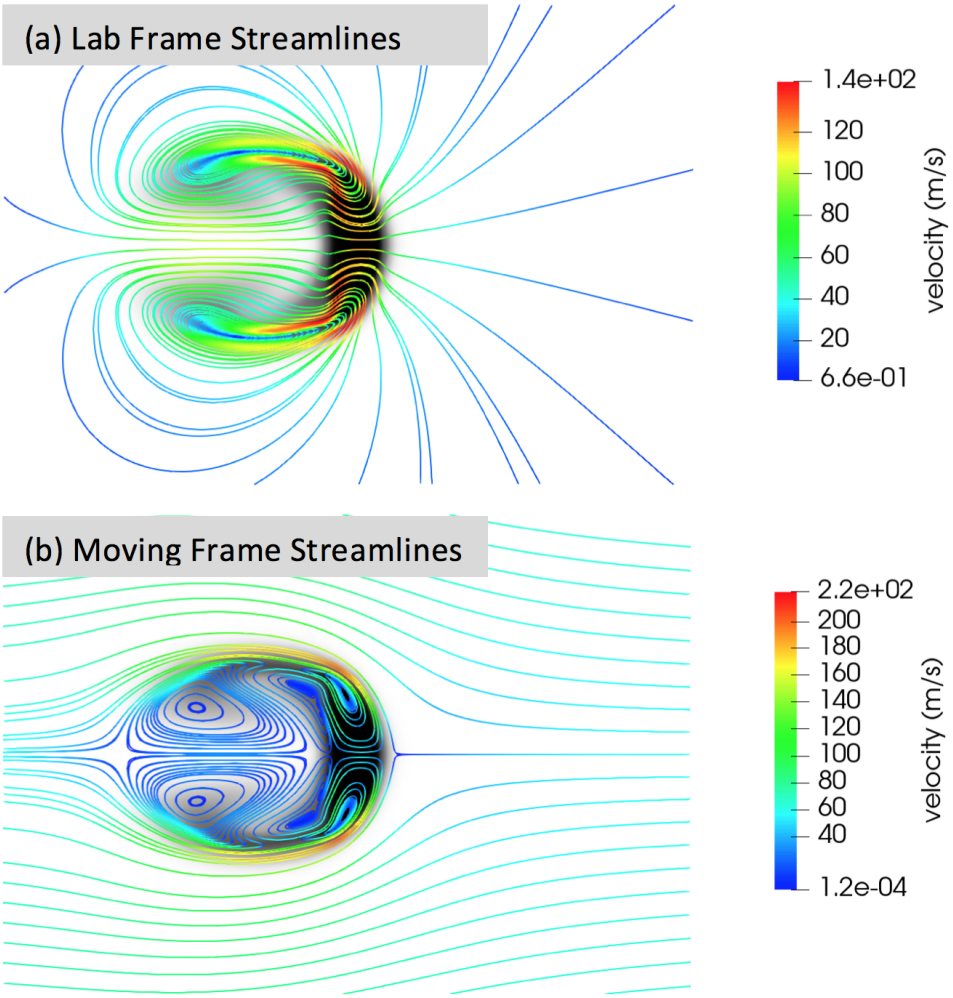

Figure 6.5: Streamlines for the moving arc calculated using the lab frame (a) and a frame which moves at the same speed as the front of the arc (b). The data used comes from the same simulation as that shown in Figure 6.3 at t=0.5 ms. A normalized temperature is shown in black to indicate the location of the arc.

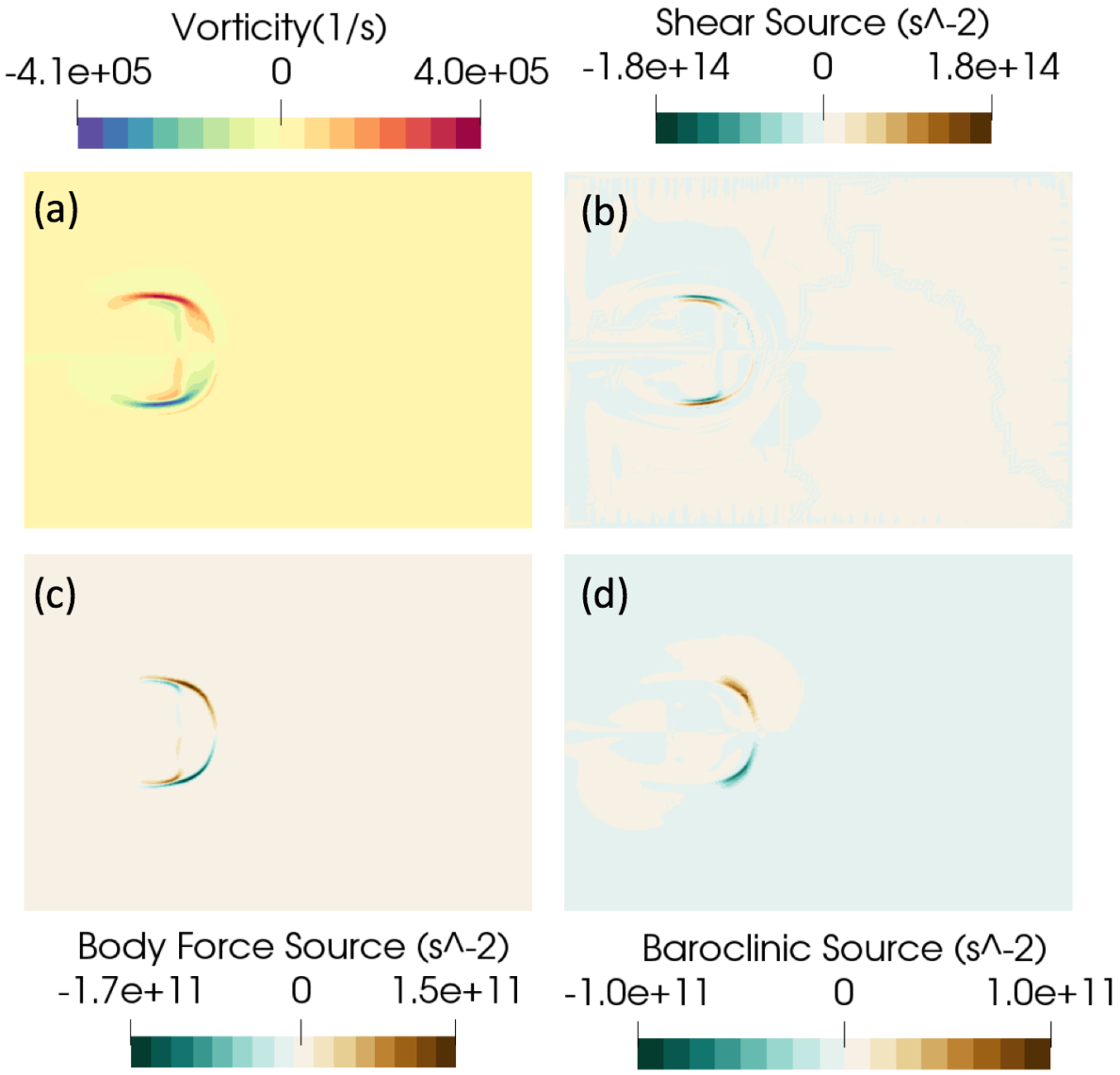

Figure 6.6: Vorticity for the arc at 30 μs is shown in (a) while vorticity source terms from shear, body forces, and baroclinicity are shown in (b), (c), and (d) respectively.

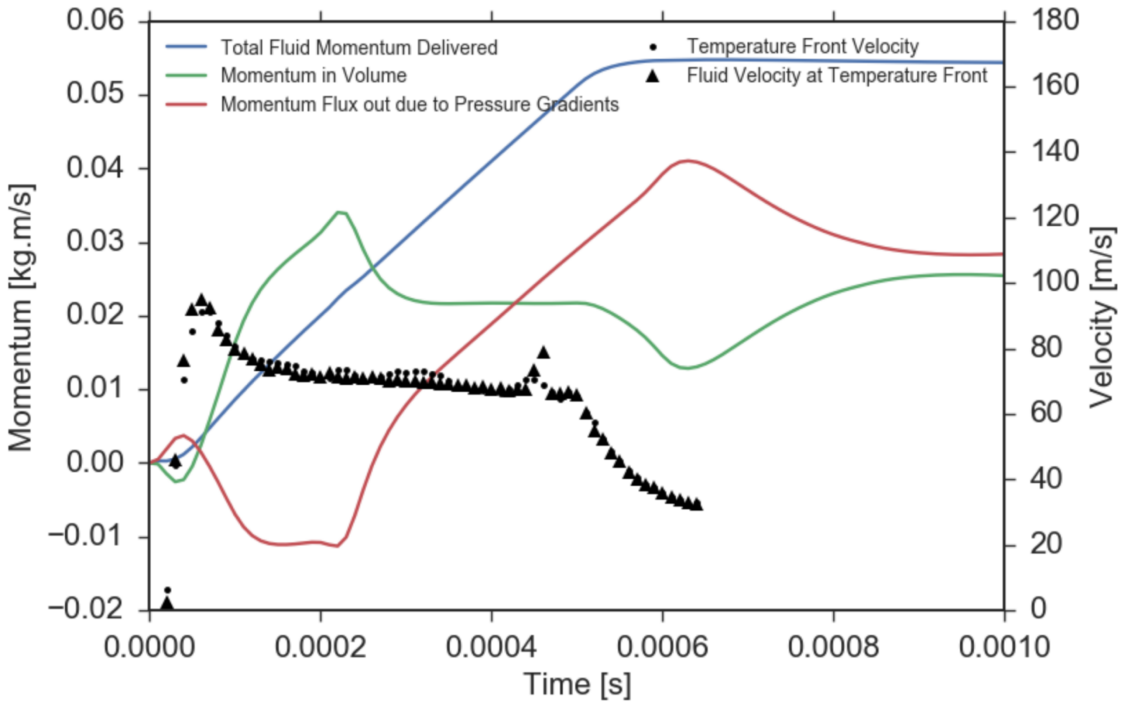

Figure 6.7: Decomposition of momentum delivered to the flow and arc velocities with respect to time. Velocity values truncate at 0.65 ms because the temperature front is bisected by the entrained jet and the location of the temperature front becomes undefined.

Presumably this is due to the fact that the arc diameter is dependent on the current but not the applied field. Results for variation in each parameter are shown in Figure 6.8. This increased dependency of the arc velocity on applied field over integrated current has been observed in experiments [42, 43] and has significant implications on flow actuation efficiency. An arc may achieve the same local jet velocities with much lower integrated current by simply increasing the applied field. There are many methods this may be achieved, several of which are discussed in Chapter 3. The results shown in Figure 6.8 suggest that the square of the arc velocity at 1 kA is roughly linearly dependent on the applied field. Literature results corroborate this finding [41–43, 81]. Myers [41] reaches the result analytically by assuming a constant value for the arc drag coefficient C_d. It is interesting that the result still holds here, given that the drag coefficients for the simulated arcs are continually dropping due to the growing diameter of the arcs. Calculated drag coefficients of the arc are between 1 and 3 after the initial rapid expansion of the arc (t>0.05 ms), with an average value across all simulations of 1.65, slightly higher than a simple cylinder.

Efficiency of an arc for flow actuation may be evaluated through analysis of the work done by the system on the fluid compared to the total input energy. This efficiency is calculated by,

$$Efficiency = \frac{work\ per\ second}{total\ power} = \frac{\vec{F} \cdot \vec{v}}{I^2 R} * 100\%, \tag{6.1}$$

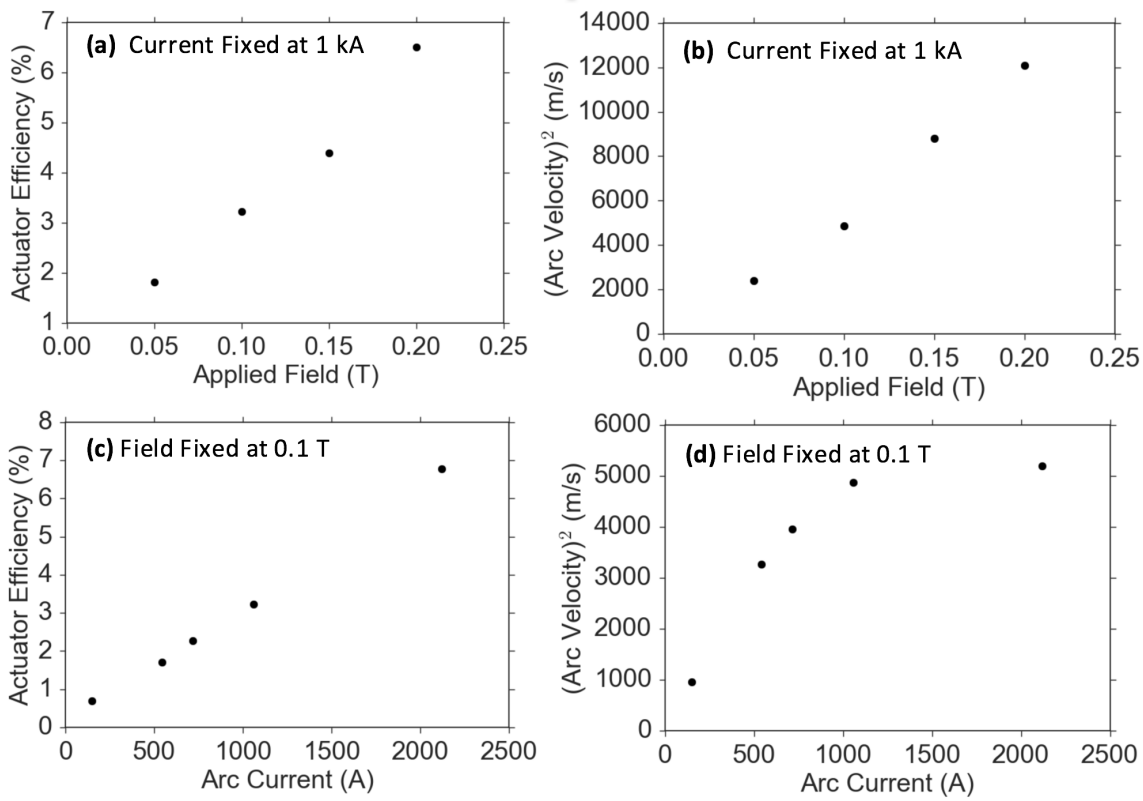

Figure 6.8: Velocity variation and efficiency variation with varied current and applied field.

where $\vec{F}$ is the total force delivered by the arc, $\vec{v}$ is the arc velocity, I is the integrated current and R is the arc resistance. The efficiency gives an idea of the level of total momentum added to the flow. An alternative performance metric of arguably greater merit is the peak velocity of the arc, since a larger local momentum and lower global momentum may be preferable for actuation purposes compared to a lower local momentum but higher total momentum.

6.3 Three Dimensional Simulations

Full fidelity three-dimensional simulations were run with 2 different configurations [67]. The first configuration simulates cylindrical electrodes with a diameter of 1.5 mm and length of 1.2 cm. The second uses 1.2 cm long electrodes with square cross-section with sides of length 1.4 mm. Both employ total integrated current of 1 kA. The rounded rails are free floating with an open gap between them, while the square rails are separated by an insulating dielectric like the flush mounted RailPAc geometry. Both configurations have inter-electrode spacing of 1.5 mm. The free-floating electrode case was run on 32 cores for 2 days to reach a simulated time of 0.35 ms, while the flush mounted case ran for 5 days on 32 cores to reach a simulated time of only 0.17 ms. Results for both cases are quantitatively highly unphysical. However, the goal of running these simulations was verification that, with more time and computational power, VizSpark might be used to make accurate numerical predictions of the RailPAc arc.

Results for the free-floating electrode geometry are shown in Figure

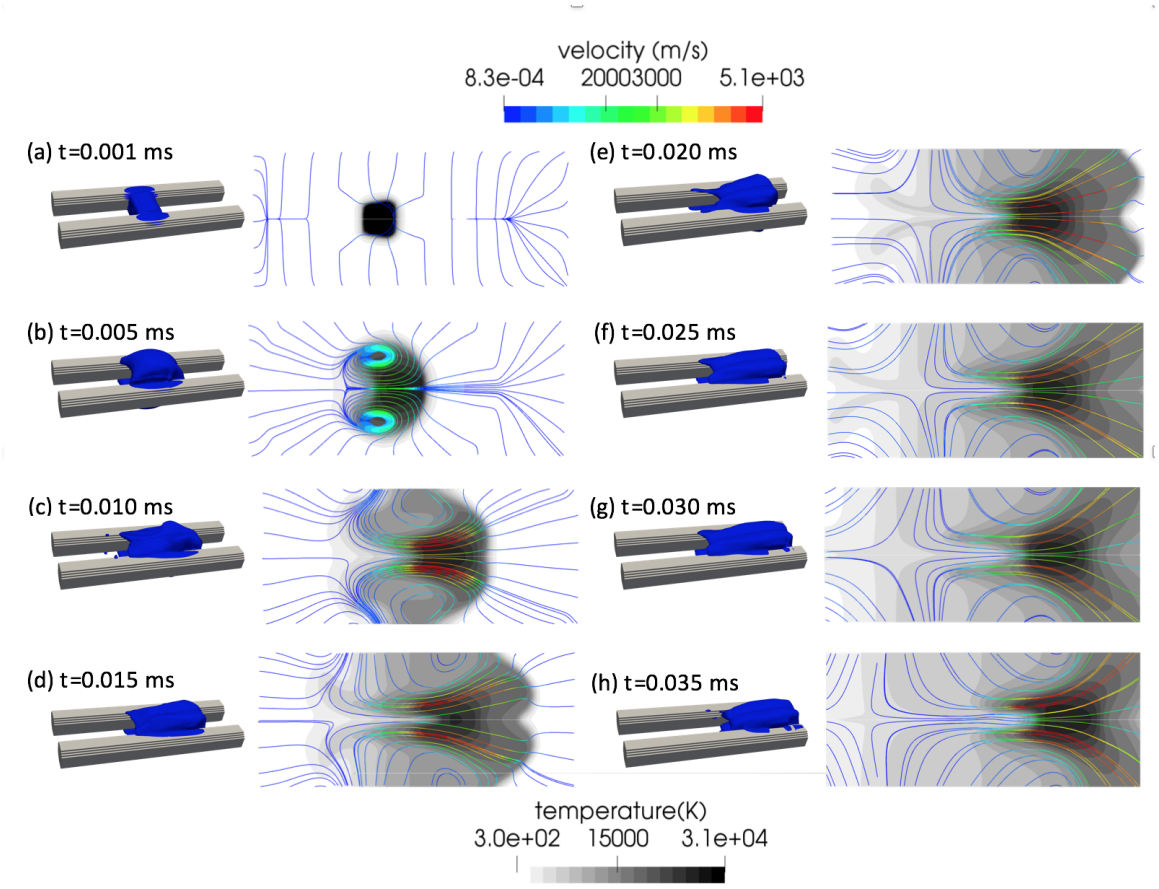

Figure 6.9: Time evolution of 5×10^7 A/m^2 current density contours, temperature distributions, and streamlines with rounded free-floating rails spaced 1.5 mm apart.

6.9. Electrodes are shown in gray and a contour of current density magnitude 5×10^7 A/m^2 is shown in blue. The arc moves at ∼360 m/s until it reaches the ends of the electrodes and slows down. The arc velocity is demonstrated in Figure 6.10 where streamlines are calculated for a frame moving at 360 m/s. A stagnation point is clearly visible at the front of the arc. The electrodes are thermally insulated and the boundaries between the electrodes and the gas are inviscid. Despite allowing for slip at the boundary the arc still has trouble moving from its initiation site. This may have implications on the mechanism of the arc root residence time phenomena observed in experiments discussed in Chapter 5. Given that this model only takes into account gas heating effects and electromagnetic effects, the finite residence time of the arc in the simulation results immediately after arc initiation may indicate that this phenomenon is independent of surface erosion effects.

As discussed above, the arc moves as a whole at ∼360 m/s but this value is very small compared to the flow velocities observed inside of the arc, which reach as high as 4 km/s. Results showing temperature and velocity distributions are shown in Figure 6.9. Larger versions are available in the appendix. This high velocity is believed to be unphysically large and a consequence of the necessarily coarse mesh used in the simulations. Despite these large velocities, the flow field around the arc is qualitatively similar to the two-dimensional simulations discussed previously, with the same counter rotating vortices forming on the top and bottom of the arc as shown in in Figure 6.10. Temperature distributions are also similar qualitatively but three-dimensional

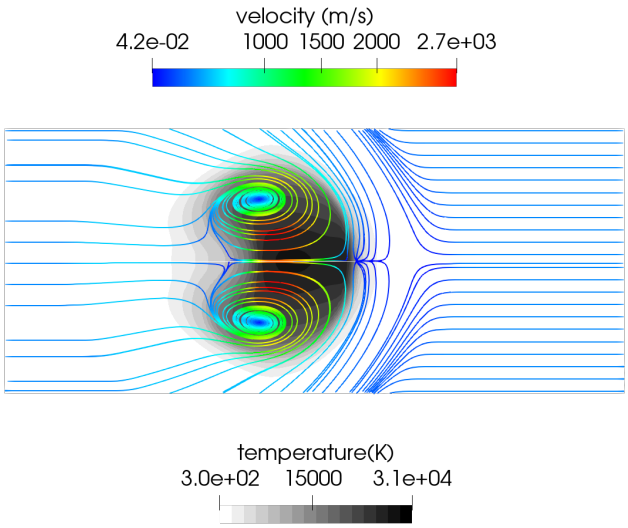

Figure 6.10: Streamlines for the centerline slice of the rods simulation at t=0.005 ms. The streamlines are calculated for a frame moving with the arc at a velocity of 360 m/s to the right.

simulation results are considerably hotter with peak temperatures ∼26000 K compared to ∼13000 K in the two-dimensional simulations.

The most notable difference between the two-dimensional and three-dimensional simulations comes as a result of the change in the applied magnetic field. The field in the three-dimensional simulations is induced by the simulated current instead of being uniformly applied. This means that different parts of the arc experience higher or lower fields and even field of opposite sense. Therefore, the net Lorentz force on the arc is not necessarily always directed down the rails and in fact, for the front nose of the arc, the force is directed backward because the magnetic field there is opposite in direction to the back of the arc. This causes the lobed appearance of the temperature distribution at the front of the arc starting at t=0.01 ms in Figure 6.9.

The second configuration examined simulates flush mounted electrodes. This configuration is considerably more computationally expensive due to the field enhancement at the kinks in the current as the current path navigates from the electrode into the arc as discussed in Chapter 4. The domain must also be larger due to the root jets which form and blow the arc away from the electrode surface and towards the boundary. So, while the free-floating case used ∼500000 cells, the flush mounted case used over 2 million cells. The shorter time step due to field enhanced Joule heating and the greater simulation size dramatically impact the performance of the solver.

Results for the 1.5 mm spaced flush mounted electrodes with integrated current ∼1 kA are shown in Figure 6.11. The arc is initially cylindrical in shape

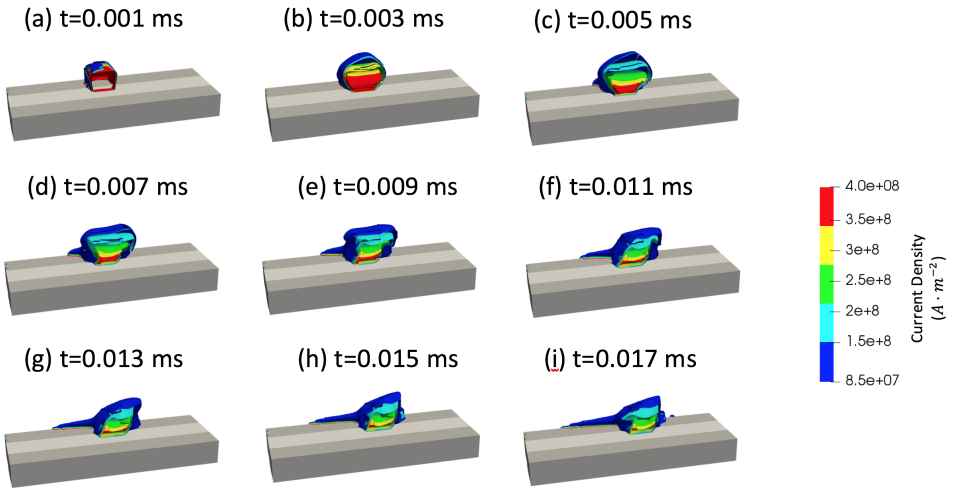

Figure 6.11: Cross section of current density contours for flush mounted electrodes. The electrode is shown in dark gray while the dielectric is shown in light gray.

but rapidly changes shape as the Lorentz force moves the arc forward. The sharp corners of the electrodes cause a field enhancement which encourages attachment of the arc along the outer edges of the electrodes, as in Figure 6.11f-i. The arc moves very slowly compared to the free-floating case. The average velocity of the arc propagation is only ∼70 m/s, though as in the free-floating case, simulated velocities inside of the arc are as high as 4600 m/s. As before, this is believed to be unphysically large. The drop the arcs propagation velocity in the flush mounted case compared to the free floating rods case is interesting and compares well with the similar factor of ∼10 drop in velocity from the fast mode to the creeping mode in the 2mm flush mounted case discussed in Chapter 5. The similarity to experiments is also shown by how

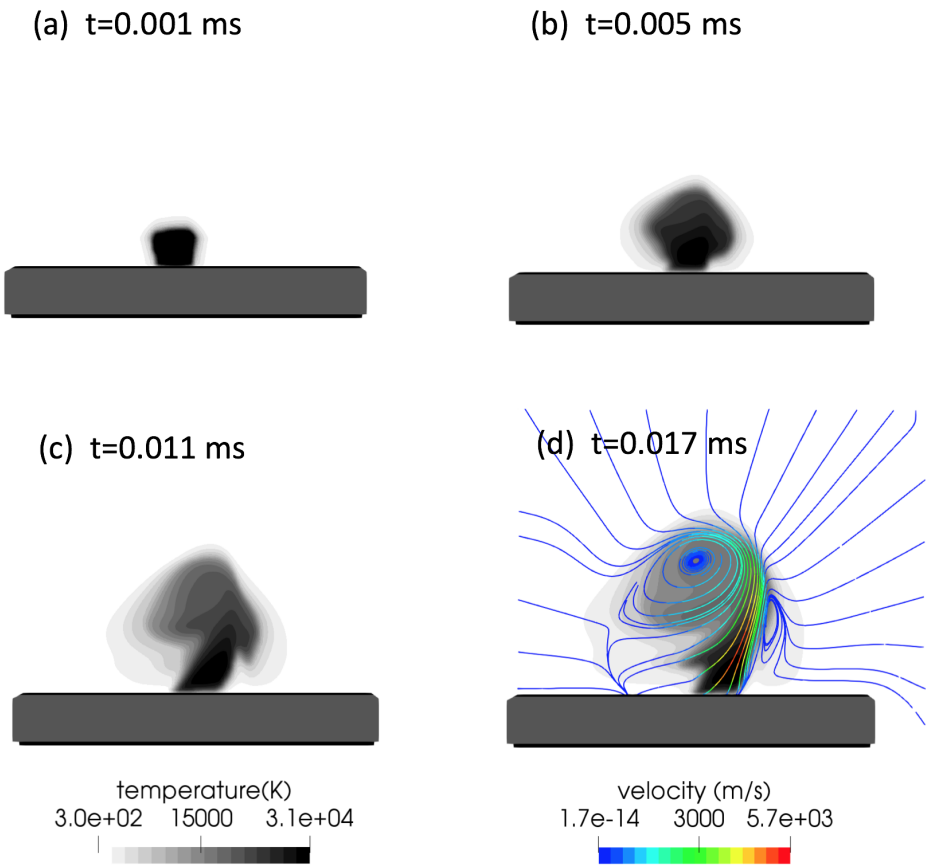

Figure 6.12: Temperature distribution at the center plane of the simulation. Streamlines are shown for t=0.017 ms. The electrode locations are shown in gray.

qualitatively similar the temperature distribution results are to observations of real arcs shown in Figure 5.7. Figure 6.12 shows that a jet tilted in the direction of propagation is forming due to Lorentz forcing near the interface of the arc and the dielectric. This jet creates a vertical structure, very similar to those seen in experiments. The vorticity generated by the jet is particularly obvious in the streamlines shown in Figure 6.12d. Note also that the velocity far from the arc is universally directed away from the arc due to the passage of the strong shock generated by the arc's ignition. The fact that the effect of the shock far exceeds the directed momentum addition of the arc is believed to be due to the coarseness of the simulation.

Chapter 7

Conclusion

This dissertation examines the plasma arc of the RailPAc magnetohydrodynamic flow actuator. The work seeks to better understand the nature of arc propagation, towards the design of a predictable and well-behaved high intensity gliding arc. Several experiment-based studies were performed examining the RailPAc plasma arc, focusing on electrical characterization, spectroscopic temperature analysis, narrow-band-imaging species evolution within the arc, and the effects of electrode surface oxidation states on the propagation of the arc. Additional experimental studies examined the effects of external magnetic fields and rod configurations, the effect of the wall near the electrodes, long-term damage on copper and Elkonite electrodes, as well as techniques for construction of RailPAc arrays which would be necessary in any large-scale implementation of the RailPAc. Computational studies examined phenomena which were difficult or impossible to characterize experimentally. This includes mechanisms of wall stabilization, root mobility over oxidized surfaces, and simulations of the arc column in two and three dimensions to examine coupling of the arc to surrounding gas.

The key contributions of this work can be split into two parts, both

of which have experimental and computational components. The first is the characterization of the RailPAc arc dynamics (electrically, chemically, and physically) and its coupling to the surrounding flow. This is examined experimentally with spectroscopy, high-speed narrow-band imaging, and electrical measurements, as well as computationally with commercial arc modeling software solving fluid flow coupled to the Maxwell's equations in potential form. The second is the examination of the RailPAc arc root interaction with the electrode surface, particularly the anode root, which has seen very little examination compared to the cathode in previous research efforts directed at high intensity gliding arcs. Both of these are combined in a computational effort to model the RailPAc arc in three dimensions.

7.1 Summary of Findings

The propagating arc of the RailPAc device was characterized with high-speed imaging, electrical measurements, and spectroscopy measurements. Three distinct stages of transit were observed. The initiation stage shows the formation and acceleration of a compact and coherent arc column. The arc column breaks into distinct bright anode and cathode columns connected by a less luminescent gas as the arc enters the main transit stage. The anode roots jump along the electrode during this stage, while the cathode roots move smoothly. These modes of transit result in a variety of repeatable fluctuations in current and breech voltage. In the quenching stage, the arc dissipates as the breech voltage drops below the minimum sustainable voltage for the rail

geometry.

The expansion of the arc column above the surface is a result of the combined effects of thermal expansion and induced magnetic fields on the columns. The differences in the characteristics of the anode root motion in comparison to those of the cathode root were proven to result in more severe damage of the anode electrode.

The RailPAc arc was found to have a temperature of ∼10,000 K and variations in the relative concentrations of copper and oxygen species were detected. The high temperature of the arc and increasing content of copper species in the arc corroborate the ablation effects visible on the rail.

Experiments manipulating the geometry of the RailPAc to alter local magnetic fields found that the arc velocity could be significantly increased by running additional turns of wire below the surface of the RailPAc to enhance the primary induced magnetic field. Muzzle directed fields generated with subsurface solenoidal electromagnets were shown to be able to raise the RailPAc arc away from the surface but not pull it down closer to the surface. Permanent magnets were able to duplicate these effects to a lesser degree.

Electrode spacing was found to have a dramatic effect on the RailPAc arc with smaller interelectrode spacing inducing the arc to move both faster and smoother. Rail spacing was analytically shown to be the sole factor in calculating the forcing on an arc with a length significantly smaller than the length of its electrodes.

Composition and structure of the RailPAc gliding arc were examined at several different electrode spacings using photometric high speed imaging. The arc was shown to consist of three separate regions: the column, the anode root, and the cathode root. The roots were shown to be dominated by plasma jets directed normally to the electrode surfaces. These jets deflect outward when far away from one another, but merge into a single jet when the electrodes are close together. The column was found to remain close to the surface with closer spaced electrodes and this seems to help keep the arc moving smoothly and quickly, while wider spaced electrodes encouraged the column to rise above the surface which resulted in chaotic arc transits.

Copper evaporated from the electrode surfaces displaces air products at the arc roots. This effect was demonstrated to be strongest when the roots anchor on the anode in the flush mounted case, and weakest in the free-floating rods where most copper in the arc comes from the cathode. Copper is more strongly present in the column when electrodes are closely spaced and the column is small. However, copper is removed after some time in the larger, more diffuse columns of the wider electrode spacing cases.

The RailPAc arc was simulated using a thermal plasma model which reproduced multiple phenomena observed in experiments on the RailPAc arc. Mechanisms for jet formation and wall stabilization of the arc were proposed based on results from the simulations and their similarity to experimentally observed phenomena. Conventional magnetic pumping jet formation mechanisms were found to be unnecessary to explain the formation of root jets in

the RailPAc electrode geometry. Instead, direct Lorentz forcing is proposed to be the primary driver for root jet formation in the RailPAc. Wall stabilization mechanisms due to pressure gradients, strong Joule heating, and electromagnetic pinching were identified and shown to become more prominent when electrode spacing is small compared to arc diameter and electrode width.

Oxidized anodes showed significantly better damage mitigation than their reduced counterparts. The lack of mechanical damage in the rails for the highly oxidized 2 mm rail spacing is very favorable for a flow actuator, which must be mounted on an aerodynamic surface and will likely be highly sensitive to surface deformations. Consistency of the RailPAc arc and the flow it induces can be increased by oxidation of the anode while simultaneously increasing efficiency, as shown by the lower arc power with oxidized anodes.

A free burning arc was simulated in two and three dimensions and a flush mounted electrode arc was simulated in three dimensions. The two-dimensional simulations reproduced behaviors shown in experiments and propagated with velocities of the same order as experiments. Arc velocity was shown to depend more strongly on applied field than device current as a consequence of higher currents generating larger arcs. Coupling of the flow was found to be mediated by pressure gradients generated across the arc and jet velocities were found to be a function of the magnitude of the forcing and not the length of arc propagation since the flow in the area around the arc quickly reached a steady state.

Three dimensional simulations produced qualitatively reasonable pre-

dictions for arc behavior however predictions of internal flow velocities were unreasonably large. Unphysical results are believed to be a result of overly coarse meshes necessary for reasonable computation times. Qualitative similarities with experiments including root jets, and arc residence times were identified in the simulations.

7.2 Arc Impermeability

Traditionally arcs have been considered to be impermeable to surrounding fluids, however one of the primary contributions of this dissertation has been to show that there is more nuance to this argument than previously understood. In Chapter 4 we showed that streamlines for the most part do not enter or exit the hot gas making up the arc as in Figure 4.14d. However it was also shown that streamlines may enter the arc provided there is sufficiently high local Joule heating to process gas as it enters the arc. These sites tend to be located at sharp kinks in the arc near the root attachment sites. Joule heating over a sufficiently large area can also allow fluid to enter the arc.

In Chapter 5 the arc root similarly processed new material into the arc only at sites of high Joule heating. These sites were at the leading and trailing edges of the arc attachment site at the electrode surface. The presence of these sites allowed the arc to grow outward.

Lastly in Chapter 6 the arc column was shown to be almost perfectly impermeable on its leading edge but the trailing edge which acts similarly to a separated region behind a bluff body allowed cold gas to remain in contact

with the hot arc for a prolonged period, thus bringing the gas there up to an electrically conductive temperature so that it might enter the arc.

Thus what we've shown is that the arc is mostly impermeable, but there are limited cases where localized regions of the arc will allow fluid to pass into them. Usually for this flow through to be significant, there must be a region of very high Joule heating near the edge of the arc which is usually only found at the arc roots.

7.3 Ideal Actuator

This dissertation has shown that there are several major parameters of the RailPAc which can be modified to significantly change the behavior of the RailPAc arc. These parameters are: electrode material, electrode shape, wire configuration, interelectrode spacing, and electrical inputs.

The work in this dissertation suggests the cathode should be constructed from Elkonite or another tungsten-copper alloy. The anode should be constructed of either pre-oxidized copper to minimize arc anchoring, or Elkonite to maximize electrode lifetime.

Flush mounted electrodes should be wide in the dimension transverse to travel to maximize the electromagnetic pinching effect discussed in Chapter 4. The electrodes should also be shallow to minimize forcing of the arc up and away from the RailPAc surface. The effect of the length of the electrodes was not studied here and would be an interesting parameter for further study.

Wire configuration around the actuator was shown to be an effective method for introducing an enhanced or altered external magnetic field. By winding the input wire several times underneath the surface of the actuator, higher velocities were achieved at a similar input energy. Unless structurally prohibitive, this would almost certainly be implemented into any practical actuator. Computational efforts also suggest that the arc velocity increases dramatically by increasing the applied magnetic field.

Bringing electrodes closer together was shown to be the most effective way of both increasing arc transit speed and regularizing the dynamic behavior of the arc. However, the total force delivered also drops for a shorter arc. The largest electrode spacing which still maintains smooth arc travel would thus be desirable. This was shown to be around 5 mm in Chapter 3. It was shown in Chapter 4 that closer spacing corresponds to higher velocity root jets. More powerful root jets should also correspond to greater stream-wise vorticity generation if mounted on an airfoil, which might aid in flow control. Further experiments in high velocity wind tunnels would need to be carried out to ascertain the relative importance of each of these effects.

Electrical inputs are the final means of altering the behavior of the RailPAc arc. Modeling suggests that the arc reaches a steady state quickly and that running the actuator beyond this point entrains air further away but does not increase the final velocity of the RailPAc wall jet. It may be desirable to deliberately shorten the arcing time of the RailPAc to minimize extraneous forcing and associated energy losses. Integrated currents above 1 kA also did

not significantly increase the velocity of the arc, so the desired device current would be below this value. Greater momentum addition can be achieved by increasing the magnetic field by one of the techniques discussed in Chapter 3 while keeping the device current low.

7.4 Future Work

Future work on the RailPAc should focus on three areas: manufacture and testing of optimized RailPAcs as discussed in the previous section, implementation of the RailPAc into real aerodynamic surfaces, and modeling of realistic RailPAc arcs.

As of now, the RailPAc has been implemented into airfoils in two studies. These were completed in a wind tunnel at flow velocities of $\sim$20 m/s and Reynolds numbers no higher than 4×10^5 [12, 82]. Both were performed on static airfoils, meaning dynamic stall behaviors could not be observed. Real world uses of the RailPAc would be at Reynolds numbers of at least 1×10^6 and ideally nonlinear fluid effects in dynamic stall would be leveraged by the actuator. Experimental efforts should thus be devoted to implementation of the RailPAc on rotary test stands and in larger high velocity wind tunnels.

Modeling efforts in the RailPAc have been reasonably accurate for two-dimensional simulations and less accurate for three-dimensional simulations owing to the computational costs and need for high resolution in three dimensions. Efforts should thus be primarily directed into improving the fidelity of three-dimensional modeling.

Chapter 8

Appendix

8.1 Mesh Convergence

A mesh convergence study was performed for the muzzle arc domain configuration. The domain used 4 mm spaced electrodes with geometry A from Figure 4.11. Relative L2 error norms between the finest mesh and successively coarse meshes are plotted in Figure 8.1. The solutions being compared are shown in Figures 8.2 and 8.3. The solutions are qualitatively similar for all cases particularly the temperature solution. The largest variation appears in the y-velocity shown in Figure 8.3. The smallest features resolved appear correctly in the cases with the cell size of 0.0001x0.0001 m^2 which was used in solutions discussed in Chapter 4. The error is still quite large showing that the solutions are not fully mesh converged, however this is not a major issue since these simulations are being used as a tool for insight into the physics involved rather than a 1 to 1 comparison with physical reality.

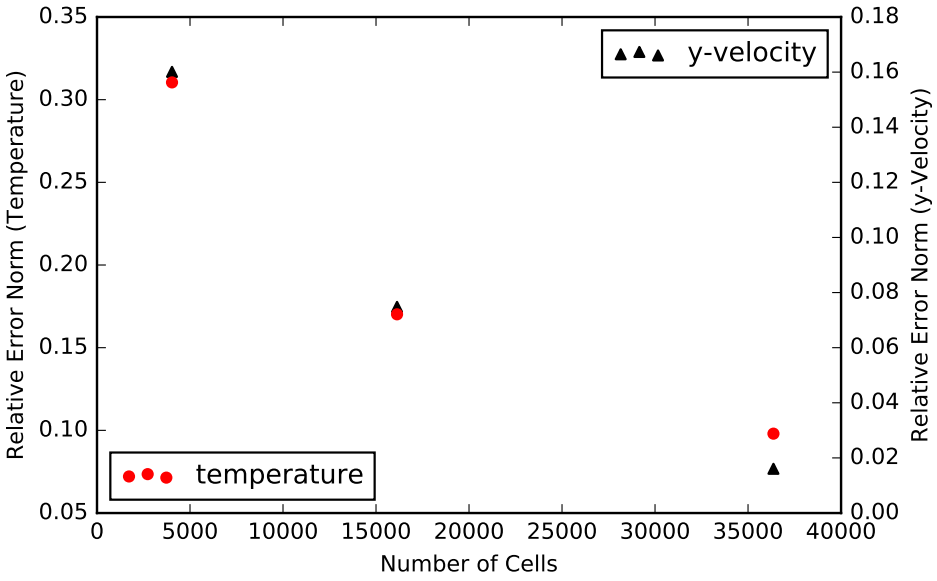

Figure 8.1: Relative L2 error for temperature and y-velocity after $10^{-}5$s simulation time for several mesh sizes.

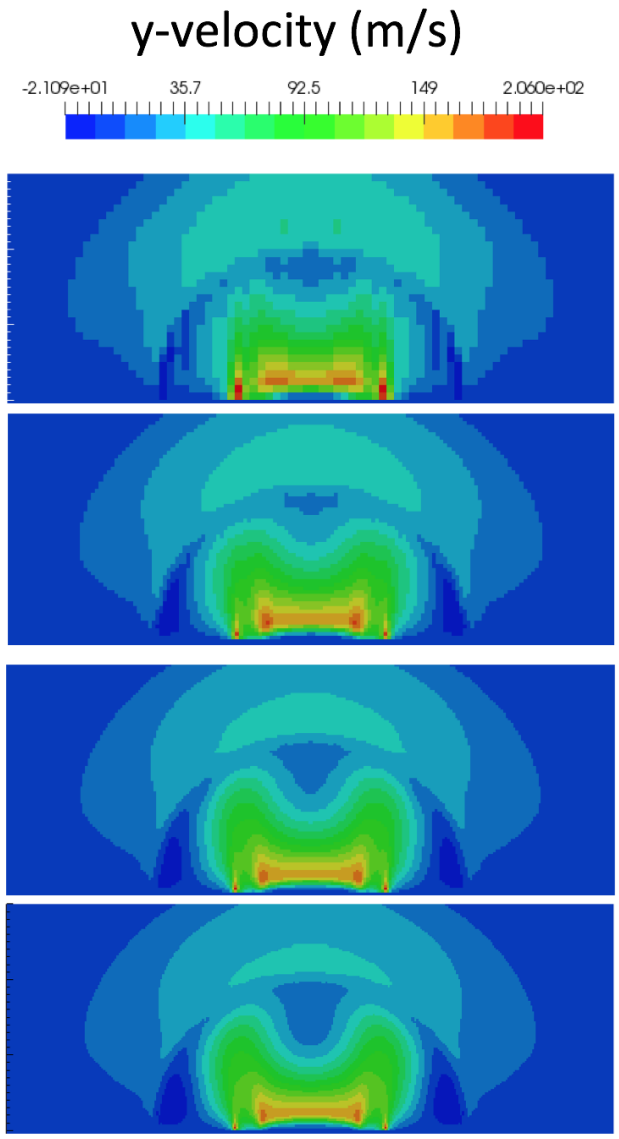

Figure 8.2: Temperature solutions for meshes with different cell sizes. From top to bottom, cell sizes are 0.0002 m, 0.0001 m, 0.000067 m, and 0.00005 m.

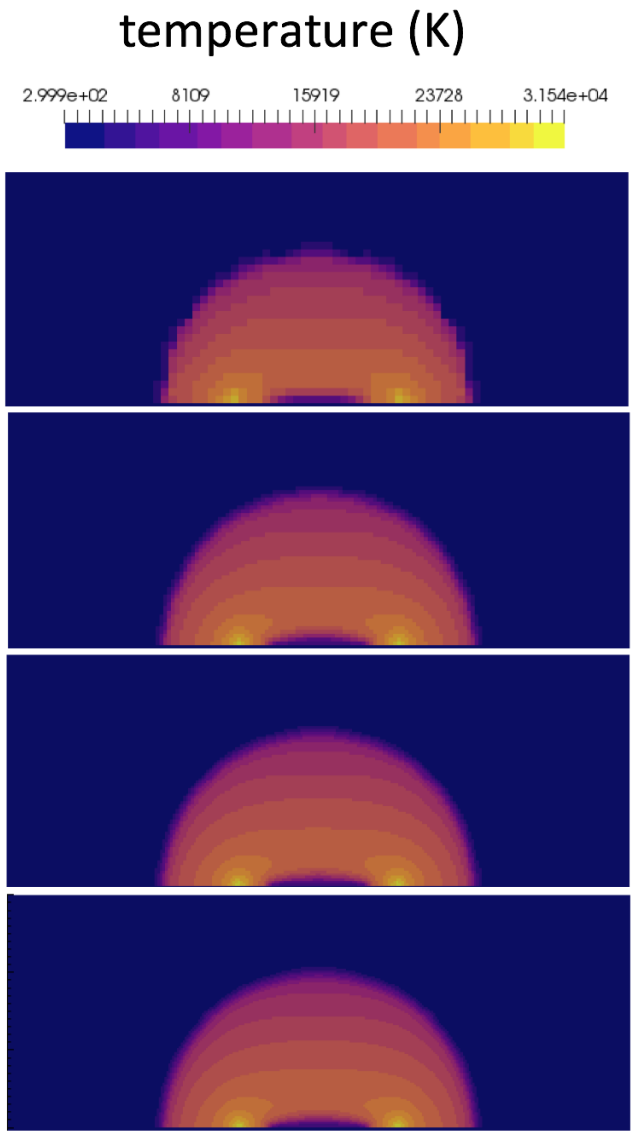

Figure 8.3: y-Velocity solutions for meshes with different cell sizes. From top to bottom, cell sizes are 0.0002 m, 0.0001 m, 0.000067 m, and 0.00005 m.

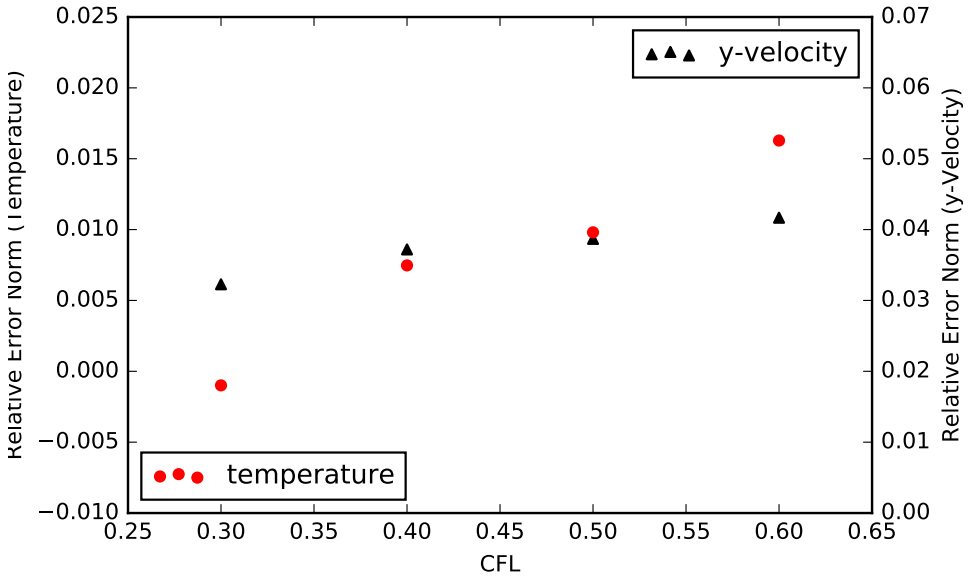

Figure 8.4: Relative L2 error for temperature and y-velocity after $10^{-}5$s simulation time with different CFL.

8.2 Rods - Larger Pictures

Larger versions of Figure 6.9 are shown below. Figure 6.9 a and b are shown in Figure 8.5, c and d in Figure 8.6, and e and f in Figure 8.7.

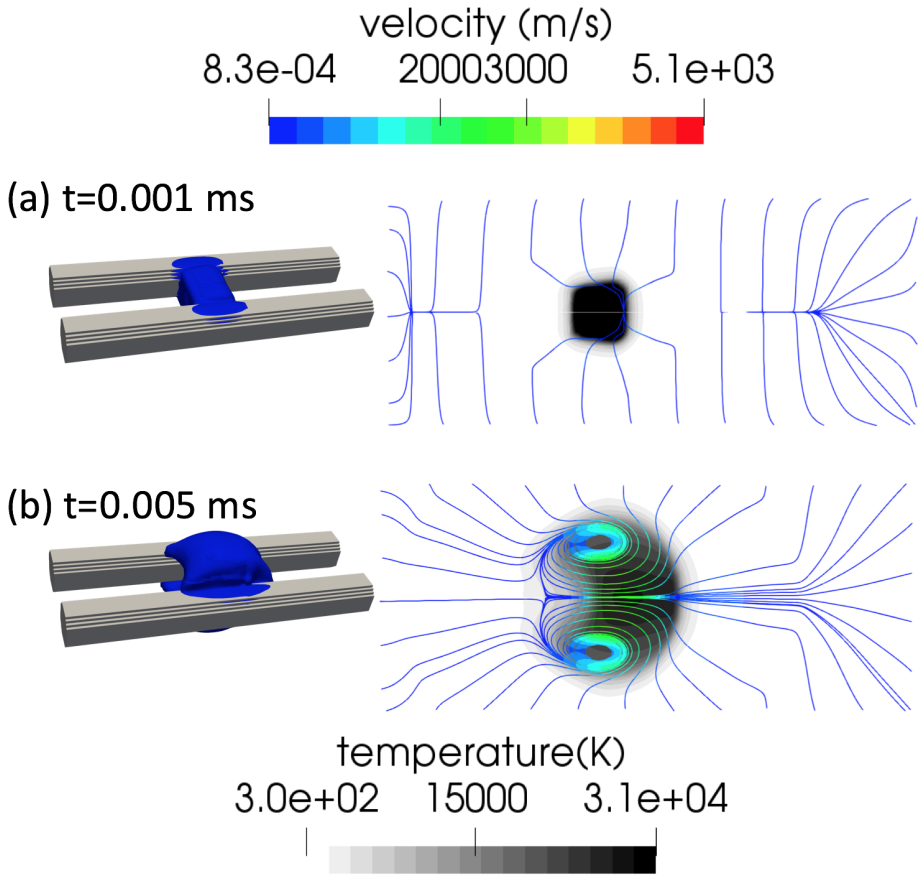

Figure 8.5: Time evolution of 5×10^7 A/m^2 current density contours, temperature distributions, and streamlines with rounded free-floating rails spaced 1.5 mm apart.

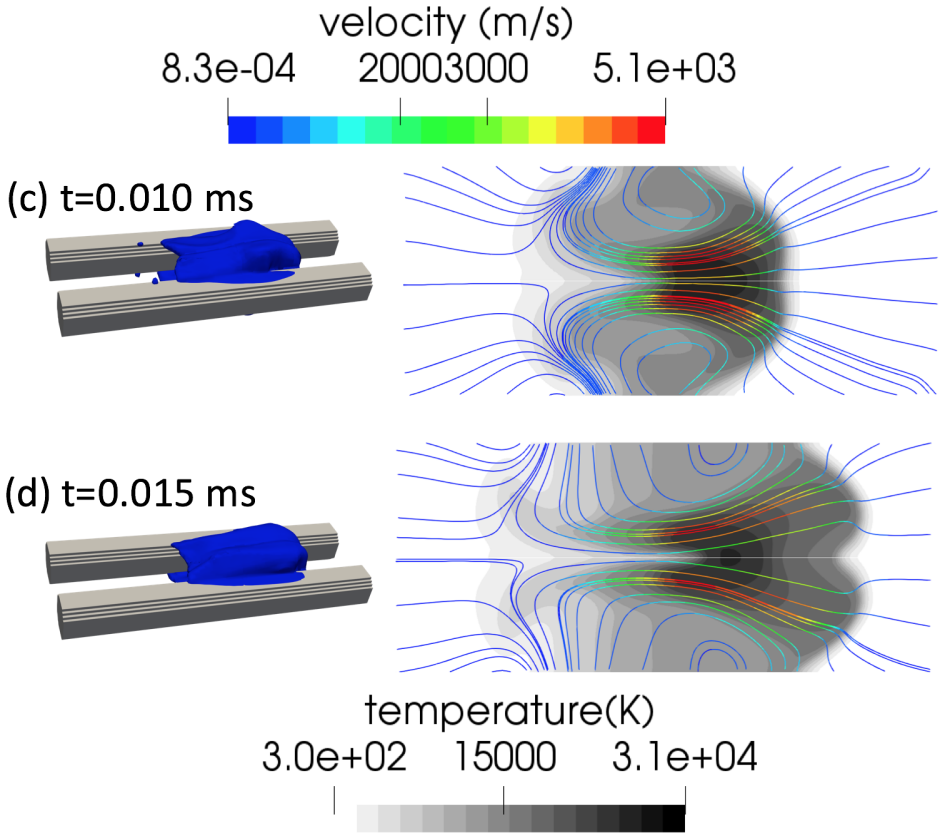

Figure 8.6: Time evolution of 5×10^7 A/m^2 current density contours, temperature distributions, and streamlines with rounded free-floating rails spaced 1.5 mm apart.

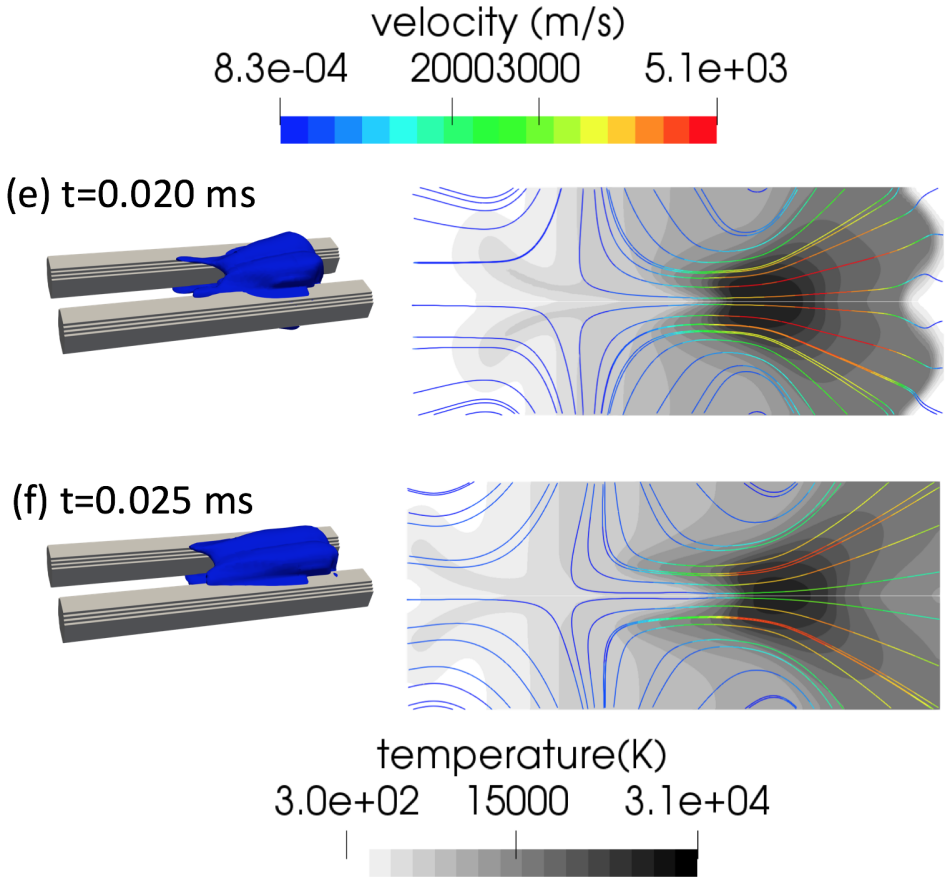

Figure 8.7: Time evolution of 5×10^7 A/m^2 current density contours, temperature distributions, and streamlines with rounded free-floating rails spaced 1.5 mm apart.

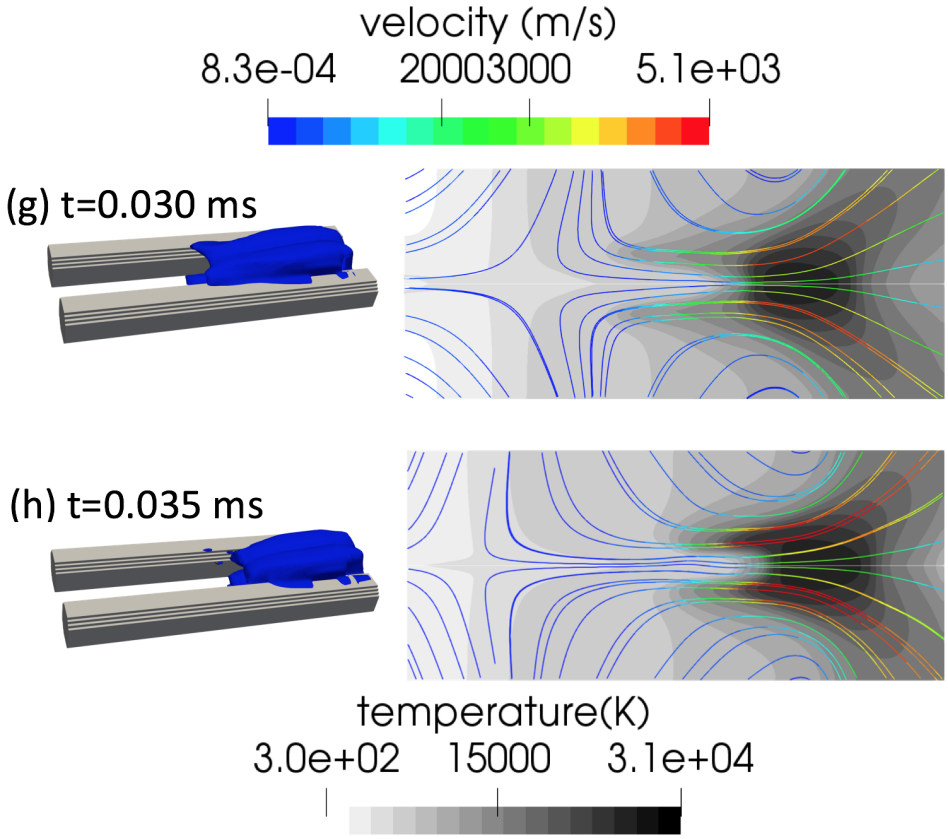

Figure 8.8: Time evolution of 5×10^7 A/m^2 current density contours, temperature distributions, and streamlines with rounded free-floating rails spaced 1.5 mm apart.

8.3 Larger Copies of Jet Characteristics

Larger versions of Figure 4.12 are shown below in Figures 8.9 and 8.10.

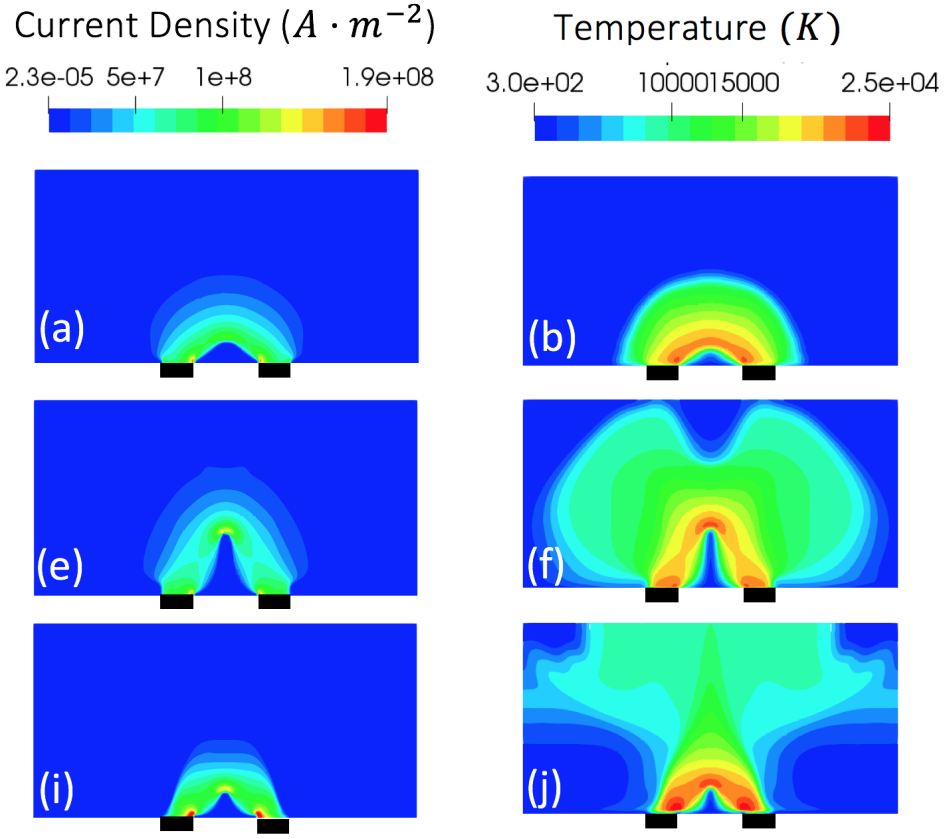

Figure 8.9: Evolution of current density and temperature for interelectrode spacing of 4 mm with Geometry B. Electrode locations are indicated by black bars. Temperature distributions are expected to correlate roughly with observed light intensity in experiments.

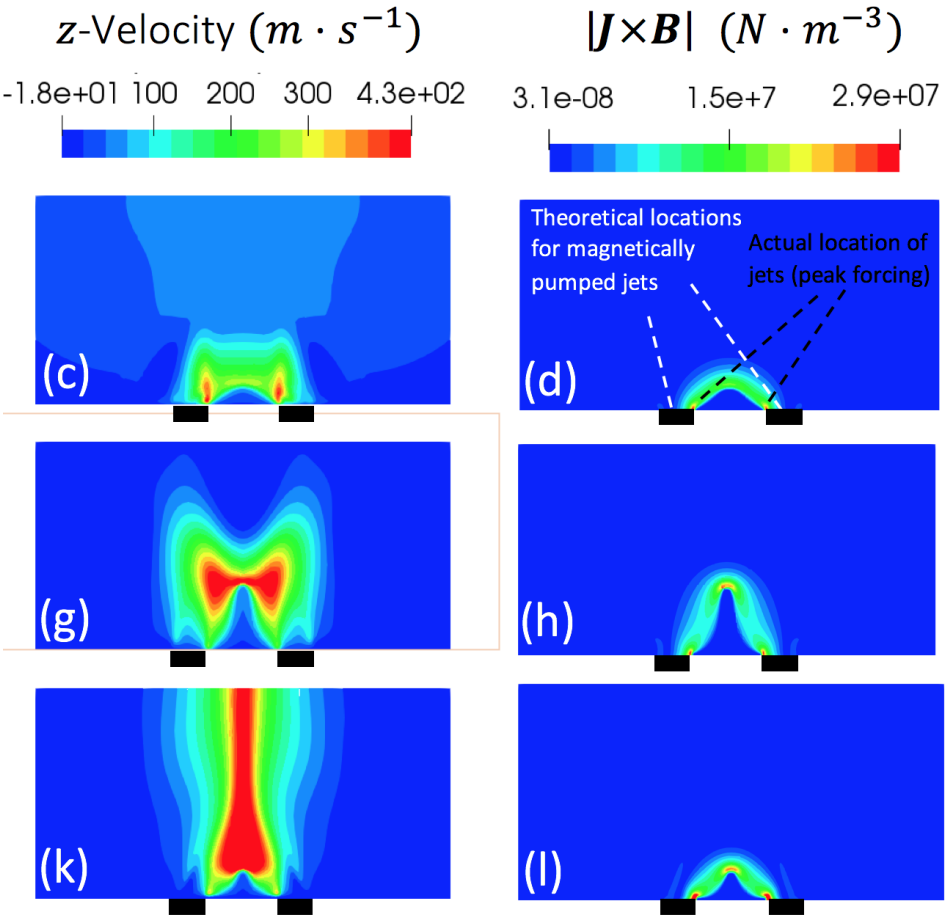

Figure 8.10: Evolution of vertical (y) velocity, and in plane Lorentz forcing for interelectrode spacing of 4 mm with Geometry B. Electrode locations are indicated by black bars.

Bibliography

[1] M. Gad el Hak, A. Pollard, and J.-P. Bonnet. *Flow Control: Fundamentals and Practices*. Springer Science and Business Media, 2003.

[2] L. N. Cattafesta and M. Sheplak. Actuators for active flow control. *Annual Review of Fluid Mechanics*, 43:247–272, 2011.

[3] T.C. Corke, C.L. Enloe, and S.P. Wilkinson. Dielectric barrier discharge plasma actuators for flow control. *Annual Review of Fluid Mechanics*, 42:505–529, 2010.

[4] M.L. Post and T.C. Corke. Separation control on high angle of attack airfoil using plasma actuators. *AIAA Journal*, 42:2177–2184, 2004.

[5] S.B. Leonov, C.D. Carter, B.E. Hedlund, A.W. Houpt, T. Ombrello, and A.A. Firsov. Control of amplitude and position of reflected shock wave by stripwise plasma. 2018.

[6] R. Kandala and G.V. Candler. Numerical studies of laser-induced energy deposition for supersonic flow control. *AIAA Journal*, 42:2266–2275, 2011.

[7] J. Little, K. Takashima, M. Nishihara, I. Adamovich, and M. Samimy. Separation control with nanosecond-pulse-driven dielectric barrier discharge plasma actuators. *AIAA Journal*, 50:350–365, 2012.

[8] Y.G. Utkin, S. Keshav, J.-H. Kim, J. Kastner, I.V. Adamovich, and Mo Samimy. Development and use of localized arc filament plasma actuators for high-speed flow control. *Journal of Physics D: Applied Physics*, 40:685, 2007.

[9] D. Roupassov, A. Nikipelov, M. Nudnova, and A. Starikovskii. Flow separation control by plasma actuator with nanosecond pulsed-periodic discharge. *AIAA Journal*, 47:168–185, 2009.

[10] C. Rethmel, J. Little, K. Takashima, A. Sinha, I. Adamovich, and M. Samimy. Flow separation control using nanosecond pulse driven dbd plasma actuators. *International Journal of Flow Control*, 3:213–232, 2011.

[11] A. V. Likhanskii, M. N. Shneider, D. F. Opaits, R. B. Miles, and S. O. Macheret. Limitations of the dbd effects on the external flow. Orlando, Florida, 2010.

[12] B. Pafford, J. Sirohi, and L. L. Raja. Propagating-arc magnetohydrodynamic plasma actuator for directional high-authority flow control in atmospheric air. *Journal of Physics D: Applied Physics*, 46,:pp, 2013.

[13] A. V. Likhanskii, M. N. Shneider, S. O. Macheret, and R. B. Miles. Modeling of dielectric barrier discharge plasma actuators driven by repetitive nanosecond pulses. *Physics of Plasmas*, 14:073501, 2007.

[14] J. P. Boeuf, Y. Lagmich, T. Unfer, T. Callegari, and L. C. Pitchford.

Electrohydrodynamic force in dielectric barrier discharge plasma actuators. *Journal of Physics D: Applied Physics*, 40:652–662, 2007.

[15] H. Sitaraman and L. L. Raja. Magneto-hydrodynamics simulation study of high speed flow control using rail plasma actuator (railpac). San Diego, California, 2013.

[16] D. M. Chen and E. Pfender. Modeling of the anode contraction region of high intensity arcs. *IEEE Transaction on Plasma Science*, 8(3):252–259, 1980.

[17] V. Kowalenko and G. A. Clark. Temperature estimates for a railgun plasma armature. *J. Phys. D: Appl. Phys*, 33:230–241, 2000.

[18] J. Zhu, J. Gao, A. Ehn, M. Aldn, Z. Li, D. Moseev, Y. Kusano, M. Salewski, A. Alpers, P. Gritzmann, and M. Schwenk. Measurements of 3d slip velocities and plasma column lengths of a gliding arc discharge. 106:044101, 2015.

[19] R. Ma, M. Rong, F. Yang, Y. Wu, H. Sun, D. Yuan, H. Wang, and C. Niu. Investigation on arc behavior during arc motion in air DC circuit breaker. *IEEE Transactions on Plasma Science,*, 41(9):2551–2560, 2013.

[20] S. S. Glickstein. Temperature measurements in a free burning arc. pages 222–229, 1976.

[21] S. M. Shkolnik. Anode phenomena in arc discharges: a review. *Plasma Sources Sci. Technol., vol. 20, no*, 20(1):013001, 2011.

[22] N. Sanders, K. Etemadi, K. C. Hsu, and E. Pfender. Studies of the anode region of a high- intensity argon arc. *Journal of Applied Physics*, 53(6):4136–4145, 1982.

[23] W. Petrie and E. Pfender. The influence of the cathode tip on temperature and velocity fields in a gas-tungsten arc. *Weld. J. Res. Suppl.*, 49:588, 1970.

[24] A. E. Guile. Arc-electrode phenomena. *Proceedings of the Institution of Electrical Engineers*, 118(9R):1131–1154, 1971.

[25] L. H. Germer. Physical processes in contact erosion. *Journal of Applied Physics*, 29(7):1067, 1958.

[26] Z. Chen and K. Sawa. Particle sputtering and deposition mechanism for material transfer in breaking arcs. *Journal of Applied Physics*, 76(6):3326–3331, 1994.

[27] A. Guile. Model of emitting sites and erosion on nonrefractory arc cathodes with relatively thick oxide films. *Proceedings of the Institution of Electrical Engineers*, 121(12):1594–1598, 1974.

[28] H. C. Miller. Anode modes in vacuum arcs. *IEEE Transactions on Dielectrics and Electrical Insulation*, 4(3):382388, 1997.

[29] A. Guile. Stored charges in relatively thin oxide films. *J Phys D: Appl Phys.*, 5(6):1153, 1972.

[30] J. McBride and P. Jeffery. Anode and cathode arc root movement during contact opening at high current. *IEEE Transaction on Components and Packaging Technology*, 22(1):38–46, 1999.

[31] A. Guile and B. Juttner. Basic erosion processes of oxidized and clean metal cathodes by electric arcs. *IEEE Transactions on Plasma Science*, 8(3):259–269, 1980.

[32] J. G. J. Sloot and G. Bosch. Some conditions for arc movement under the influence of a transverse magnetic field. *Holectechniek*, 2(3):98–106, 1972.

[33] C. Lichun and X. Jiazhi. Motion of magnetically driven arcs on oxidized electrodes. *IEEE Transactions on Components, Hybrids, and Manufacturing Technology*, 5(1):86–89, 1982.

[34] M. S. I. Rageh, D. V. Morgan, and A. E. Guile. Arc cathode root initiation on aluminium oxide films. *Journal of Physics D: Applied Physics*, 10(16):2277–2284, 1977.

[35] M. Rageh, D. Morgan, and A. Guile. Charge storage and arc cathode root initiation on aluminium oxide films. *J. Phys. D: Appl. Phys.*, 8(4):434–437, 1975.

[36] K. Poeffel. Influence of the copper electrode surface on initial arc movement. *IEEE Transactions on Plasma Science*, 8(4):443–448, 1980.

[37] G. Yang and J. Heberlein. Anode attachment modes and their formation in a high intensity argon arc. *Plasma Sources Sci. Technol.*, 16(23):529–542, 2007.

[38] M. D. Gray, Y. J. Choi, J. Sirohi, L. L., and Raja. Structure of propagating arc in a magnetohydrodynamic rail plasma actuator. *J. Phys. D: Appl. Phys.*, 49(1):015202, 2015.

[39] J. J. Lowke. Simple theory of free-burning arcs. *Journal of Physics D: Applied Physics*, 12:1873, 1979.

[40] S. Ramakrishnan. An approximate model for high-current freeburning arcs. *Journal of Physics D: Applied Physics*, 11:2267, 1978.

[41] T. Myers, C. N. McKinnon, and J. Lysen. Experimental investigation of a magnetically balanced arc in a transverse argon flow. *J. Eng. Power, vol. 88, no*, 88(1):27–30, 1966.

[42] J. Uhlenbusch. Miscellaneous arc devices. *Physica B+C*, 82(1):61–85, 1976.

[43] W. C. Roman and T. W. Myer. Experimental investigation of an electric arc in transverse aerodynamic and magnetic fields. *AIAA*, 5(11):2011–2017, 1967.

[44] L. Nicolai and A. Kuethe. Properties of magnetically balanced arcs. *The Physics of Fluids*, 12(10):2072–2082, 1969.

[45] H. Rachard, P. Chevrier, D. Henry, and D. Jeandel. Numerical study of coupled electromagnetic and aerothermodynamic phenomena in a circuit breaker electric arc. *International Journal of Heat and Mass Transfer*, 42:1723–1734, 1999.

[46] P. K. Ray. Arc restrike in the rail accelerator. 1989.

[47] K. Koyama, H. Toya, Y. Wada, and A. Hasegawa. Arc behavior driven by electromagnetic force between rail electrodes. page 8437, 1993.

[48] G. Velleaud, A. Laurent, and M. Mercier. A study of the kinematics of a low-voltage breaking self-blown arc: Analysis of the derivative of the anode-cathode voltage. *J Phys D: Appl. Phys.*, 22:933–940, 1989.

[49] F. Yang, Y. Wu, M. Rong, H. Sun, and A. B. Murphy. Low-voltage circuit breaker arcssimulation and measurements. *J. Phys. D: Appl. Phys*, 46:273001, 2013.

[50] P. R. Zeller and W. F. Rieder. Arc structure, arc motion, and gas pressure between laterally enclosed arc runners. *IEEE Trans. Compon. Packag. Technol*, 24:337–41, 2001.

[51] M. Mercier, D. Cajal, A. Laurent, G. Velleaud, and F. Gary. Evolution of a low-voltage electric arc. *J. Phys. D: Appl. Phys*, 29:95–98, 1996.

[52] P. Teste, T. Leblanc, and J. P. Chabrerie. Study of the arc root displacement and three-dimensional modelling of the thermal phenomena

occuring in a hollow cathode submitted to an electric moving arc. *J. Phys. D: Appl. Phys*, 28:888–898, 1995.

[53] M. Lindmayer. The influence of contact materials and chamber wall materials on the migration and the splitting of the arc in extinction chambers. *IEEE Transactions on Parts, Hybrids, and Packaging*, PHP-9(1), 1973.

[54] M. Lindmayer and J. Paulke. Arc motion and pressure formation in low voltage switchgear. *IEEE Trans. Compon. Packag. Manuf. Technol. A*, 21:33–9, 1998.

[55] W. Yi and M. Rong. Numerical analysis of the effect of the chamber width and outlet area on the motion of an air arc plasma. *IEEE Trans. Plasma Sci*, 36:28317, 2008.

[56] P. M. Weaver and J. W. McBride. Magnetic and gas-dynamic effects on arc motion in miniature circuit-breakers. *IEEE Trans. Compon. Packag. Manuf. Technol. A*, 17:39–46, 1994.

[57] D. A. Wetz, F. Stefani, J. Parker, and I. R. McNab. Advancements in the development of a plasma-driven electromagnetic launcher. 2008.

[58] A. Kramida, Y. Ralchenko, J. Reader, and N. A. T. Nist atomic spectra database (ver 5.2). 2014.

[59] J. J. Camacho. Optical emission studies of nitrogen plasma generated by IR CO2 laser pulses. *J. Phys. B: At. Mol. Opt. Phys*, 40:45734590, 2007.

[60] J. A. Aguillera and C. Aragon. Characterization of a laser-induced plasma by spatially resolved spectroscopy of neutral atom and ion emissions. *Spectrochimica Acta Part B*, 40:1861–1876, 2004.

[61] Y. J. Choi, J. Sirohi, L. L., and Raja. Measurement of transient force produced by a propagating arc magnetohydrodynamic plasma actuator in quiescent atmospheric air. *J. Phys. D: Appl. Phys.*, 48(42):425204, 2015.

[62] J. V. Parker. Why plasma armature railguns dont work (and what can be done about it. 1989.

[63] R. Haug, R. Hahn, Z. J. He, M. Samba, and P. C. Gouloubi. Current transfer between two parallel electrical arcs. *J. Phys. D: Appl. Phys*, 24:325–330, 1991.

[64] M. Schnick, U. Fussel, M. Hertel, A. Spille-Kohoff, and A. B. Murphy. Metal vapour causes a central minimum in arc temperature in gasmetal arc welding through increased radiative emission. *J. Phys. D: Appl. Phys*, 43:022001, 2010.

[65] A. Pathak. An elementary argument for the magnetic field outside a solenoid. *European Journal of Physics*, 38(1):015201, January 2017.

[66] Y. J. Choi, M. Gray, J. Sirohi, and L. Raja. Effects of anchoring and arc structure on the control authority of a rail plasma actuator. *J. Phys. D: Appl. Phys.*, 50(35):355203, 2017.

[67] *VizSpark: A Multi-Dimensional Simulator for Thermal Plasma Systems, User Manual (Version 2.1).* Esgee Technologies, Inc., 2015.

[68] S. Gu, J. He, R. Zeng, B. Zhang, G. Xu, and W. Chen. Motion characteristics of long ac arcs in atmospheric air. *Applied Physics Letters*, 90:051501, 2007.

[69] E. Pfender, J. Fincke, and R. Spores. Entrainment of cold gas into thermal plasma jets. *Plasma Chemistry and Plasma Processing*, 11(4):529–543, Dec 1991.

[70] P. C. Huang, K. Heberlein, and E. Pfender. A two-fluid model of turbulence for a thermal plasma jet. *Plasma Chemistry and Plasma Processing*, 15(1):25–46, Mar 1995.

[71] F. Yang, M. Rong, Y. Wu, A. B. Murphy, J. Pei, L. Wang, Z. Liu, and Y. Liu. Numerical analysis of the influence of splitter-plate erosion on an air arc in the quenching chamber of a low-voltage circuit breaker. *J. Phys. D: Appl. Phys.*, 43(43):434011, 2010.

[72] L.Piqueras, D. Henry, D. Jeandel, J. Scott, and J. Wild. Three-dimensional modelling of electric-arc development in a low-voltage circuit-breaker. *International Journal of Heat and Mass Transfer*, 51:4973–4984, 2008.

[73] D.D. Ryutov. Phenomenological theory of the kink instability in a slender plasma column. *Physics of Plasmas*, 13:032105, 2006.

[74] S.-K. Leea, H.-C. Hsua, and W.-H. Tuana. Oxidation behavior of copper at a temperature below 300 c and the methodology for passivation. *Materials Research*, 19(1):51–56, 2016.

[75] L. C. Cheng and P. Zhao. Influence of electrode surface state and electrode thermal parameters on the motion of magnetically driven arcs. *IEEE Transactions on Components, Hybrids, and Manufacturing Technology*, 10(4):662–665, 1987.

[76] A. B. Murphy, M. Tanaka, K. Yamamoto, S. Tashiro, T. Sato, and J. J. Lowke. Modelling of thermal plasmas for arc welding: the role of the shielding gas properties and of metal vapour. *Journal of Physics D: Applied Physics*, 42:194006, 2009.

[77] N.A. Sanders and E. Pfender. Measurement of anode falls and anode heat transfer in atmospheric pressure high intensity arcs. *Journal of Applied Physics*, 55:714–722, 1984.

[78] H.A. Dinulescu and E. Pfender. Analysis of the anode boundary layer of high intensity arcs. *Journal of Applied Physics*, 51:3149–3157, 1980.

[79] R.-T. Lee, H.-H. Chung, and Y.-C. Chiou. Arc erosion behaviour of silver electric contacts in a single arc discharge across a static gap. *IEEE Proceedings - Science, Measurement and Technology*, 148:8–14, 2001.

[80] L. D. L. S. Valladares, D. H. Salinas, A. B. Dominguez, D. A. Najarro, S. Khondaker, T. M. a. C. Barnes, J. A. Aguiar, and Y. Majima. Crys-

tallization and electrical resistivity of cu2o and cuo obtained by thermal oxidation of cu thin films on sio2/si substrates. *Thin Solid Films*, 520:6368–6374, 2012.

[81] A.E. Guile, V.W. Adams, W.T. Lord, and K.A. Naylor. High-current arcs in transverse magnetic fields in air at atmospheric pressure. *Proceedings of the Institution of Electrical Engineers*, 116:645–652, 1969.

[82] Y. J. Choi, J. Sirohi, M. Gray, and L. Raja. Static stall alleviation using a rail plasma actuator. *J. Phys. D: Appl. Phys.*, in press https://doi.org/10.1088/1361-6463/aac7b2, 2018.